Modelling of syngas fermentation with *C. autoethanogenum* in an external loop gaslift reactor

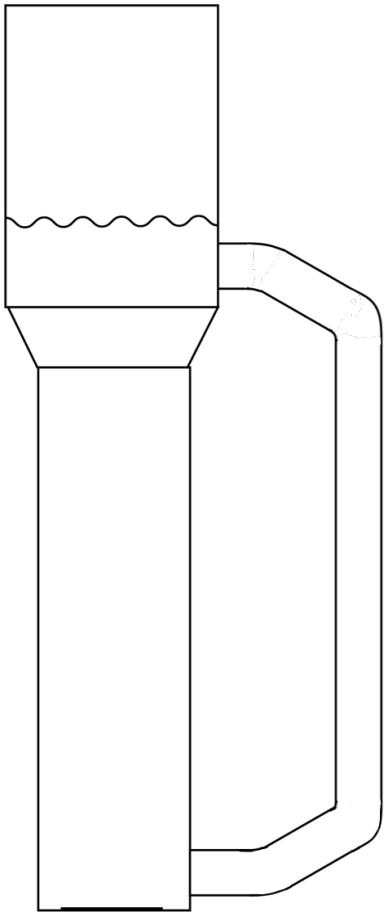

Laura Brocades Zaalberg

TU Delft

Modelling of syngas fermentation with *C. autoethanogenum* in an external loop gaslift reactor

By

Laura Brocades Zaalberg

In partial fulfilment of the requirements for the degree of

Master of Science

in Life Science and Technology with an emphasis in Biochemical Engineering

at the Delft University of Technology,
to be defended publicly on Monday May 31st, 2021 at 14:00 PM.

September 2020 - May 2021

Daily supervisor:	Lars Puiman
Thesis committee:	Cristian Picioreanu
	Marcel Ottens
	Henk Noorman

TU Delft

Abstract

The use of syngas, a renewable energy soucre, has raised increasing interest for the production of chemicals. Syngas, a mixture containing CO, H_2 and CO_2, can be converted into hydrocarbons, such as ethanol and 2.3-butanediol via a biochemical conversion. In this process the micro-organism *Clostridium autoethanogenum* (*C. autoethanogenum*) converts syngas into these hydrocarbons under ambient conditions. Still, syngas fermentation has drawbacks which influence the commercialization and scale-up, which are low mass transfer rates due to the low solubility of syngas and the low growth rate of *C.autoethanogenum*.

An external loop gaslift reactor (ELGLR) was considered to potentially overcome the low mass transfer rates. The recirculation of liquid in the reactor induces pneumatic agitation and the recirculation of biomass which can improve the mass transfer and growth of *C. autoethanogenum* and is currently used at industrial scale by the company LanzaTech. A 1D model of an external loop gaslift reactor can provide understanding of the hydrodynamics and syngas fermentation process with *C.autoethanogenum* in a ELGLR. A 1D model has the advantage to be less computationally intensive compared to other dimension models and can be solved dynamically which can be valuable to comprehend the phenomena of syngas fermentation over time in the reactor. The predictions obtained by this model can be used to roughly determine ranges for optimal syngas fermentation, which could be useful for higher dimensional models or experimental set-ups.

The model considered a continuous inflow and outflow as well as liquid recirculation between the riser and the downcomer. The hydrodynamics of the reactor were based on correlations and equations proposed in literature, whereas the syngas conversion by *C. autoethanogenum* was described by a black-box approach. The hydrodynamic parameters were validated with experimental data proposed in literature and a CFD model, which was also used for the comparison of the syngas fermentation parameters. Additionally, the syngas fermentation in the 1D model was further optimized by adjusting external variable parameters like the dilution rate, inlet biomass concentration and the gas mass inflow rate. The syngas fermentation parameters in terms of ethanol productivity and CO conversion yield were compared to the industrial syngas fermentation process which is operated by the company LanzaTech.

The 1D model was found to predict the hydrodynamics parameters in the same order of magnitude as the experimental data. Yet, the hydrodynamic parameters predicted with the CFD and 1D model corresponded less. Additionally, the syngas fermentation parameters, varied greatly between the 1D and CFD model, probably as a result of different hydrodynamic parameter estimations in both models.

Using an optimization procedure, a dilution rate of $3{\cdot}10^{-5}$ 1/s, gas inflow rate of 2.5 kg/s and a biomass inlet concentration of 10 g/L were found to be the most advantageous for syngas fermentation in the 1D ELGLR model, resulting in an ethanol productivity of 0.6 g/L/h and 24.9% conversion. The comparison with the estimated industrial performance deviated 75.5% and 4.3% in ethanol productivity and CO-to-ethanol conversion yield, respectively. Due to the rough estimations and calculations, the validity of the 1D model to predict the syngas fermentation in an industrial process could not be deduced.

In conclusion, the 1D model was considered to reasonably predict the hydrodynamics of an actual external loop gaslift reactor and give a rough approximation of the syngas fermentation by *C. autoethanogeum*. However, more experimental data on the syngas fermentation process is necessary for a complete understanding of the syngas fermentation process within a ELGLR.

Nomenclature

Symbol	Definition	Unit
a	interfacial area	1/m
A	surface area	m^2
C	concentration	mol/m^3
d_b	bubble diameter	m
D	diameter	m
D_{if}	gas diffusion coefficient	m^2/s
D_{il}	dilution rate	1/s
D_G	gas dispersion coefficient	m^2/s
D_L	liquid dispersion coefficient	m^2/s
ε_{G}	gas hold-up	
ε_{L}	liquid hold-up	
η_{L}	liquid viscosity	Pa s
F	volumetric flowrate	m^3/s
g	gravitational constant	m^2/s
H	Henry coefficient	$mol/(Pa\ m^3)$
I_{et}	ethanol inhibition term	
J	flux	$mol/m^2/s$
k_B	Boltzmann constant	J/K
K_B	friction loss coefficient	
K_I	inhibition constant	mol/m^3
k_L	liquid mass transfer coefficient	m/s
K_s	Monod constant	mol/m^3
L	length	m
μ	growth rate	1/s
M	molar mass	g/mol
m_{in}	mass inflow	kg/s
m_s	maintenance coefficient	mol/mol X/s
n	molar flowrate	mol/s
P	pressure	Pa
P_b	pressure bottom riser	Pa
P_L	atmospheric pressure	Pa
q	biomass specific rate	mol/mol X/s
q_{max}	maximum biomass specific rate	mol/mol X/s
ρ	density	kg/m^3
r	reaction rate	mol/s
R	volumetric reaction rate	$mol/m^3/s$
R_{tr}	mass transfer rate	$mol/m^3/s$
R	gas constant	J/mol/K
R_0	solute radius	m
T	temperature	°C or K
t	time	s
u	velocity	m_R/s
u	superficial velocity	$m^3/m_R^2/s$
V	Volume	m^3
v_b	terminal bubble rise velocity	m/s
y	molar gas fraction	
Y	stoichiometric coefficient	
Y	conversion yield	

Supercripts and Subscripts

Symbol	Definition
L	liquid phase
G	gas phase
ir	inflow riser
r	riser
d	downcomer
or	outflow riser
CO	carbon monoxide
EtOH	ethanol
X	biomass
N_2	nitrogen
0	initial value
cat	catabolisme
met	metabolisme
i	species
in	inlet

Contents

Chapter 1

Introduction

The demand and use of fossil fuels for energy, fuel and chemical production increases each year (Köpke and Simpson, 2020; Daniell et al., 2012). Yet, fossil fuels are finite resources that will become scarce in time and combustion of fossil fuels results in emission of greenhouse gasses (Daniell et al., 2012). An alternative for using finite resources is the use of renewable resources for the production of energy, fuels and chemicals (Köpke and Simpson, 2020). A renewable source that can be used as feedstock for these products while simultaneously reducing the emission of greenhouse gasses is a second generation feedstock. Nowadays the most abundant second generation feedstock worldwide is lignocellulosic biomass (Paul and Dutta, 2018). This feedstock is potential to be used at large scale for the production of bioethanol, in which the fermentable sugars obtained from the lignocellulosic biomass are used as substrate (Munasinghe and Khanal, 2010a). Yet, the presence of the unfermentable compound lignin in the lignocellulosic biomass reduces the yield of bio-ethanol on substrate and creates an additional waste stream (Liew et al., 2016). An alternative use of lignocellulosic biomass that has raised more worldwide interest over the past few years is gasification of the lignocellulosic biomass. Gasification enables the use of biomass as entirety and gasification of the lignocellulosic biomass results in formation of synthesis gas or syngas. Syngas can be converted into a wide variety of chemicals, such as ethanol, for instance in a sygnas fermentation process. (Liew et al., 2016; Munasinghe and Khanal, 2010a; Asimakopoulos et al., 2018) .

1.1 Synthesis gas and application

Synthesis gas is a gas that is mainly composed of carbon monoxide (CO), hydrogen (H_2) and carbon dioxide (CO_2). The gas can be obtained from a wide variety of resources which include, lignocellulosic biomass, municipal solid waste and steel mill off gasses (Köpke and Simpson, 2020; National EnergyTechnology Laboratory, 2014). The composition of syngas through gasification of these resources is highly dependent on the type of resource, gasifier and process conditions (Abubackar et al., 2011). The conversion of syngas into hydrocarbons occurs mainly via two different processes, the thermal chemical process: Fisher-Tropsch (FT) or a biocatalytic process (Yang et al., 2003; Abubackar et al., 2011). In the Fischer-Tropsch process, syngas is converted into hydrocarbons, such as ethanol, under elevated pressures (>30 bar) and high temperatures (150-350 °C) (Liew et al., 2016; Abubackar et al., 2011). The process includes two reactions steps, the water gas shift reaction (WGS) and the Fischer-Tropsch reaction (FT). The WGS reaction converts CO into H_2 (eqn. 1.1) to increase the CO/H_2 ratio for the FT reaction that is catalyzed by a chemical catalyst (eqn. 1.2) (Abubackar et al., 2011).

$$CO + H_2O \longrightarrow H_2 + CO_2 \text{ (WGS)} \tag{1.1}$$

$$2\,CO + 4\,H_2 \longrightarrow C_2H_5OH + H_2O \text{ (FT)} \tag{1.2}$$

The conversion in the Fischer-Tropsch process is faster due to the use of chemical catalysts, for example copper or cobalt. However, the use of chemical catalysts has several drawbacks which include the catalysts' sensitivity to impurities in syngas, a fixed substrate ratio $CO{:}H_2$ and low product specificity (Abubackar et al., 2011; Mohammadi et al., 2011; Köpke and Simpson, 2020). The purification and fixed gas ratio of the syngas mixture results in an increase of costs in the chemical conversion process (Köpke and Simpson,

2020). In the biocatalytic process, the conversion of syngas occurs under ambient temperature (37 °C) and pressure (1 bar) (Liew et al., 2016). The gasified biomass in the biocatalytic conversion process is converted into hydrocarbons, such as ethanol or other organic compounds, 2.3-butanediol and acetate (Abubackar et al., 2011; Daniell et al., 2012). The biocatalytic process has several advantages compared to the FT-process, which are the ambient process conditions, high specificity of the biocatalysts, which can lead to higher yields, enhanced tolerance for contaminants, such as tars and no fixed substrate ratio of CO:H_2 is required (Abubackar et al., 2011; Munasinghe and Khanal, 2010a).

1.2 Synthesis gas fermentation

In the biocatalytic process syngas is converted by micro-organisms. Anaerobic acetogenic bacteria or acetogens are micro-organisms that are able to convert syngas into higher valuable compounds such as, 2.3-butanediol (Köpke et al., 2011a). These bacteria have the advantage of using CO as sole carbon and energy source compared to other micro-organisms (Liou and Madsen, 2008; Valgepea et al., 2018). In acetogens, the carbon in syngas is fixated by the Wood−Ljungdahl pathway or Acetyl-CoA pathway. The Wood−Ljungdahl pathway has two branches, a carbonyl and methyl branch (eastern and western branch, respectively)(fig. 1.1). In the carbonyl branch the CO from syngas is converted to CO_2, by the enzyme CODH which catalyzes the biological water-gas shift reaction (WGS). The CO_2 is then further reduced to the methyl group that is present in the acetyl-CoA molecule. In the methyl branch CO_2 is either converted into CO by the WGS reaction by the CODH enzyme or CO is directly converted into the carbonyl group of the acetyl-CoA molecule. The carbonyl and methyl branch together yield the precursor acetyl-CoA (Liew et al., 2016; Abubackar et al., 2011). Acetogenic bacteria can further convert the acetyl-CoA during solventogenesis into solvents such as, ethanol and butanol. This occurs under growth limited conditions, for instance at low pH (Richter et al., 2016)(fig. 1.1). During acetogenesis acetyl-CoA is converted into acetate which occurs during growth of the micro-organism (Richter et al., 2016) (fig. 1.1). Hence, the product spectrum is dependent on the pH of the environment (Abubackar et al., 2011; Richter et al., 2016). The production of undissociated acetic acid in the cell environment during acetogenesis induces a metabolic switch from acetogenesis to solventogenesis, in which the acetic acid will be converted to ethanol (Richter et al., 2013). The products formed by acetogens can also be used as substrate for production of higher valuable compounds within the same fermentation, by performing a co-culture fermentation in which two micro-organisms are present. The product of one micro-organism can be used as substrate by the other micro-organism resulting in chain-elongation of the first product (Diender et al., 2019; Köpke and Simpson, 2020). A co-culture fermentation could increase the product spectrum of the fermentation (Köpke and Simpson, 2020). An acetogen that is particularly interesting is *Clostridium autoethanogenum* (*C. autoethanogenum*). This micro-organism can convert syngas to ethanol and 2,3-butanediol and can be used in co-culture fermentations (Abrini et al., 1994; Diender et al., 2019; Köpke et al., 2011b). An advantage of *C. autoethanogenum*, compared to other acetogens, such as *C.ljungdahlii*, is the higher ethanol-acetate selectivity that can be achieved without supplying additional H_2 (Li et al., 2019). Moreover, *C. autoethanogenum* is currently used on industrial scale for syngas conversion into ethanol and 2.3-butanediol by the company LanzaTech (Chen et al., 2018).

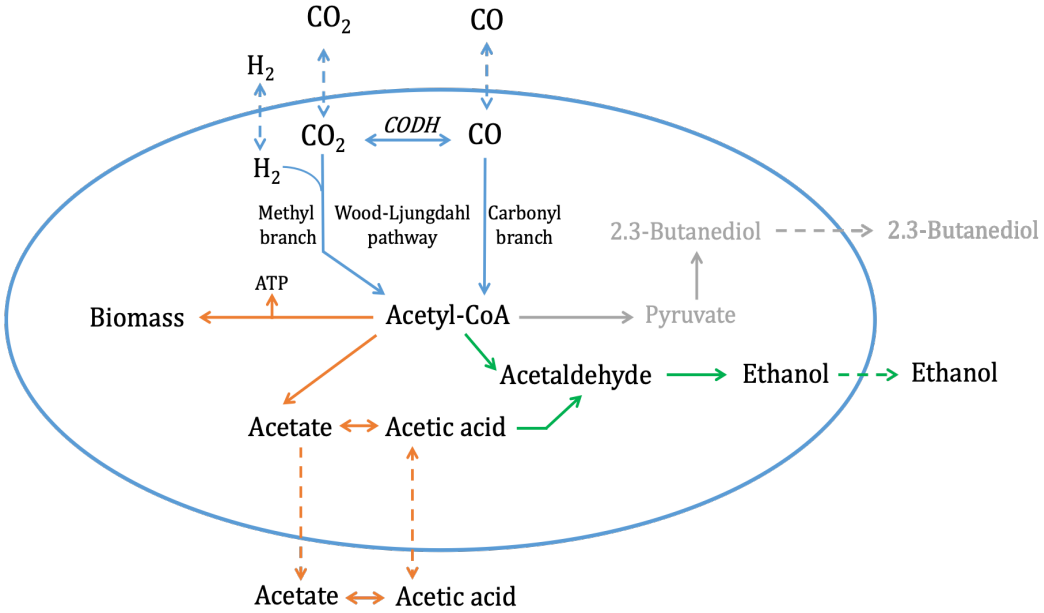

Figure 1.1: Schematic representation of metabolism of *C. autoethanogenum*. The blue lines indicate the Wood-Ljundahll pathway which reduces the CO_2 and CO to acetyl-CoA. The green and orange arrows indicate the acidogenesis and solventogenesis, respectively. Acidogenesis converts the acetyl-CoA to biomass and acetate and solventogenesis converts acetyl-CoA to ethanol. The dashed lines indicate the transfer of compounds over the cell membrane. The grey arrows indicate the production of 2.3-butanediol from acetyl-CoA. This figure as been adapted from Richter et al. (2016).

1.3 Reactor Configurations

Despite the aformentioned advantages of syngas fermentation process, several limitations are encountered which hamper the commercialization and scale-up of syngas fermentation (Yasin et al., 2019). The main drawbacks are poor gas-liquid mass transfer, low productivity and low cell density or growth of *C. autoethanogenum* (Yasin et al., 2019; Stoll et al., 2020). Mass transfer is very poor due to the low solubility of the gases present in syngas. Gas-liquid mass transfer is determined by, type of gaseous compound, the area over which mass transfer occurs and the driving force (Abubackar et al., 2011). A strategy to improve the mass transfer is to increase the volumetric mass transfer coefficient (k_La). One of the possible approaches to increase this coefficient is to improve the interfacial area (Munasinghe and Khanal, 2010b). For that purpose, several reactor configurations were examined which included: stirred tank reactors (STR), trickle bed reactors (TBR), hollow fibre membrane reactors (HFMBR), bubble columns (BCR) and gaslift reactors (GLR). The STR is a favoured bioreactor for scale-up, but for high gas-liquid mass transfer much mechanical agitation is required (Bredwell et al., 1999). The high power and cooling requirements caused by the mechanical agitation, make the STR not economical for syngas fermentation at a large scale (fig. 1.2a) (Yasin et al., 2019; Shen et al., 2014; Jones, 2007; Bredwell et al., 1999). Reactors without mechanical agitation are, trickle bed reactors, hollow fibre membrane reactors, bubble columns and gaslift reactors.

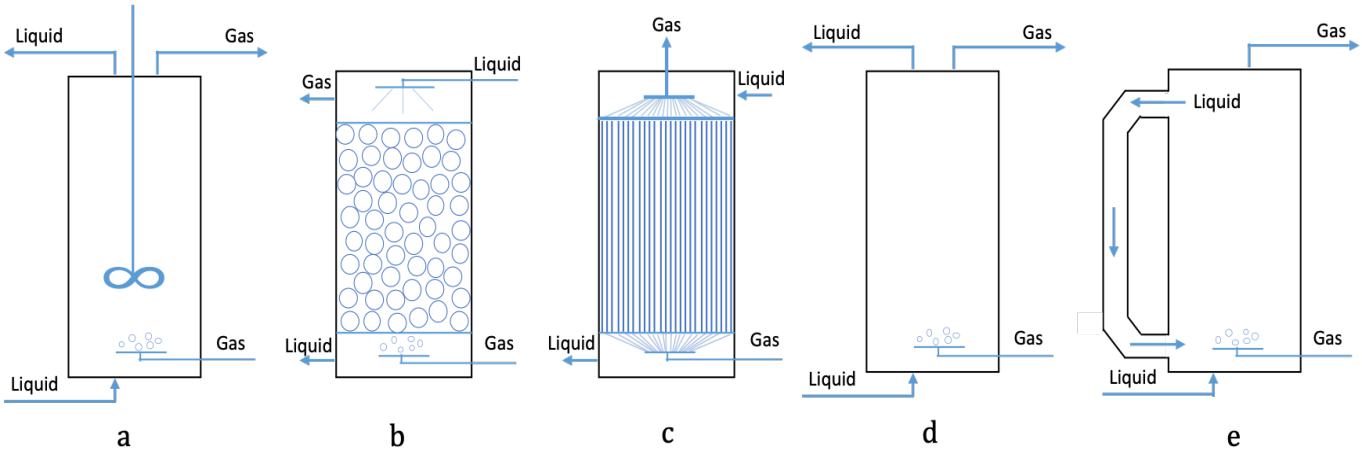

Figure 1.2: Schematic representation of bioreactors: a) Stirred Tank reactor (STR), **b)** Trickle-bed reactor (TBR), **c)** Hollow fibre membrane reactor (HFMBR), **d)** Bubble column reactor (BCR) and **e)** External loop gaslift reactor (ELGLR).

Trickle bed reactors are immobilized cell reactors where fermentation broth flows from the top of the reactor down on the immobilized cells, that are fixed in the reactor (fig. 1.2b). The gas-liquid transfer is increased due to the small liquid film that is in contact with the gas. In this reactor gas-liquid mass transfer ($k_L a$) of 421 1/h can be achieved (Orgill et al., 2013). Yet, the scalability of this reactor is very poor due to the low working volume which results in low production rates of chemical product (Stoll et al., 2020; Yasin et al., 2019).
The hollow fibre membrane reactor is an reactor which can even achieve higher gas-liquid mass transfer rates. In a HFMBR gas diffuses due to a concentration gradient through a membrane to the liquid phase where a biofilm can be attached that is able to convert the syngas (fig. 1.2c). A mass transfer coefficient up to 1096 1/h can be achieved with an HFMBR (Shen et al., 2014; Stoll et al., 2020). Although high transfer rates and biomass retention can be obtained, one of the drawbacks this reactor configuration is biofouling, which is caused by the thickness of the biofilm (Asimakopoulos et al., 2018). Another drawback is pore-wetting, in which liquid enters the membrane pores due to pressure gradients in the membrane which results in decrease of productivity (Datta et al., 2012; Stoll et al., 2020). Another important drawback is that the process is not available on commercial scale yet, so little is known about scale-up of hollow fibre membrane reactors for syngas fermentation (Asimakopoulos et al., 2018; Abubackar et al., 2011).
A reactor configuration that can obtain high interface surface areas is a bubble column reactor (BCR) (Munasinghe and Khanal, 2010a; Abubackar et al., 2011). A BCR is filled with a liquid phase and a gas phase is sparged at the bottom of the reactor (fig. 1.2d) (Abubackar et al., 2011; Shen et al., 2014). The bubbles that are sparged in this reactor create the large gas-liquid surface area and cause mixing of the liquid phase without mechanical agitation (Abubackar et al., 2011). The $k_L a$ that can be achieved in a BCR is up to 860 1/h and even 1800 1/h if the reactor is sparged with microbubbles (Bredwell and Worden, 1998). On large scale BCRs encounter mixing problems due to back-mixing which causes limited mass transfer, that results in microbial growth limitations. Next to this, BCRs have to be operated within a limited range of gas flow rates since high flow rates might induce bubble coalescence which reduces mass transfer as the interfacial area is decreased (Jones, 2007).
A variation on a bubble column reactor is a gaslift reactor. The liquid in a gaslift reactor is recirculated due to the density differences in the reactor. A gaslift reactor consists of a riser, which can be considered similar to a bubble column, and a downcomer. The riser and downcomer can be in one tank in which both parts are separated by a baffle or draught tube, this is referred to as an internal gaslift reactor. The riser and downcomer can also be two separate pipes, which is referred to as an external loop gaslift reactor (ELGLR) (fig. 1.2e). In this configuration the riser and downcomer are connected at the top by a gas separator and at the bottom of the riser and downcomer to create the loop (Chisti and Moo-Young, 1987; Merchuk and Garcia Camacho, 2010). In an ELGLR the gas is sparged in at the bottom of the riser, either at the beginning of the riser or more upwards in the riser, at the position of the outlet of the downcomer. In the riser the gas is transferred to the liquid. At the top of the riser the gas present in

the gas phase is separated from the liquid phase and the liquid flows into the downcomer. Hence, zero to almost no gas is present in the downcomer. This causes a higher density in the downcomer compared to the riser, which results in the circulation of the liquid in an ELGLR (Chisti and Moo-Young, 1987; Jones, 2007). Considering syngas fermentation in an ELGLR, the gas dissolves into the liquid where the micro organism, *C. autoethanogenum* is present that consumes the syngas. The gas mass transfer to the liquid and the reaction that is catalyzed by *C.autoethanogenum* occurs during the flow of liquid from the bottom to the top of the riser and in the flow of the downcomer. Consequently, no mass transfer is considered to occur in the downcomer. Compared to a bubble column reactor, in an ELGLR reactor a larger range of gas flow rates, better mixing, a uniform fluid direction and potentially higher gas-liquid mass transfer rates can be achieved (Chisti and Moo-Young, 1987; Jones, 2007). Moreover, a continuous ELGLR reactor is currently being used for syngas fermentation with *C. autoethanogenum* at industrial scale by the company LanzaTech.

1.4 Modelling of syngas fermentation

The potential high mass transfer coefficients that can be achieved in an ELGLR, could resolve the gas-liquid mass transfer limitation in syngas fermentation. Still, the low cell densities could cause low productivitiy. For lucrative use of the syngas fermentation process, further optimization is needed. On one hand, this can be accomplished by improving the microbe through genetic modifications (Daniell et al., 2012). By genetically modifying the micro-organism, the production pathways in *C. autoethanogenum* are altered to obtain high productivity and product on substrate yields (Köpke and Simpson, 2020). On the other hand, the process can be optimized by adjusting reactor parameters, such as reactor or external variable parameters.
In an ELGLR adjusting external variable parameters such as, biomass inlet concentrations and dilution rate in case of a continuous process, gas flow rate, pH, pressure and reactor parameters, such as length, diameter, gas sparger and specific surface area can improve the syngas fermentation in an ELGLR.
A model of an external loop gaslift reactor can simulate the reactor dynamics which can be used to examine the influence of, substrate gradients on the metabolism of *C. autoethanogenum*, examine biomass retention, to increase the amount of biomass in the reactor and optimize the productivities of the products formed by adjusting the external variable reactor parameters such as the dilution rate, gas/liquid inflow rate, pressure and temperature. In literature some models for syngas fermentation in reactors are proposed. The models proposed are often steady state one dimensional (1D) bubble columns with dimensionless kinetics of *C. autoethanogenum* (Chen et al., 2015, 2018; Li et al., 2019). Others only proposed models to examine and describe the global hydrodynamics, sometimes combined with local hydrodynamics, of gaslift reactors based on momentum and energy balances without incorporating a metabolic model or kinetic model of a micro-organism for a conversion process (Chisti et al., 1988; Verlaan, 1987; Young et al., 1991; Vial et al., 2002). de Medeiros et al. (2019) proposed a 1D dynamic model that uses the kinetics of *C. autoethanogenum*, based on experiments reported in literature, in a continuously stirred tank reactor to study the ethanol productivity and CO conversion. Siebler et al. (2020) compared syngas fermentation in a 1D and computational fluid dynamic (CFD) model (3D) bubble column model, to verify the accuracy of a less intensive computational model in terms of hydrodynamics. Next to this, Abrahamson (2019) modelled a 1D bubble column reactor and a CFD model of an ELGLR to study the LanzaTech syngas fermentation process. By studying the reactor hydrodynamics and the syngas fermentation process, the influence of the reactor hydrodynamics on the syngas fermentation process were identified, as well as the differences between 1D and 3D models. In addition, more insights were gained in the proprietary industrial scale syngas fermentation of the company LanzaTech.

1.5 Thesis goal and Approach

Currently no 1D model of an external loop gaslift reactor for syngas fermentation to produce ethanol with *C. autoethanogenum* is available yet. An 1D ELGLR model can aid in predicting the hydrodynamics of an external loop gaslift reactor and syngas fermentation parameters, such as: gas/liquid superficial velocities, gas/liquid hold-ups and ethanol productivity and conversion yield, respectively. The goal of this master thesis is to model a 1D external loop gaslift reactor to assess hydrodynamic parameters and the parameters involved in syngas fermentation with *C. autoethanogenum* by validation with experimental

data proposed in literature, and improve the syngas fermentation process through optimization of external variable parameters.
The 1D ELGLR model was considered to simulate a continuous process in which flow circulation, mass transfer and reactions occur. Due to the 1D geometry the hydrodynamics are described through equations and correlations proposed in literature. In addition the syngas conversion by *C. autoethanogenum* is described by an black-box approach. First the assumptions, structure and solution of the model are presented. Additionally, the characteristic hydrodynamic parameters that determine the reactor performance of an practical ELGLR were identified. Subsequently, the identified hydrodynamic parameters are validated with experimental data proposed in literature as well as with a CFD model. Furthermore, the syngas fermentation parameters, mass transfer, reaction rates and concentrations are compared to the same CFD model. Lastly, the syngas fermentation in the 1D ELGLR is optimized in terms of, ethanol productivity (g/L/h) and CO-to-ethanol conversion yield (%) through adjustment of external variable parameters: the dilution rate, gas inflow rates and inlet biomass concentrations.

Chapter 2

Modelling Approach

In this section the detailed modelling approach of the 1D external loop gaslift reactor is described. The geometry used to describe the ELGLR in the model is discussed first. Subsequently, the physics assumed to occur in an ELGLR are described. Thirdly, the correlations that describe the hydrodynamic parameters of an ELGLR and the microbial conversion of syngas are presented and argued. Then the model solution is explained as well as the modelling steps used to obtain the solution. Lastly, the approach to validate the model is discussed.

2.1 Geometry

The geometry selected for the external loop gaslift reactor model was one dimensional (1D). Other geometries, like 2D and 3D, are more computational intensive as these geometries are more complicated to solve compared to a 1D model (Mudde and Van Den Akker, 2001). The 2D and 3D geometries have the advantage of a more detailed and thus more accurate representation of a real external loop gaslift reactor over a 1D model. Computational fluid dynamics (CFD) are generally used in 3D geometries, in which continuity of momentum and mass are described by the Navier-Stokes equation. Additionally, CFD models incorporate flow characteristics of the multiphase flow present in an ELGLR, such as bubble induced turbulence, flow regimes and bubble dynamics (Mudde and Van Den Akker, 2001; Merchuk and Garcia Camacho, 2010). Nevertheless a 1D geometry is implemented, due to the computational intensity of a CFD model and the accuracy of a 2D model compared to a 1D model (Mudde and Van Den Akker, 2001) Additionally, a 1D model can be solved over time and can include a continuous process which is more complicated in 2D and 3D geometries.

A real external loop gaslift reactor consists of a riser, downcomer, gas separator, upper and lower part that connect the downcomer and riser (fig. 2.1a). To model the circulatory liquid flow in an external loop gaslift reactor, the 1D model is divided in four parts, inflow riser, riser, outflow riser and a downcomer (fig. 2.1b). In addition, the syngas fermentation in the gaslift reactor is considered to be continuous. For simplicity in the 1D geometry modelling, the horizontal lower and upper part that connect the downcomer and riser are not considered in the 1D gaslift model.
The height and diameter of the riser were initially based on the reactor of Li et al. (2019). The length of the downcomer was set equal to the height of the riser. The diameter of the downcomer was derived from the riser diameter and the downcomer-to-riser area ratio derived from a LanzaTech patent (Li et al., 2017). The inflow riser represents the part of the riser before the gas sparger. Whereas the outflow riser is used to describe the riser part above the upper connecting part of an external loop gaslift reactor. The length of the inflow and outflow riser is considered small, 0.04 meter, as the two parts are considered to be a part of the riser in a real ELGLR (fig. 2.1bb).

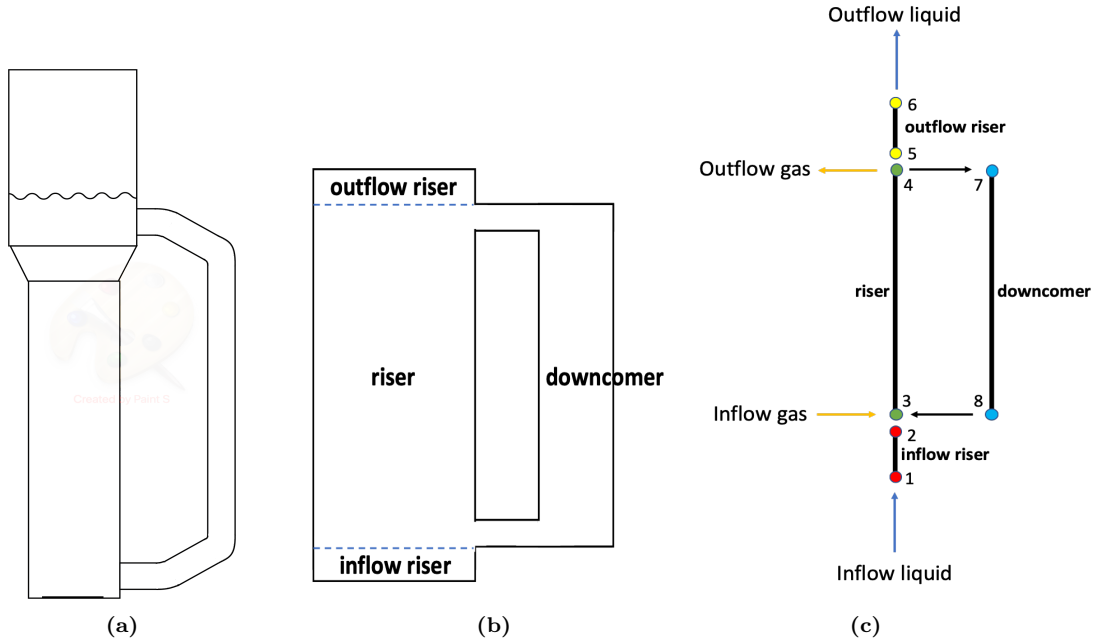

Figure 2.1: Schematic representation of **a)** industrial ELGLR and **b)** its representation in the model **c)** its representation int the model interface, with the four different reactor parts. The numbers represent the boundaries of each of the four parts. The blue arrows indicate the liquid in and outflow of the reactor. The yellow arrows indicate the gas in and outflow in the riser.

2.2 Model equations

In this section the equations used to describe the model are elaborated. Firstly, the general model equation is explained. Subsequently, the model equations and assumptions for the four different reactor parts are discussed. Lastly, the hydrodynamic and microbial conversion parameters that are described by correlations from literature are discussed. A schematic representation of the ELGLR model with corresponding boundaries is presented in figure 2.1c.

General model equation

The 1D ELGLR is based on the physical convection-dispersion equations or tranpsort equations (eqn. 2.1). The equations describe the transport of a species in a physical system through convection and dispersion. The convective term or flux describes the change in concentration of a the specie over the length of a volume with a certain velocity. The velocity applied in the equations of this study is the superficial velocity (u). The superficial velocity is described as the volume of a phase (gas or liquid) per surface area of the reactor per second ($m^3_G/m^2_R/s$ or $m^3_L/m^2_R/s$) The dispersion term or flux describes the change in concentration of a specie over the length of a volume in two directions. The dispersion coefficient (D_G or D_L) describes the amount of dispersion that occurs in the surface area of the reactor per second (m^2_R/s). In the ELGLR model two phases are considered, a gas and liquid phase. Mass transfer from the gas to the liquid phase is modelled and the model equations are proposed for each chemical specie considered in the model. Due to the use of correlations and two phases, several parameters were corrected with the gas and liquid hold-up (m^3_G/m^3_R or m^3_L/m^3_R). The units of the model equations are either in $mol/m^3_G/s$ or $mol/m^3_L/s$.

$$\frac{\partial C_i}{\partial t} = -u\frac{\partial C_i}{\partial x} + D\frac{\partial^2 C_i}{\partial x^2} + S_i \tag{2.1}$$

2.2.1 Inflow riser

The inflow riser represents the small part of the riser before the downcomer exit in the riser (fig. 2.1c). The inflow riser was modelled to simulate the continuous flow of biomass that flows into the reactor. High dispersion ($D_{L_{ir}} = 1 \cdot 10^6$ m^2/s) was assumed to occur due to the dimensions of the inflow riser. The superficial velocity present in the convective term of the equation ($u_{L_{ir}}$) was determined by the volumetric flowrate ($F_{L_r,in}$ m^3_L/s) and the surface area of the riser (A_r (m^2_R)). The $F_{L_r,in}$ was defined by the dilution rate (D_{il} (1/s)) and the liquid volume in the reactor (V_L (m^3_L)) (Appendix B). Only a liquid phase was assumed in the inflow riser, since the gas sparger is modelled to be higher in the riser (fig. 2.1c). Therefore, the liquid hold-up (ε_{L_ir}) was 1 (eqn. 2.2). A Dirichlet boundary condition was applied at the inlet of the inflow riser (eqn. 2.3). The boundary condition at the outlet was a Neumann boundary condition, convective outflow (eqn. 2.4)(Mazumder, 2016).

$$\frac{\partial C_{L_{ir},i}}{\partial t} = -u_{L_{ir}} \frac{\partial C_{L_{ir},i}}{\partial x} \qquad \text{with} \qquad i = \text{X} \tag{2.2}$$

$$C_{L_{ir},i}(0,t) = C_{0,L_{ir},i} \qquad \text{with} \qquad i = \text{X} \tag{2.3}$$

$$\frac{\partial C_{L_{ir},i}(x,\, t)}{\partial x} = 0 \qquad \text{with} \qquad i = \text{X} \quad \text{and} \quad x = L_{ir} \tag{2.4}$$

2.2.2 Riser

The riser incorporates a gas and liquid phase. Both phases are modelled by individual convection-dispersion equations. Consequently, both the gas phase and liquid phase are discussed individually.

Gas phase

The gas is sparged into the liquid in the riser (fig. 2.1c). The species considered in the gas phase are CO and N_2, since no accurate model is available yet to describe the use and conversion of all of gaseous compounds in syngas (CO, H_2 and CO_2). In the model an equimolar gas mixture of CO and nitrogen (N_2) is used.

$$\frac{\partial C_{G_r,i}}{\partial t} = -\frac{1}{\varepsilon_{G_r}} \frac{\partial C_{G_r,i} u_{G_r}}{\partial x} - \frac{k_L a \Delta C_{L_r,i}}{\varepsilon_{G_r}} \qquad \text{with } i = \text{CO} \tag{2.5}$$

$$C_{G_r,i}(0,t) = C_{0,G_r,i} \tag{2.6}$$

$$\frac{\partial C_{G_r,i}(x,\, t)}{\partial x} = 0 \qquad \text{with} \qquad i = \text{CO} \quad \text{and} \quad x = L_r,\, 0 \tag{2.7}$$

The equation used to model CO in the gas phase included convection and dispersion initially (eqn. 2.5). The correlation for the gas dispersion coefficient presented by Heijnen and van 't Riet (1984) was verified to be applicable for the gas phase dispersion in the model. However, the model did not solve correctly with the gas dispersion correlation, therefore the gas dispersion coefficient was assumed to be zero (D_{G_r} = 0) and thus the dispersion term was neglected.
The superficial gas velocity (u_{G_r}) in the convection term, was considered to change over the length of the riser and thus is a function of x. The superficial gas velocity was derived from equation 2.5 by assuming steady state (Appendix B). The superficial gas velocity increases due to decreasing hydrostatic pressure and decreasing overall mass transfer (eqn. 2.8). Due to the varying superficial gas velocity over the length of the riser, the superficial gas velocity is included in the convective partial differential term. Dispersion is considered due to the large riser diameter and high superficial gas velocity that was calculated (Shah

et al., 1982). However, the gas phase in gaslift reactors often is considered to be plug flow, yet plug-flow is not applicable for all external gaslift reactors (Young et al., 1991). In addition, little research has been conducted on gas dispersion correlations (Chen et al., 2015; Li et al., 2019; van't Riet and van der Lans, 2011; Merchuk and Garcia Camacho, 2010). The boundary condition for the gas phase at the inlet of the riser is a concentration contraint or Dirichlet boundary condition (eqn. 2.6). At the outlet of the riser a Neumann boundary condition was applied (eqn. 2.7)(Mazumder, 2016).
The gas hold-up (ε_{G_r}) was included in the equation, to consider two phases in the riser. The correlation suggested to describe the gas hold-up is explained and clarified in section 2.3. The mass transfer term in equation 2.5 was used to describe the transfer of the gaseous compounds to the liquid phase in the riser. Further elaboration on the parameters k_L and a in the mass transfer term is presented in section 2.3. The concentration difference denoted with ΔC_{L_r}, is the difference between the saturation concentration of the gaseous compound in liquid (C^*) and the dissolved concentration of the gaseous compound. The saturation concentration is determined with Henry's law (Appendix B). In addition, the pressure used in equation 2.5 is considered to vary over the height of the riser due to decreasing hydrostatic pressure towards the top of the column. The pressure was described by the difference in density and position in the riser (equation 2.9). The derivation of equation 2.9 is presented in (Appendix B).

$$\frac{du_{G_r}}{dx} = \frac{\rho_G g u_{G_r}}{P} - \frac{RT}{P}\sum_i (k_{L,i} a \Delta C_{L_r,i}) \tag{2.8}$$

$$P(x) = g(\rho_L \varepsilon_L + \rho_G \varepsilon_G)(L - x) \tag{2.9}$$

Liquid phase

The species considered in the liquid of the riser are: the dissolved gaseous compounds CO and N_2, biomass (X) and ethanol (EtOH). Other products from syngas fermentation by *C. autoethanogenum* are not considered as there is no accurate model available to describe the complete syngas fermentation.
The model equation for the dissolved gaseous compound included convection, dispersion, a mass transfer term, since the gaseous compound is transferred from the gas to the liquid phase and a reaction term. The equations for biomass (X) and ethanol (EtOH) were similar to the equations of the dissolved gaseous compounds, except for the mass transfer term which was not included in these equations 2.10. The liquid hold-up (ε_{L_r}) was included in the model equations for the liquid phase, regarding the two phases in the riser. The liquid hold-up in the riser is determined with the gas hold-up by 1-ε_{G_r}. The reaction term is described by the parameters, biomass specific rate ($q_{r,i}$) and the biomass concentration in the liquid ($C_{L_r,X}$). The biomass specific rate is further elaborated in section 2.3.

$$\frac{\partial C_{L_r,i}}{\partial t} = -\frac{u_{L_r}}{\varepsilon_{L_r}}\frac{\partial C_{L_r,i}}{\partial x} + D_{L_r}\frac{\partial^2 C_{L_r,i}}{\partial x^2} + \frac{k_L a \Delta C_{L_r,i}}{\varepsilon_{L_r}} \pm q_{r,i} C_{L_r,X} \quad \text{with} \quad i = \mathrm{CO, EtOH, X} \tag{2.10}$$

$$u_{Lr} = u_{Lir} + u_{Lr} \tag{2.11}$$

Due to the recirculation of liquid in an ELGLR, convection in the liquid phase is assumed. The superficial liquid velocity in the convective term was described by the correlation for liquid circulation velocity in the riser proposed by Chisti et al. (1988). To simulate the continuous inflow of biomass, the superficial liquid in the riser was described as a function of the liquid velocity predicted with the correlation as well as the inflow velocity (eqn. 2.11). The dispersive term was included in the model equation, since the velocity of the liquid flow and the gas flow are assumed to induce dispersion. The dispersion coefficient correlation proposed by Heijnen and van 't Riet (1984) was used to describe the dispersion. In section 2.3 the superficial liquid velocity and dispersion coefficient are further elucidated.
The flow going into the riser is considered to be the sum of the outflow from the inflow riser and the

outflow from the downcomer(fig. 2.1c). The boundary condition for the inlet of the riser is assumed to be a Danckwerts boundary condition (Danckwerts, 1953). The concentration at the inlet boundary condition was derived from the two flows coming from the inflow riser and downcomer. The derivation of the concentration at the inlet of the riser is further elaborated in (Appendix B) (eqn. 2.12). The boundary condition for the outlet of the riser is considered to be a Neumann boundary condition, hence no dispersion is assumed at the boundary (eqn. 2.14) (Mazumder, 2016).

$$C_{L_r,i}(0,t) = u_{L_r}\, C_{L_r,i} - D_{L_r} \frac{\partial C_{L_r,i}}{\partial x} \qquad \text{with} \quad i = \text{CO, X, EtOH} \tag{2.12}$$

$$C_{L_r,i}(0,t) = \frac{C_{L_d,i}(0,t)\, A_d\, u_{L_d} + C_{L_{ir},i}(L_{ir},t)\, A_r\, u_{L_{ir}}}{A_r\, u_{L_r}} \tag{2.13}$$

$$\frac{\partial C_{L_r,i}(L_r,\, t)}{\partial x} = 0 \tag{2.14}$$

2.2.3 Downcomer

The downcomer only considers a liquid phase, as it is assumed that gas is separated from the liquid and vented of at the outlet of the riser. Only dissolved gaseous compounds are considered to be existent in the downcomer. Model equations for the downcomer included a convection term and reaction term, for the species CO, biomass and ethanol (eqn. 2.15).

$$\frac{dC_{L_d,i}}{dt} = -u_{Ld} \frac{\partial C_{L_d,i}}{\partial x} + q_{d,i} C_{L_d,X} \qquad \text{with} \qquad i = \text{CO, X and EtOH} \tag{2.15}$$

Since no gas is assumed in the downcomer $\varepsilon_{L_d} = 1$. The superficial liquid velocity in the downcomer was proposed to be a resultant of the superficial liquid velocity in the riser, to represent the continuum of the liquid in the reactor (Chisti et al., 1988). The correlation suggested to describe the superficial liquid velocity in the downcomer is clarified in section 2.3. The flow in the downcomer was assumed to be of plug-flow type, due to the one phase flow (Chisti and Moo-Young, 1987; Verlaan et al., 1986). Hence, the dispersion coefficient in the downcomer is assumed to be zero (($\mathrm{D}_{L_d} = 0$). The reaction term is similar to the riser and biomass specific reaction term is further elucidated in 2.3.
The boundary condition at the inlet of the downcomer is a Dirichlet boundary condition. To represent the continuum of the liquid flow from the riser into the downcomer, the concentrations of the species in the liquid from the riser should equal the concentrations of the species in the liquid entering the downcomer (eqn. 2.16). The outlet of the downcomer is considered to be a Neumann boundary condition or a convective outflow of liquid, since the liquid is recirculated in from the downcomer back into the riser (eqn. 2.17)(Mazumder, 2016).

$$C_{L_d,i}(0,t) = C_{L_r,i}(L_r,t) \qquad \text{with} \qquad i = \text{CO, X, EtOH} \tag{2.16}$$

$$\frac{\partial C_{L_d,i}(x,\, t)}{\partial x} = 0 \qquad \text{with} \quad x = L_d,\, 0 \tag{2.17}$$

2.2.4 Outflow riser

The outflow riser represents the small part of the riser above the downcomer entrance at the top of the riser (fig. 2.1b). The outflow riser was modelled to simulate the continuous flow in the external loop gaslift reactor. It is assumed that almost all flow from the riser enters the downcomer, except for a small part of the flow which exits at the outflow riser. As a result, superficial liquid velocity of the outflow riser

($u_{L_{or}}$) is assumed to be equal to the superficial liquid velocity in the inflow riser ($u_{L_{ir}}$). In addition, very high dispersion ($D_{L_{or}} = 1 \cdot 10^6$ m^2/s) was assumed to occur due to the dimensions of the outflow riser. A reaction term was included in the model equation due to the liquid flow of this part being similar to the liquid flow in the riser. The biomass specific rate ($q_{or,i}$) is further specified and elaborated in section 2.3. Only a liquid phase was assumed in the outflow riser, since the gas is assumed to be vented off before entering the outflow riser part, resulting in a liquid hold-up (ε_{L_or}) of 1 (eqn. 2.18). A Dirichlet boundary condition was used to describe the inlet of the outflow riser (eqn. 2.19). To simulate the continuum of the liquid, the concentration of the compounds present in the liquid at the outlet of the riser part should equal the concentration of the compounds in the liquid that enters the inlet of the outflow riser part. At boundary of the outlet a Neumann boundary condition was applied (eqn. 2.20) (Mazumder, 2016).

$$\frac{dC_{L_{or},i}}{dt} = -u_{L_{or}} \frac{\partial C_{L_{or},i}}{\partial x} + q_{or,i} C_{L_{or},X} \qquad \text{with} \qquad i = \text{CO, X, EtOH} \tag{2.18}$$

$$C_{L_{or},i}(0,t) = C_{L_r,i}(L_r,t) \tag{2.19}$$

$$\frac{\partial C_{L_{or},i}(x,\, t)}{\partial x} = 0 \qquad \text{with} \qquad x = L_{or} \tag{2.20}$$

2.3 Specific model equations and model parameters

The geometry of the external loop gaslift reactor model is 1D. Real external loop gaslift reactors involve hydrodynamics since hydrodynamic parameters in different parts of the reactor are interrelated (Siegel and Merchuk, 1988; Jones, 2007). The hydrodynamics of an external loop gaslift reactor are approached in the model with correlations proposed in literature. The correlations used to describe the hydrodynamic parameters are discussed first. Secondly, the syngas fermentation parameters are discussed.

2.3.1 Hydrodynamic parameters

The hydrodynamic parameters are discussed in order of appearance in the model equations. The hydrodynamic parameters occurring in the gas phase as well as in the liquid phase are elucidated individually.

Superficial liquid velocity riser

The superficial liquid velocity in the riser (u_{L_r}) is described by the correlation proposed by Chisti et al. (1988) (eqn. 2.21). Chisti et al. (1988) derived the superficial liquid velocity in the riser from the energy balance. The input of energy into the riser was equalled to the energy dissipation occurring in the entire reactor (Chisti et al., 1988). The correlation is simplified by neglecting the wall friction, due to the substantial higher friction obtained from bubble wakes and flow around bends in the reactor (Chisti et al., 1988). The gas hold-up of the riser and downcomer are used in the correlation instead of the gas flow rate. The gas hold-up is used since the hold-up is dependent on liquid properties as well (Chisti and Moo-Young, 1993). The friction loss coefficient (K_B) for external loop gaslift reactors is proposed by Chisti et al. (1988) to be 5. Yet, K_B is highly dependent on the reactor geometry. Correct estimation of the friction loss coefficient can be achieved by experiments with a real external loop gaslift reactor. Therefore, a sensitivity analysis was performed, see Appendix D. The correlation was validated with experimental data available in literature and predicted the superficial liquid velocity accurate, within a 30 % range (Chisti et al., 1988).

$$u_{Lr} = \left[\frac{2gL_r \left(\varepsilon_{L_r} - \varepsilon_{L_d}\right)}{K_B \left(\frac{1}{(1-\varepsilon_{L_r})^2} + \left(\frac{A_r}{A_d}\right)^2 \frac{1}{\left(1-\varepsilon_{L_d}\right)^2} \right)} \right]^{0.5} \tag{2.21}$$

Superficial liquid velocity downcomer

The superficial velocity in the downcomer (u_{L_d}) was determined with the superficial liquid velocity in the riser, to represent the continuum of the liquid (eqn. 2.22. The superficial liquid velocity in the downcomer is determined by u_{L_r} and the riser-to-downcomer specific area ($\frac{A_r}{A_d}$) (eqn. 2.23)

$$A_d u_{L_d} = A_r u_{L_r} \tag{2.22}$$

$$u_{L_d} = \frac{A_r}{A_d} u_{L_r} \tag{2.23}$$

Liquid dispersion coefficient

The liquid dispersion coefficient (D_L) correlation proposed by Heijnen and van 't Riet (1984) is initially used to describe liquid dispersion in bubble columns. The correlation is applicable for high superficial liquid velocities (< 2.8 m/s) and in bubble columns with large diameters (<7.5 m) (Heijnen and van 't Riet, 1984). Due to the applicability of the correlation proposed by Heijnen and van 't Riet (1984) and the little dispersion coefficient correlations present in literature, the correlation proposed by Heijnen and van 't Riet (1984) was used to describe the liquid dispersion coefficient in the external loop gaslift reactor (eqn. 2.24).

$$D_{\mathrm{L_r}} = 0.33 \left(g D_r^4 u_{\mathrm{G_r}}\right)^{1/3} \tag{2.24}$$

Gas hold-up riser

In an ELGLR the gas hold-up (ε_{G_r}) influences the liquid recirculation (Merchuk and Garcia Camacho, 2010). Due to the interdependence of the superficial liquid velocity and the gas hold-up in the riser, the correlation introduced for the iterative procedure by Chisti and Moo-Young (1993) was used. The gas hold-up was derived from experimental data by Hills (1976) (eqn. 2.25). The correlation is initially used for the determination of gas hold-up in bubble columns. However, due to the similarity between the upflow of gas and liquid in the riser of an gaslift reactor and a bubble column, the correlation is found to be applicable (Chisti and Moo-Young, 1993).

$$\varepsilon_{G_r} = \frac{u_{G_r}}{0.24 + 1.35 \left(u_{G_r} + u_{L_r}\right)^{0.93}} \tag{2.25}$$

Volumetric liquid mass transfer coefficient

Correlations describing the volumetric liquid mass transfer coefficient ($k_L a$) are described by many researchers as reviewed by Chisti and Moo-Young (1987). However, the applicability of the correlations is often in a very specific range of parameters (Chisti and Moo-Young, 1987). Hence, the liquid mass transfer coefficient (k_L) and interfacial area (a) are described by individual correlations in the model. For the mass transfer of the gaseous compounds from the gas to the liquid phase, only liquid side mass transfer is incorporated. Since, mass transfer at the liquid side encounters more resistance due to the solubility of the gaseous compound in the liquid (Garcia-Ochoa and Gomez, 2009) (fig. 2.2).

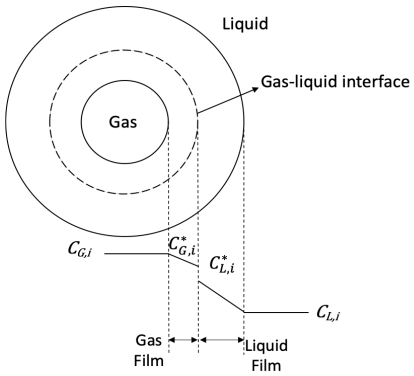

Figure 2.2: Gas-Liquid interface of gas bubble in liquid.

Heijnen and van 't Riet (1984) proposed an equation based on Higbie's penetration theory for the liquid mass transfer coefficient in bubble columns. The equation is assumed to be accurate for the 1D ELGLR model, since k_L is mainly determined by the bubble diameter (d_b) (Heijnen and van 't Riet, 1984;

Calderbank and Moo-Young, 1995). Furthermore, the correlation was proposed for a specified bubble diameter range (1-10 mm) which is applicable in this model.

$$k_{\mathrm{L,i}} = 1.13 \left(\frac{v_{\mathrm{b}}\, D_{\mathrm{if}}}{d_{\mathrm{b}}} \right)^{0.5} \qquad \text{with} \quad i = \mathrm{CO} \tag{2.26}$$

The interfacial area equation is derived from the ideal gas law and applied by various others (Shah et al., 1982; Bello et al., 1985; Heijnen and van 't Riet, 1984). In this correlation the bubble diameter (d_b) and gas hold-up determine the interfacial area, which results in the dependency of the volumetric mass transfer coefficient on the gas bubbles in the riser.

$$a = \frac{6\varepsilon_{Gr}}{d_b} \tag{2.27}$$

Bubble rise velocity

The bubble rise velocity (v_b) was initially described by a correlation for a spheroid bubble in a stagnant liquid proposed by Park et al. (2017). However, the correlation was dependent on the bubble diameter (d_b), which caused circular dependence of the d_b and v_b correlations. In addition, the v_b varies very little in a bubble diameter range of (1-10 mm) (Park et al., 2017). As a result, v_b is assumed constant.

Bubble diameter

The bubble diameter (d_b) is assumed to change over the length of the riser due to decrease of hydrostatic pressure and mass transfer. Therefore, bubble diameter correlation that was presented and applied to the bubble column model of Li et al. (2019) was considered. The bubble diameter correlation is derived from the ideal gas law and is dependent on the molar flowrate (n_G (mol/s)) and hydrostatic pressure. The molar flowrate is described by the superficial gas velocity and the CO concentration in the gas and changes over the length of the riser due to the superficial gas velocity.

$$d_b = d_{b,0} \sqrt[3]{\frac{P_L}{P} \frac{n_G}{n_{0,G}}} \qquad \text{with} \quad n_G = u_{G_r} A_r C_{G_r} \quad \text{and} \quad C_{G_r}(x) = \sum_{i=\text{all gases}}^{\infty} C_{G_r,i}(x) \tag{2.28}$$

2.3.2 Microbial conversion parameters

The parameters used to describe the conversion of syngas to ethanol with *C. autoethanogenum* are based on a thermodynamical black-box approach and CO uptake kinetics for *C. ljungdahlii* proposed by Mohammadi et al. (2014). A black-box approach is implemented since no proper model to describe the metabolism of *C. autoethanogenum* is available yet. In the black-box approach linear relations between catabolism, anabolism and maintenance are obtained from the elemental conservation balances and Gibbs free energy balances (Kleerebezem and Van Loosdrecht, 2010). In Appendix C, catabolism, anabolism and metabolism equations are reported. Similarly, the biomass specific production rates and microbial growth are formulated according to the black-box approach (eqns. 2.29 and 2.30). The reaction terms presented in section 2.3 are determined with equations 2.29 and 2.30. The specific biomass rates as well as the specific growth rate are calculated individually for each part of the ELGLR in which the term occurs. Subsequently, the biomass specific rates together with the biomass concentration in the specific reactor part are used to calculate the reaction rates (eqn. 2.31).

$$\mu = \frac{q_{CO} - m_{s,CO}}{Y_{CO/X}^{Met}} \tag{2.29}$$

$$q_i = Y_{i/X}^{MET} \cdot \mu - m_{s,i} \qquad \text{with} \quad i = \text{EtOH} \tag{2.30}$$

$$R_i = q_i \cdot C_x \qquad \text{with} \quad i = \text{CO, EtOH and X} \tag{2.31}$$

Mohammadi et al. (2014) experimentally obtained CO uptake rates and fitted the data to two different uptake models with an CO inhibition term (K_I). Additionally, an ethanol inhibition term (I_{et}) proposed by Puiman (2020) was included since growth of *C. autoethanogenum* is inhibited by ethanol (eqn. 2.32) (de Medeiros et al., 2019; Puiman, 2020). Although, the CO uptake model suggested by Mohammadi et al. (2014) is presented for the microbe *C. ljungdahlii* it is currently the best available model to describe the CO uptake kinetics of *C. autoethanogenum*. Nevertheless, the model is controversial since the experiments performed by Mohammadi et al. (2014) did not incorporate dissolved concentrations of gaseous compounds or microbial consumption of substrate (Jang et al., 2017).

$$q_{CO} = q_{\max,CO} \, \frac{C_{L,\text{CO}}}{K_s + C_{L,CO} + C_{L,CO}^2/K_I} \, I_{et} \qquad \text{with} \qquad I_{et} = 1 - \frac{C_{L,et}}{K_{I,et}} \tag{2.32}$$

2.4 Model solution

The 1D external gaslift model is developed and solved in the simulation software COMSOL Multiphysics 5.4. The *transport of diluted species* interface in COMSOL Multiphysics is used to describe the species in each of the four parts of the model since this interface uses the convection-dispersion transport equations. The differential equation of the superficial gas velocity is solved with the convection-diffusion equation from the *mathematical partial differential* interface. All the partial differential equations are numerically solved using the finite element method, wherein the geometry is divided into small intervals. At the nodes, the partial differential equations are solved. The stability of the solver and the accuracy of the solution increases by increasing the number of nodes. The nodes or mesh, as termed in COMSOL Multiphysics was altered for the four different intervals of the 1D model. The mesh in the inflow and outflow riser intervals was increased from 1 to 5 elements. The mesh of the riser interval was increased from 1 to 250 elements with a symmetric distribution of elements to increase the accuracy of the solution at the boundaries of the riser. Similarly, the mesh of the downcomer was adjusted from 1 to 100 elements with a symmetric distribution of elements (fig. 2.3). The relative tolerance was set to 0.005 to obtain an accurate solution with an acceptable solution time of around 1 minute on 4 CPUs.

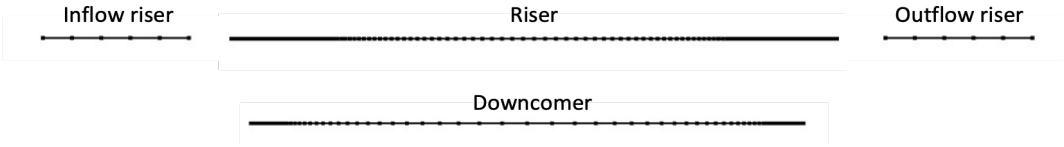

Figure 2.3: Mesh of 1D ELGLR model for each reactor part.

The solution of the model was obtained through several modelling steps. Firstly, a global function is minimized with the Nelder-Mead optimization method to obtain u_{L_r} and ε_{G_r} (Appendix B). The solutions of u_{L_r} and ε_{G_r} are used as parameter in the physic interfaces of the next step, the time dependent solver. The equations in physical interfaces are solved time-dependent with an automatic (highly) non-linear Newton solver with default settings. Additionally the physic interfaces are solved at steady state (stationary study) with the automatic highly non-linear Newton, to verify whether the dynamic solver was solved correctly (fig. 2.4). The implementation of several hydrodynamic parameter correlations caused the model not to solve. Consequently, conditional statements were implemented to solve the model (Appendix E). The time to solve the model was set at 5 days to assure steady state was reached.

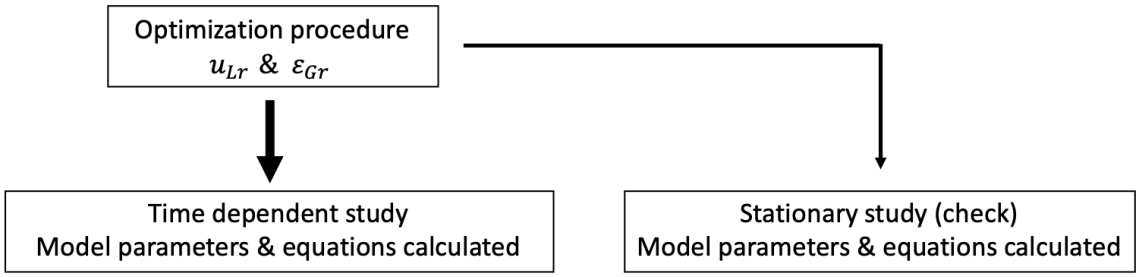

Figure 2.4: Order of steps taken to solve 1D model.

2.5 Model Validation

The application of different correlations in the model to describe syngas fermentation in an ELGLR approximates the process in an actual ELGLR. To verify the accuracy of the model, the hydrodynamic parameters predicted with the 1D ELGLR model are compared to experimental data from Vial et al. (2002) and Young et al. (1991) and a computational fluid dynamics model (CFD) from Abrahamson (2019). Additionally, the syngas process parameters that were predicted with the CFD model: CO uptake rate ($q_{r,co}$), CO mass transfer ($R_{tr,co}$) rate and dissolved CO concentration ($C_{L_r,co}$), are compared with the 1D ELGLR model as well. A comparison between two models was performed to verify the accuracy of a less detailed model (1D) with a highly detailed model (CFD). In addition, the 1D model was optimized for the external variable parameters: dilution rate (D_{il}), gas mass inflow rate (m_{in}) and biomass inlet concentration ($C_{L_{ir},X,0}$), to obtain the most optimal configuration of the 1D model to achieve high ethanol productivity and CO conversion yield. In addition, the obtained ethanol productivity and CO conversion yield are compared to the rough estimation of the same parameters for the industrial process of LanzaTech. In addition only the mass transfer, reaction rates and concentrations in the riser are considered since biomass is fed continuously to the reactor and the values of the downcomer are a resultant of the values predicted in the riser. For all comparisons and parametric analysis the time set to solve the model was 5 days to ensure the steady state in the reactor. The data of the 1D model used in the comparisons are at the last time point, unless differently stated.

In the 1D model the hydrodynamic parameters, u_{Lr}, u_{Gr}, ε_{Gr} and u_{Ld}, are considered to mainly describe the process of an ELGLR. The hydrodynamic parameters obtained by Young et al. (1991) and Vial et al. (2002) are measured at different gas inlet velocities. For the comparison, the same reactor geometry and inlet superficial gas velocities are implemented in the 1D model (table 2.4, 2.1) (Appendix B) (table 2.4). In addition, the microbial conversion and mass transfer of the 1D model were not solved for when solving for the hydrodynamic parameters (fig. 2.4). The inlet superficial gas velocities from the experimental data were converted to mass flowrates (kg/s) for the 1D model to achieve the same inlet superficial gas velocities (table 2.1) (Appendix B). The experimental data is obtained through visual observations from plots. The local parameters u_{Lr}, u_{Gr}, ε_{Gr} and u_{Ld} obtained by Young et al. (1991) were converted to global values by correction with the gas and liquid hold-up, respectively, for the comparison to the predicted parameters from the 1D model. For the comparison with the data from Vial et al. (2002) only the global measured parameters are considered, u_{Lr}, ε_{Gr} and u_{Ld}. The superficial liquid velocity was reported at a different inlet gas velocity, at 4.3 cm/s in stead of 3.7 cm/s, therefore this was applied in the 1D model too (table 2.1). The hydrodynamic parameters predicted with the CFD model were time-averaged and obtained from the 2D surface plots of Abrahamson (2019). For the comparison the average of the parameter over the diameter of the reactor was considered. Similarly to the comparison with Young et al. (1991); Vial et al. (2002) the inlet superficial gas velocity of the CFD model was implemented in the 1D model (table 2.1). The inlet superficial gas velocity applied by For the 1D model, the superficial liquid velocity and gas hold-up are calculated for a single point in the reactor and therefore are constant over the length of the riser. The superficial gas velocity in the 1D model is calculated over the riser height, yet for comparison the average of the superficial gas velocity is considered.

Table 2.1: Inlet superficial gas velocities of experimental data and CFD model

	Young et al. (1991)	Vial et al. (2002)	Abrahamson (2019)
Inlet superficial gas velocities (cm/s)	0.96	1.2	-
	2.1	3.7 or 4.3	-
	4.7	6.6	-
	8.2	11.7	9.78

Furthermore, for the comparison between the CFD and 1D model, both the ε_{Gr} were predicted with the ε_{Gr} correlation proposed by Bello et al. (1985) to check which model predicted the hold-up more accurate.

$$\varepsilon_{Gr} = 0.16\Big(\frac{u_{Gr}}{u_{Lr}}\Big)^{0.57}\big(1+\frac{A_d}{A_r}\big) \tag{2.33}$$

The process parameters identified in this study to describe the performance of syngas fermentation are the ethanol productivity (g/L/h) and CO-to-ethanol conversion yield (%). In the CFD model a thermodynamic black-box model and CO uptake kinetics from Mohammadi et al. (2014) are considered. However, the ethanol productivity and CO-to-ethanol conversion yield were not discussed, yet the factors that influence the process parameters, the mass transfer and CO uptake rates as well as the dissolved CO concentration, are discussed. Therefore, these factors are used to examine the performance of the syngas fermentation process. Moreover, the external variable parameters D_{il}, (m_{in}) and $C_{L_{ir},X,0}$, were varied respectively to examine at which values these parameters contribute to high ethanol productivity and CO conversion yield. In addition the ethanol productivity and CO conversion yield of the industrial LanzaTech process are roughly estimated with the little data presented by LanzaTech and through approximations. All the parameters that were considered in the optimization from the 1D model were averages of that specific parameter over the length of the riser at the last time point t = $4.32{\cdot}10^5$ s.

2.6 Table Parameters

Table 2.2: Parameters used to model ELGLR. The parameters calculated for the model are described in the appendices.

	Symbol	Value	Unit	Reference
General				
Gravitational constant	g	9.81	m^2/s	Janssen and Warmoeskerken (1987)
Temperature	T	310	K	Li et al. (2019)
Boltzmann constant	k_B	$1.3806 \cdot 10^{-23}$	J/K	Janssen and Warmoeskerken (1987)
Gas constant	R	8.3145	J/(mol K)	Janssen and Warmoeskerken (1987)
Reactor				
Pressure atmospheric	P_L	$1 \cdot 10^5$	Pa	-
Diameter riser	D_r	1.955	m	Li et al. (2019)
Diameter downcomer	D_d	1.03	m	Li et al. (2019)
Dilution rate	D_{il}	0.001	1/s	assumed
Surface area downcomer/riser ratio	A_d/A_r	0.29	m	Li et al. (2017)
Length inflow riser	L_{ir}	0.04	m	assumed
Length riser	L_r	10	m	Li et al. (2019)
Length downcomer	L_d	10	m	assumed
Length outflow riser	L_{or}	0.04	m	assumed
Mass transfer liquid				
Solute radius	R_0	$1.208 \cdot 10^{-10}$	m	Cussler (2009)
Diffusion coefficient CO	$D_{if,co}$	$2.717 \cdot 10^{-9}$	m^2/s	see Appendix B
Henry constant CO	H_{co}	$0.7595 \cdot 10^{-5}$	$mol/m^3/Pa$	see Appendix B
Reaction liquid				
CO inhibition constant	$K_{I,co}$	0.5101	mol/m^3	Mohammadi et al. (2014)
CO Monod constant	$K_{s,co}$	0.0178	mol/m^3	Mohammadi et al. (2014)
Ethanol inhibition constant	$K_{I,et}$	217	mol/m^3	Puiman (2020)
Maintenance coefficient CO	$m_{s,co}$	$1.839 \cdot 10^{-5}$	mol/mol X/s	Puiman (2020)
Maximum CO uptake rate	q_{max}	$2.348 \cdot 10^{-4}$	mol/mol X/s	Mohammadi et al. (2014)
Stoichiometric coeff. catabolism	Y_{CO}^{cat}	6	mol/mol EtOH	see Appendix C
Stoichiometric coeff. catabolism	$Y_{CO_2}^{cat}$	4	mol/mol EtOH	see Appendix C
Stoichiometric coeff. catabolism	Y_{Et}^{cat}	1	mol/mol EtOH	see Appendix C
Stoichiometric coeff. metabolism	Y_{CO}^{met}	46.06	mol/mol X	see Appendix C
Stoichiometric coeff. metabolism	$Y_{CO_2}^{met}$	30.407	mol/mol X	see Appendix C
Stoichiometric coeff. metabolism	Y_{Et}^{met}	7.327	mol/mol X	see Appendix C
Stoichiometric coeff. metabolism	Y_X^{met}	1	mol/mol X	see Appendix C

Table 2.3: Continuation of table 2.3. Parameters used to model ELGLR. The parameters calculated for the model are described in the appendices

	Symbol	**Value**	**Unit**	**Reference**
Gas phase				
Molar fraction inlet CO	y_{CO}	0.5	-	assumed
Molar fraction inlet N_2	y_{N_2}	0.5	-	assumed
Gas mass inflow rate	m_{in}	0.5	kg/s	assumed
Superficial inlet velocity	$u_{G,in}$	0.077	m/s	see Appendix B
Bubble rise velocity	v_b	0.25	m/s	see Appendix B
Initial bubble diameter	d_{b0}	0.003	m	Li et al. (2019)
Dispersion coefficient	D_G	$1{\cdot}10^{-9}$	m^2/s	assumed
Molar mass CO	MW_{CO}	28	g/mol	-
Molar mass N_2	MW_{N_2}	28	g/mol	-
Liquid phase				
Density liquid	ρ_L	1000	kg/m^3	Janssen and Warmoeskerken (1987)
Dynamic viscosity liquid	η_L	$6.922 \cdot 10^{-4}$	Pa s	Janssen and Warmoeskerken (1987)
Inlet biomass concentration	$C_{L,X,0}$	25	g/L	Abrahamson (2019)
Molar weight ethanol	MW_{et}	46	g/mol	-
Molar weight biomass	MW_X	24.6	g/mol	-
Dispersion coefficient inflow riser	D_{Lir}	$1{\cdot}10^{6}$	m^2/s	assumed
Dispersion coefficient outflow riser	D_{Lor}	$1{\cdot}10^{6}$	m^2/s	assumed
Dispersion coefficient downcomer	D_{Lor}	$1{\cdot}10^{-16}$	m^2/s	assumed

Table 2.4: Geometries of reactors proposed in literature used for validation

	Young et al. (1991)	Vial et al. (2002)	Abrahamson (2019)	LanzaTech
Length (m)	1.65	6	30	30
Length downcomer (m)	1.65	6	26.5	26.5
Diameter riser (m)	0.19	0.15	4.5	4.5
Diameter downcomer (m)	0.14	0.09	3	3

Chapter 3

Results

In this section the 1D ELGLR model is validated by means of the hydrodynamic and syngas fermentation parameters. The experimental data on the hydrodynamics of an ELGLR from Young et al. (1991)), Vial et al. (2002) and Abrahamson (2019) are used. The hydrodynamic parameters found relevant are the: superficial gas velocity (u_{G_r}), gas hold-up (ε_{G_r}) and superficial liquid velocity in the riser and downcomer (u_{L_r} and u_{L_d}) (Jones, 2007). Subsequently, the parameters: CO mass transfer rate ($R_{tr,co}$), CO uptake rate($q_{r,co}$)and dissolved CO concentration ($C_{Lr,co}$) that influence the syngas fermentation are compared to data from the CFD model of Abrahamson (2019). Lastly, the 1D model is optimized in terms of ethanol productivity (mol/m^3/s) and CO-to-ethanol conversion yield by adjusting the external variable parameters: dilution rate (D_{il}), gas mass inflow rate (m_{in}) and the inlet biomass concentration ($C_{Lir,X0}$). Additionally the obtained productivity and yield are compared to the productivity and yield (%) estimated for the LanzaTech industrial process.

3.1 Hydrodynamic parameter validation

3.1.1 Young

Young et al. (1991) studied the local gas velocity, liquid velocity and gas hold-up in a pilot-scale ELGLR of a two phase flow, air and water. The dimensions of the pilot scale reactor are 1.65 meter in height for riser and downcomer, a riser diameter of 0.19 meter, a downcomer diameter of 0.14 meter and a liquid working volume of 160 L (fig.3.1) (Young et al., 1991).

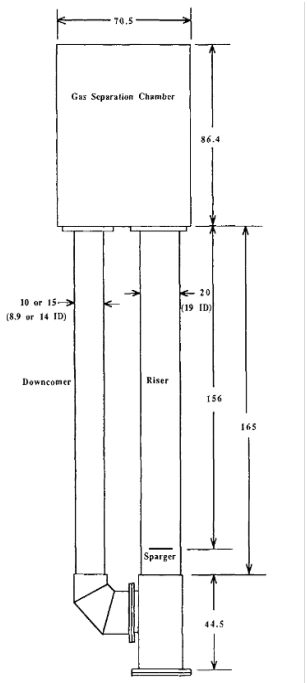

Figure 3.1: Experimental set-up of pilot scale external loop gaslift reactor used by Young et al. (1991)

In the riser two measuring points were present: one at 0.72 meter above the sparger and 1.32 meter above the sparger, the upper en lower ports, respectively. For the comparison only the upper port was considered, since this point is at a larger distance from the sparger, so the hydrodynamic parameters measured at this position are less influenced by the gas sparger. The measuring point of the downcomer was in the middle of the downcomer at 0.66 meter. In addition, the liquid in the downcomer is suggested to be completely free of gas.
Young et al. (1991) examined the hydrodynamic parameters locally at four different inlet superficial gas velocities, 0.96, 2.1, 4.2 and 8.2 cm/s, respectively. The experimentally obtained parameters at the different inlet superficial gas velocities were compared with the 1D external loop gaslift model, that was solved for each of the different inlet superficial gas velocities.

Results and Discussion

The superficial gas velocity in the riser was expected to increase by increasing inlet superficial gas velocity. By sparging more gas in the riser, more bubbles are sparged in and thus a higher superficial gas velocity is achieved. This trend was confirmed by both the 1D model and the experimental data of Young et al. (1991) (fig. 3.2a). The u_{G_r} was accurately predicted by the 1D model at inlet gas velocities of 0.96 cm/s, 2.1 cm/s and 4.7 cm/s. A larger discrepancy between the model and the experimental value was observed at 8.2 cm/s (fig. 3.2a). The superficial gas velocity in the 1D model is predicted by a differential equation over the riser length, that increases through the pressure drop that is caused by a decrease in hydrostatic pressure. In an experimental setting the superficial gas velocity is not only influenced by the hydrostatic pressure, also the reactor geometry, sparger design, bubble dynamics and liquid properties are factors that influence the superficial gas velocity (Heijnen and van 't Riet, 1984). Young et al. (1991) reported that the bubble diameters in the pilot scale gaslift reactor were in the range of 4-6 mm, whereas the bubble diameter in the 1D gaslift ranged from 3-3.8 mm over the length of the riser. The bubble diameter in the 1D external loop gaslift reactor is described to mainly increase over the length of the riser due to the decrease of hydrostatic pressure and decrease little due to the gas molar flowrate. The little deviation between the two bubble diameters, is a possible explanation for the difference in gas velocities at the higher inlet gas velocities since large bubbles tend to rise faster in liquid than small bubbles (Shah et al., 1982). The deviation between the superficial gas velocities of Young et al. (1991) and the 1D

model is small at lower inlet superficial gas velocities, therefore the aforementioned explanations for the deviations may both affect the superficial gas velocity, which elucidate the differences between the 1D model and the experimental data obtained by Young et al. (1991).
The superficial liquid velocity in the riser was predicted considerably accurate by the 1D ELGLR compared to the experimental data obtained by Young et al. (1991)(fig. 3.2b). The superficial liquid velocities of the experimental data and the predictions of the 1D gaslift model both increased with increasing inlet superficial gas velocity. A higher inlet superficial gas velocity increases the amount of gas in the riser, which results in a higher hold-up. A higher hold-up in a gaslift reactor results in more density difference between the riser and downcomer, this imposes a higher liquid recirculation velocity and thus a higher superficial liquid velocity in the riser (Merchuk and Garcia Camacho, 2010). Moreover, at higher inlet superficial gas velocities larger discrepancies are observed between the the predictions of the 1D model and the experimental data. The larger increase of the superficial liquid velocity observed from the experimental data is likely to be caused by the reactor geometry. In view of the experimental set-up of the ELGLR by Young et al. (1991), the two connecting parts between the riser and downcomer are likely to have different friction coefficients (K_B). For instance, an angular shape of a connecting part results in an increase of the friction coefficient (Chisti et al., 1988). The lower part is presumably contributing more to the friction losses, since the liquid is more constricted, whereas the flow that enters the gas separator is much less constricted. The correlation applied in the 1D model considers the friction coefficients of the two connecting parts equal. Therefore, the friction coefficient is highly dependent on the reactor geometry and considered as a significant parameter for the prediction of the superficial liquid velocity in the riser. Although, the superficial liquid velocity in the riser was predicted in the same order of magnitude as the experimental data obtained by Young et al. (1991), the friction coefficient used in the 1D gaslift model was probably not accurate for the reactor geometry used by Young et al. (1991) resulting in more deviation between the experimental and predicted superficial liquid velocities. To examine the influence of K_B on u_{L_r}, an analysis with different values for K_B was performed (Appendix D). The superficial liquid velocities in the riser are higher and more influenced by the coefficient at low friction coefficients (K_B <5). At higher friction coefficients ($K_B \geq 5$) the superficial liquid velocity is less influenced by K_B. Next to this, at higher inlet superficial gas velocities, the superficial liquid velocity is more influenced by the friction coefficients (Appendix D). This effect is observed between the liquid velocities of the 1D model and the experimental data, where deviation between the experimental data and the 1D model at lower inlet gas velocities is smaller than at higher inlet gas velocities. Therefore, the deviation between the experimental data and the 1D model can be partially explained by the assumption of the K_B in the model which is likely to differ from the reactor geometry proposed by Young et al. (1991). The equation to describe the superficial liquid velocity, was validated with experimental data within a range of $\pm$ 30% (Chisti et al., 1988). Therefore the deviation between the experimental data and the 1D model are likely to be caused by the range of validity of the equation proposed by Chisti et al. (1988) and the influence of the friction coefficient.

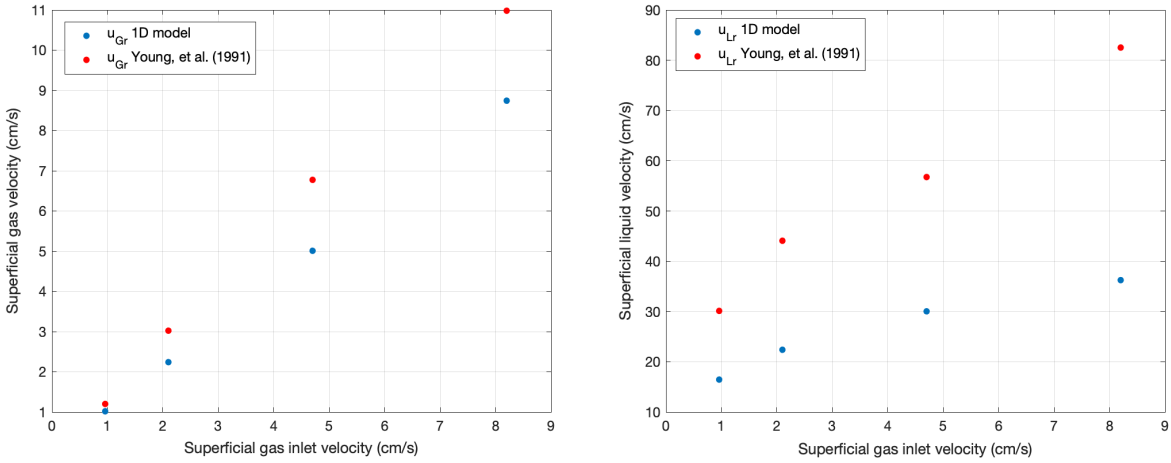

(a) **(b)**

Figure 3.2: Superficial velocities in the riser of 1D model and Young et al. (1991). **a)** gas and **b)** liquid at superficial inlet gas velocities of 0.96, 2.1, 4.7 and 8.2 cm/s, respectively. The blue dots indicate the predictions made by the 1D model and the red dots indicate the experimental data of Young et al. (1991).

Furthermore, the gas hold-up in the riser and the superficial liquid velocity in the downcomer predicted by the 1D gaslift model were compared. The gas hold up and superficial liquid velocity in the downcomer agree well with the experimental data (fig. 3.3a, 3.3b). The gas hold up at the superficial inlet gas velocity of 0.96 cm/s is very accurately predicted by the model. Nevertheless, the gas hold up predicted by the model deviates more at higher gas velocities, yet within the same order of magnitude. The deviations of the gas hold-up between the 1D model and the experimental data obtained by Young et al. (1991) increase, when the inlet superficial gas velocity is increased. The same trend is observed with the superficial gas velocity. The gas hold-up and superficial gas velocity are interrelated, higher superficial gas velocities cause an increase in gas hold-up, since more gas is sparged into the reactor (Jones, 2007). Therefore, the deviation between the superficial gas velocity of the 1D model and the experimental data of Young et al. (1991), might translate to the deviations that are present in gas hold-up values. Since the deviations of the superficial gas velocity and the gas hold-up are not exactly equal, other reasons for the deviation are discussed. The gas hold up in the model is predicted according to the correlation proposed by Hills (1976). This correlation only considers the superficial gas and liquid velocities in the riser and is only applicable in a certain range of gas and liquid velocities, hence for certain flow regimes. The flow regime for which the correlation was established might differ from the flow regime observed by Young et al. (1991). Since for the experimental conditions of Young et al. (1991) different flow regimes are expected, it is hypothesized that this difference resulted in the deviation between the predicted and experimental gas hold-ups.

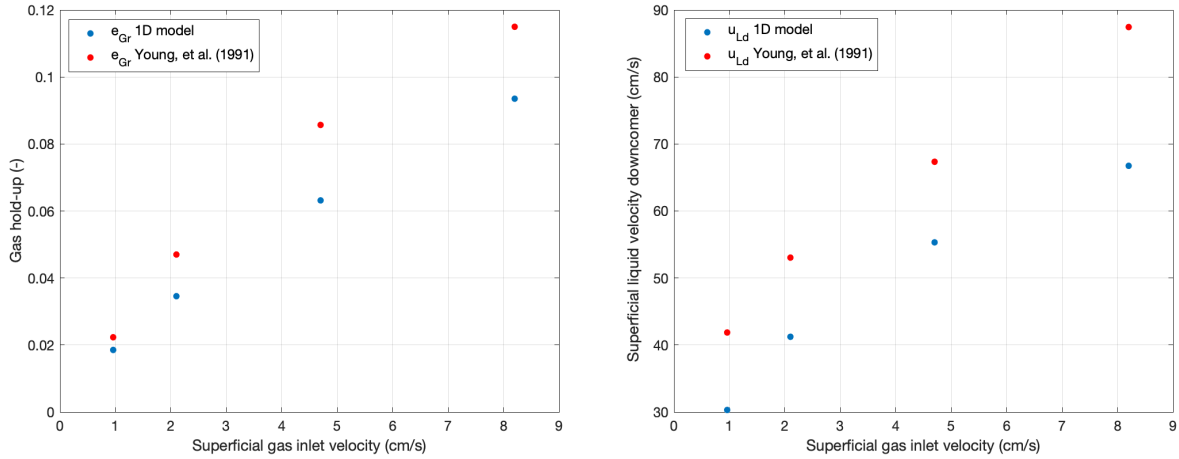

(a) **(b)**

Figure 3.3: Gas hold-up in riser and superficial velocity in downcomer of 1D model and Young et al. (1991). **a)** gas hold-up and **b)** superficial liquid velocity downcomer at superficial inlet gas velocities of 0.96, 2.1, 4.7 and 8.2 cm/s, respectively. The blue dots indicate the predictions made by the 1D model and the red dots indicate the experimental data of Young et al. (1991).

Lastly, the predictions of the superficial liquid velocity in the downcomer in the model agreed with the experimental data, only small deviations were observed (fig. 3.3b). The 1D model predicted lower superficial liquid velocities in the downcomer with the same trend that is observed with the superficial liquid velocity in the riser. The velocity in the downcomer is predicted with the superficial liquid velocity in the riser and corrected with the downcomer-to-riser ratio. As previously mentioned, the superficial liquid velocity in the riser is underpredicted by the 1D model, thus the prediction of the superficial liquid velocity in the downcomer is underpredicted too. Still, the deviation between the experimental data of Young et al. (1991) and the 1D model is smaller than the deviation observed with the superficial liquid velocity in the riser. Since, the liquid velocity in the downcomer is described by the liquid velocity in the riser it is likely that the deviation between the velocities in the riser translated to the deviations between the velocities in the downcomer.

3.1.2 Vial

Vial et al. (2002) examined and compared the local and global phenomena of an external gaslift reactor by measuring the local and global hydrodynamic parameters (ε_{G_r}, u_{L_r} and u_{L_d}) in an experimental set-up of an external loop gaslift reactor. The experimental set-up gaslift reactor of Vial et al. (2002) includes a 6 meter riser and downcomer with a diameter of 15 cm and 9 cm, respectively (fig. 3.4). In the riser two measuring points are located at 2.1 meter distance from another and minimal 1 meter away from the disengagement zone and gas sparger to reduce possible effects of these reactor parts on the hydrodynamic parameters (Vial et al., 2002). The position of the measuring point in the downcomer was not presented. The height of the liquid in the disengagement zone was chosen high enough to completely deaerate the liquid flowing into the downcomer. The global parameters, superficial liquid velocity in the riser and downcomer (u_{L_r}, u_{L_d}) and gas hold-up in the riser (ε_{G_r}) were measured at different superficial gas velocities. The global hydrodynamic parameters were compared with the hydrodynamic parameters predicted by the 1D ELGLR model.

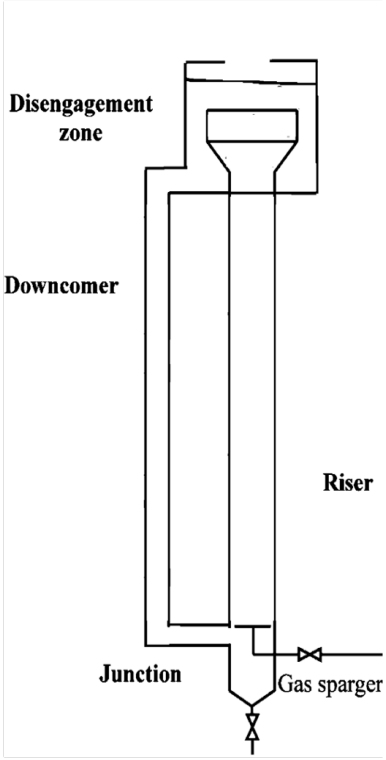

Figure 3.4: Experimental set-up of external loop gaslift reactor used by Vial et al. (2002)

Results and Discussion

The superficial liquid velocities of the 1D model and the experimental data both increase at higher superficial gas velocities. (fig. 3.5a). Similarly to the trend in the comparison with Young et al. (1991), the superficial liquid velocities are expected to increase with increasing superficial gas velocities. At higher superficial gas velocities more bubble are sparged in. The superficial liquid velocities are predicted higher by the 1D gaslift model compared to the experimental data. A large discrepancy between the model and the experimental data is observed at 11.7 cm/s compared to the other superficial gas velocities. The larger discrepancy is assumed to be imposed by increasing friction at larger superficial liquid velocities. The superficial liquid velocity predicted in the 1D model is dependent on the reactor geometry and the gas hold-up. Since, the gas hold-up from experimental data is higher than gas hold-up predicted with the 1D model, the gas hold-up is not likely to cause the discrepancy. The influence of the reactor dimensions is another possible explanation for the discrepancy. Yet, the reactor geometry of Vial et al. (2002) was implemented in the 1D ELGLR model when solved for the hydrodynamic parameters. Therefore, the influence of the reactor dimensions is not likely. Similarly to the comparison with Young et al. (1991), the friction coefficient (K_B) used in the correlation to predict the superficial liquid velocity could have caused the discrepancy.
An incorrect estimation of the friction coefficient might induced the discrepancies between the superficial liquid velocity predicted by the model and the experimental data. To verify the influence of the friction coefficient on the superficial liquid velocity, a sensitivity analysis was performed. The u_{L_r} was predicted for different K_B values at a superficial gas velocity of 11.7 and 6.6 cm/s (Appendix D). The performed analysis shows that small variation of the K_B results in small variations in u_{L_r} (Appendix D). Therefore, the little deviations between the experimental and predicted u_{L_r} at superficial gas velocities from 2.1 - 6.6 cm/s can be explained. The larger deviation of u_{L_r} at u_{G_r} of 11.7 cm/s is not explained.
In addition, K_B is unlikely to be the cause for the deviation since the discrepancy at a superficial gas velocity of 11.7 cm/s is different from the other discrepancies observed at lower superficial gas velocities. It is speculated that the discrepancy possibly is a result of either additional friction that is encountered in an actual ELGLR or possibly a measurement error that was encountered by Vial et al. (2002). Since, measurement errors where not presented by Vial et al. (2002).
In the 1D gaslift model the superficial liquid velocity in the downcomer is dependent on the superficial

liquid velocity in the riser, therefore the discrepancies observed with the superficial liquid velocities in the riser are translated to the downcomer (fig. 3.5b). The discrepancies between the experimental and predicted superficial liquid velocities in the downcomer follow a similar trend as the discrepancies in the superficial liquid velocities in the riser. Consequently, it is very likely that the elucidation of the discrepancies in the riser, also translated to the discrepancies in the downcomer.

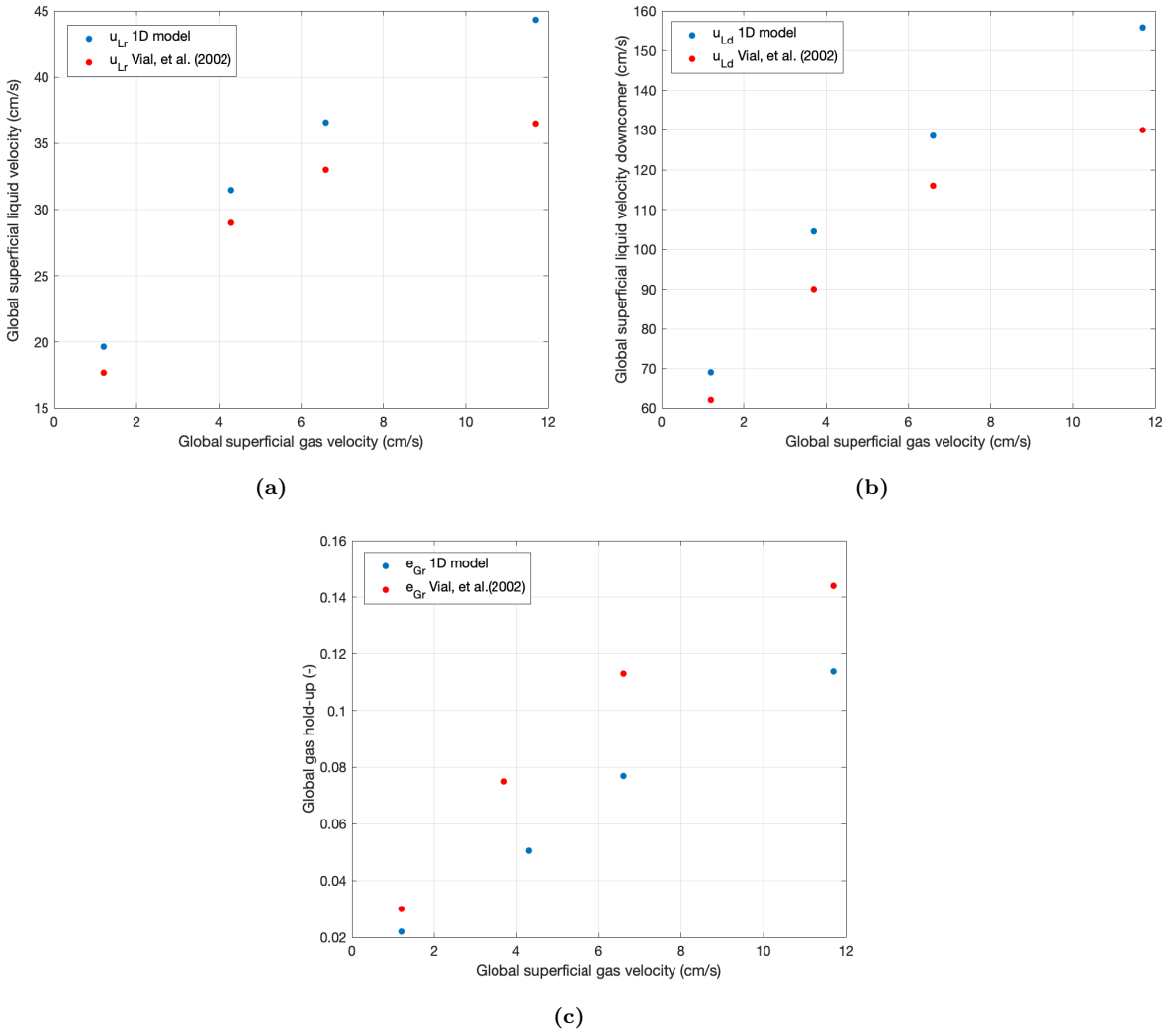

Figure 3.5: Hydrodynamic parameters of 1D model and Young et al. (1991). **a)** superficial liquid velocity, **b)** superficial liquid velocity downcomer **c)** gas hold-up at superficial inlet gas velocities of 1.2, 3.7 and 4.3 for the superficial liquid velocity, 6.6 and 8.2 cm/s, respectively. The blue dots indicate the predictions made by the 1D model and the red dots indicate the experimental data of Vial et al. (2002).

In contrast to the superficial liquid velocities predicted, the global gas hold-ups in the riser, predicted by the 1D model were lower compared to the experimental data (fig. 3.5c). Still, the gas hold-up in the 1D model increased with increasing inlet superficial gas velocities, as well as the gas hold-up from the experimental data. The gas hold-up at 1.2 cm/s was quite accurately predicted by the 1D model, yet an increase in inlet superficial gas velocity caused larger deviations between the 1D model and the experimental data. Vial et al. (2002) presented a comparison between the experimental data and the their CFD model. The global gas hold-up was accurately predicted by the CFD model at low superficial gas velocities, however at increasing superficial gas velocities the deviation between the experimental data and their model increased. Vial et al. (2002) attributed the deviation to the estimation of the turbulence parameters included in the CFD model. A similar trend of deviation is observed when comparing the gas hold-up from experimental data to the 1D model. Therefore, it is hypothesized that more turbulence

occurred at higher inlet gas velocities in the experimental reactor of Vial et al. (2002), which leads to more deviation between the experimental data and the predicted gas hold-up by the 1D model. Since the 1D model did not consider turbulence.

3.1.3 CFD model Abrahamson (2019)

Abrahamson (2019) developed a CFD model to simulate the industrial syngas fermentation process by LanzaTech. The hydrodynamic parameters: superficial gas and liquid velocity and gas hold-up in the riser and the superficial liquid velocity in the downcomer predicted by the CFD model from Abrahamson (2019) were compared to the parameters predicted by the 1D gaslift model. The reactor geometry used for the LanzaTech process consisted of a riser of 30 meter height with a diameter of 4.5 meter, additionally the broadening of the riser at the top was not considered. The downcomer was 26.4 meter in height with a width of 3 meter (Abrahamson, 2019).

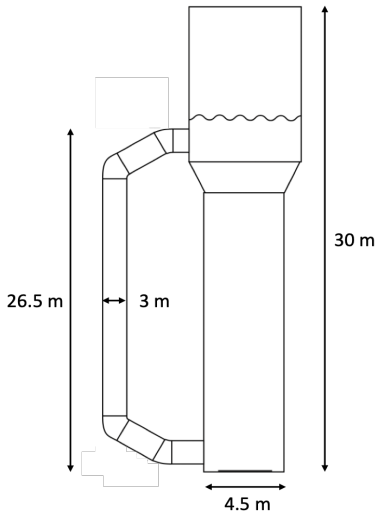

.

Figure 3.6: External loop gaslift reactor geometry proposed and used by Abrahamson (2019)

Results and discussion

The superficial gas velocity predicted by the 1D model corresponds to the gas velocity predicted by the CFD up to 21 meter in the riser (fig. 3.7a). After 25 meters the headspace of the ELGLR in the CFD is reached, where almost no liquid is present, thus the superficial gas velocity is expected to decrease. A headspace was not considered in the 1D model, therefore the superficial gas velocities after 25 meters are not further compared and elucidated. The superficial gas velocity in an ELGLR should increase over the length of the reactor, due to a decrease of hydrostatic pressure and bubble dynamics, such as bubble coalescence. However, no bubble dynamics were considered in the CFD model. The fluctuations in the gas velocity from the CFD are probably caused by the time that was taken for the time-averaging to obtain the hydrodynamic parameters. Performing the time-average of the CFD with too short time presumably results in fluctuations being less well averaged, which is not expected when time-averaging is performed for longer times.
The superficial gas velocity of the 1D model increased over the length of the riser, due to the definition of the u_{G_r} in which the velocity tends to increase due to decreasing hydrostatic pressure.

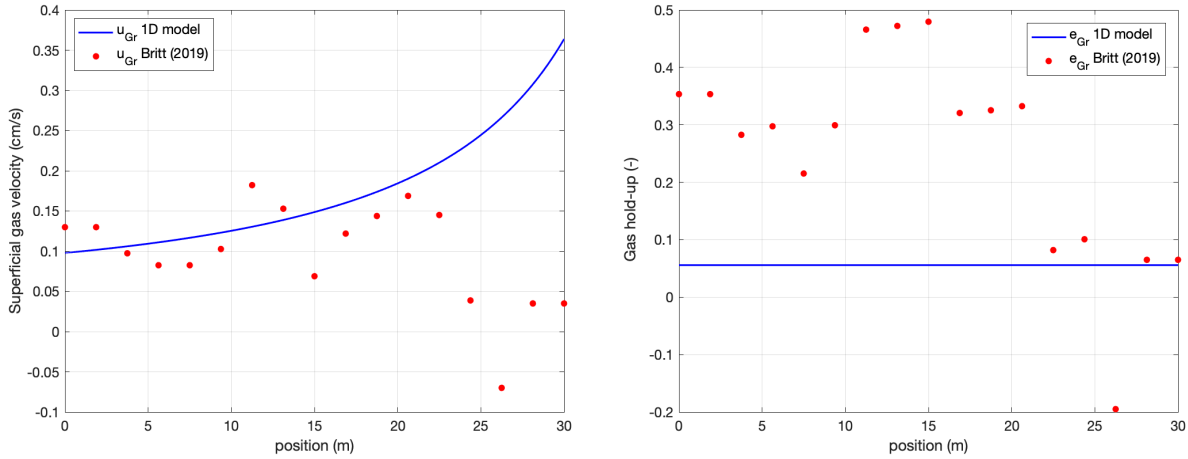

(a) **(b)**

Figure 3.7: Gas superficial velocity and hold-up in riser of 1D model and CFD model by Abrahamson (2019). **a)** superficial gas velocity and **b)** gas hold-up over the length of the riser (m). The blue line indicates the predictions made by the 1D model and the red dots indicate the predictions made by the CFD model of Abrahamson (2019).

Similarly to the superficial gas velocity, the values of the gas hold-up in the headspace of the reactor in the CFD are not compared to the 1D model. The hold-up predicted by the 1D model (0.0557) was significantly lower than the hold-ups predicted by the CFD simulation. Nevertheless, the gas hold-ups predicted by the CFD are considered higher than expected for ELGLRs. The comparison of two models cannot clarify which hold-up is more likely to be an accurate prediction of the gas hold-up in an actual gaslift reactor at large scale. Therefore, the gas hold-up correlation proposed by Bello et al. (1985) was used to examine gas hold-up that is expected in a large scale external gaslift reactor. The correlation proposed by Bello et al. (1985) was used since the correlation was compared to experimental data and other correlations proposed in literature. The correlations used by Bello et al. (1985) included comparison with the correlation proposed by Hills (1976), which is used for the prediction of the gas hold-up in the 1D model.

The predicted hydrodynamic parameters and reactor geometry of the CFD model were implemented in the gas hold-up correlation. The values of the calculated gas hold-up are on average 0.14, with two deviations at 15 and 22.5 meters (fig. 3.8). The deviations are likely to be caused by the time that was used for the time averaging of the CFD simulation, as previously mentioned. The average of the gas hold-up values predicted in the CFD model are 0.20. The CFD model overestimated the gas hold-up with 30 %.
The gas hold-up of 1D model was predicted with the correlation proposed by Bello et al. (1985) as well. The calculated hold-up increased over the length of the riser due to the superficial gas velocity that was used in the correlation proposed by Bello et al. (1985), which is a result of the decrease in hydrostatic pressure. The average of the calculated hold-up (0.065) overstimated the hold-up predicted with the 1D model with 18%. The difference between the calculated hold-ups of the 1D and CFD model can be mainly attributed to the difference in superficial liquid velocity. Since, the calculated gas hold-up of the CFD and 1D model correspond more to the hold-up predicted by the 1D model it is presumed that the hold-up predicted with the CFD model of Abrahamson (2019) was too high.

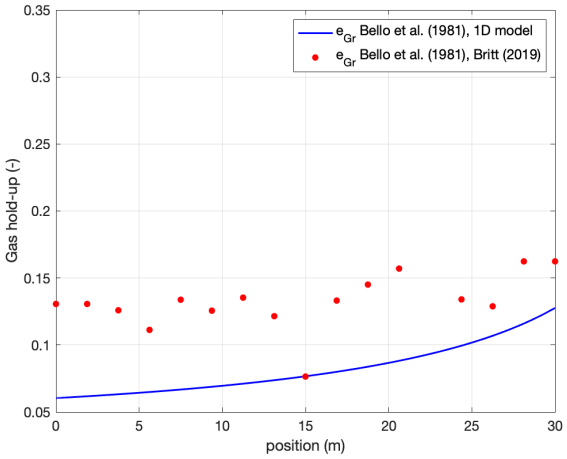

Figure 3.8: Gas hold-up of 1D gaslift model and CFD model of Abrahamson (2019) approached by correlation of Bello et al. (1985)

Furthermore, the superficial liquid velocity predicted by the 1D model was 1.05 m/s, whereas the superficial liquid velocity in the CFD model by Abrahamson (2019) fluctuated from 0.2 m/s to 0.5 m/s. A potential hypothesis for the difference in superficial liquid velocity in the CFD and the 1D model is the gas entrainment in the downcomer which was observed in the CFD simulation. Gas entrainment in the downcomer reduces the density difference between riser and downcomer, which results in a decreasing liquid velocity in the riser. Since the liquid velocity is dependent on the density differences between the riser and downcomer. In the 1D gaslift model no gas was assumed to be entrained in the downcomer, hence the superficial liquid velocity in the 1D gaslift model was estimated higher compared to the CFD model by Abrahamson (2019). Additionally, the expansion of the riser diameter at the top of the riser in the CFD was not included in the 1D model. An increase in the riser diameter decreases the superficial liquid velocity. It is speculated that this difference in geometry contributed to the difference between the superficial liquid velocity from the 1D model and CFD as well.
The superificial velocity in the downcomer predicted by the CFD fluctuates between 1.3 and 1.45 m/s, whereas the 1D model predicted the superficial liquid velocity in the downcomer at 2.32 m/s. Gas entrainment in the downcomer can cause the lower superficial liquid velocity in the downcomer, like it decreases the superficial liquid velocity in the riser.

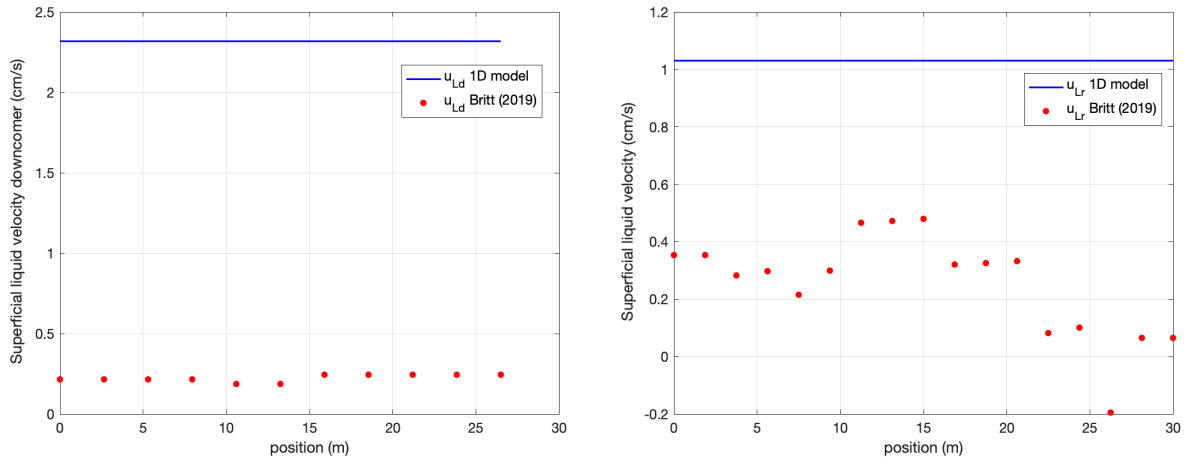

(a) **(b)**

Figure 3.9: Liquid superficial velocity in riser and downcomer of 1D model and CFD model by Abrahamson (2019). **a)** superficial liquid velocity and **b)** superficial liquid velocity in the downcomer over the length of the riser (m). The blue line indicates the predictions made by the 1D model and the red dots indicate the predictions made by the CFD model of Abrahamson (2019).

3.1.4 Conclusion

In conclusion the hydrodynamic parameters, superficial gas velocity (u_{G_r}), gas hold-up (ε_{G_r}) and superficial liquid velocity in the riser and downcomer (u_{L_r} and u_{L_d}), predicted by the 1D model seemed to agree well with the experimental data. The deviations between experimental data and the 1D model were attributed to the correlations, equations and assumptions in the 1D model to describe the hydrodynamic parameters. Still, it is concluded that the 1D model can be used to obtain an approximate prediction of important hydrodynamic parameters in an actual ELGLR.
The hydrodynamic parameters of the CFD model were less well predicted by the 1D model, yet still within the same order of magnitude. The deviations between the CFD model and the 1D model are attributed to the assumptions and correlations that are different for both models, such as the turbulence modelling in the CFD. A comparison between two models cannot elucidate which model more accurately simulates and predicts the hydrodynamic parameters of an industrial ELGLR. Hence experimental validation should elucidate which model more accurately predicts the hydrodynamic parameters in an ELGLR.

3.2 Syngas fermentation parameters

A comparison between the syngas fermentation process of Abrahamson (2019) and the 1D model was performed, since little data is available on syngas fermentation in large scale ELGLR. Abrahamson (2019) attempted to simulate the LanzaTech fermentation process in more detail, therefore the syngas fermentation process of the 1D model was compared to the CFD model.

3.2.1 Abrahamson (2019) syngas comparison CFD simulation

The ethanol productivity and CO-to-ethanol conversion yields are considered to estimate the performance of the syngas fermentation process. Both parameters are dependent on several factors, like the uptake rate of CO by the micro-organism, mass transfer and potential inhibition terms. The ethanol productivity and CO to ethanol conversion yield were not discussed in Abrahamson (2019), yet the mass transfer and CO uptake rates as well as the dissolved CO concentration, are discussed. Therefore, these factors are used to examine the performance of the syngas process in an ELGLR. To asses whether these factors agree between the 1D model and the CFD simulation, the mass transfer and CO uptake rates and CO concentration profiles over the length of the riser are compared.

Results and Discussion

The comparison between both models showed that the dissolved CO concentration predicted by the 1D model was lower than the concentration from the CFD simulation. In both models the amount of dissolved CO concentration is a resultant of the difference between the mass transfer rate and the CO uptake rate. The mass transfer that was predicted by the CFD simulation of Abrahamson (2019) decreased over the length of the riser. At a height of 25 meters the headspace is of the reactor is reached resulting in a decrease in mass transfer. The headspace was not included in the 1D model, therefore the headspace is not included in the comparison. The mass transfer rates predicted by the 1D model are lower than the values predicted with the CFD simulation. Moreover, the mass transfer rates of the 1D model gradually decrease over the length of the riser. The difference between the 1D model and the CFD model could be caused by the different mass transfer coefficient (k_L) equation that is used in the CFD model. The mass transfer coefficient predicted with the 1D model was higher ($5{\cdot}10^{-4}$ m/s) compared to the k_L of the CFD ($3.5{\cdot}10^{-4}$ m/s). A high k_L should increase the mass transfer, therefore the difference between the mass transfer rates cannot be explained by this. Yet, the high hold-up observed in the CFD simulation was approximately 0.35 which is roughly 5 times higher than the hold-up predicted in the 1D model, which was 0.07 (fig. 3.7b). The difference in hold-up between both models is likely to be the cause for the higher mass transfer rates. Additionally the bubble size was examined since, the mass transfer rate is dependent on the bubble size distribution in the reactor (Merchuk and Garcia Camacho, 2010). Smaller bubbles have a larger gas-liquid surface area which increases the mass transfer. However, Abrahamson (2019) assumed a constant bubble diameter of 7 mm. The large bubbles are potentially the cause for the high gas hold-up. In contrast, the bubble diameter in the 1D model was described to increase over the length of the riser due to a decrease in hydrostatic pressure and an increase of superficial gas velocity. The bubble diameter increased from 3 mm to approximately 3.8 mm. Therefore, higher mass transfer rates are expected in the 1D gaslift model. To analyse the influence of the two different bubble diameters, the mass transfer rate in the riser of the 1D model was calculated at a bubble diameter of 3 and 7 mm, respectively (Appendix D). A higher mass transfer rate at lower bubble diameter was confirmed by the analysis. Consequently, it is presumable that the difference between the mass transfer rates is caused by the difference in hold-up between both models, this could also explain the difference between the dissolved CO concentration and CO uptake rate in both models.

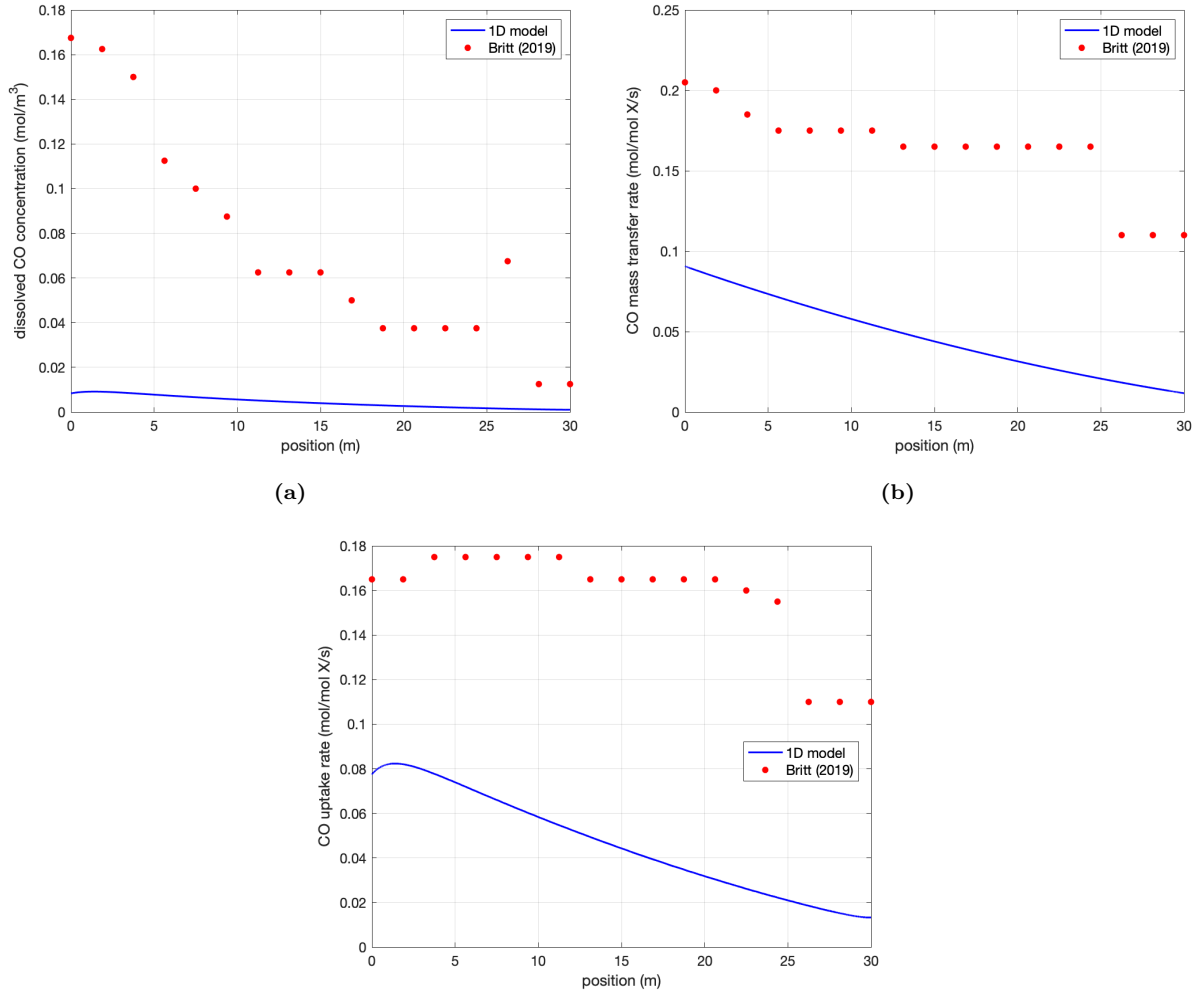

c) CO uptake rate over the length of the riser (m). The blue line indicates the predictions made by the 1D model and the red dots indicate the predictions made by the CFD model of Abrahamson (2019).

Figure 3.10: a) Dissolved CO concentration **b)** CO mass transfer coefficient

Conclusion

In conclusion, the syngas fermentation parameters predicted with the 1D and CFD model did not correspond. The deviation between the models is likely to be caused by the different estimation of the hydrodynamic parameters, such as the gas hold-up which presumably resulted in higher mass transfer rates in the CFD model. Since the conversion of CO by *C. autoethanogenum* was similar in both models. It was shown that that smaller bubble diameters result in higher mass transfer coefficients. Hence, experimental data on syngas fermentation in an ELGLR is necessary for the validation of syngas fermentation in a 1D ELGLR model.

3.3 Optimization syngas fermentation 1D model

Optimizing syngas fermentation in view of ethanol productivity or titer and CO-to-ethanol conversion yield is important, especially for industrial purposes (Liew et al., 2016). By maintaining the mass transfer rate equal to the CO reaction rate, the dissolved CO concentration is kept constant and thus less inhibition of CO occurs. This results in higher CO uptake rates, which determine the CO reaction rate. To obtain high mass transfer and CO uptake rates, external variable parameters of an actual ELGLR were identified and varied in the 1D model: dilution rate (D_{il}), biomass concentration (C_X) and gas mass inflow rate (m_{in}). Firstly, the dilution rate was varied to obtain the most optimal mass transfer rate of CO and the CO uptake rate, after that the ethanol productivity was examined. The dilution rate was varied between 0 and 0.0001 1/s since the dilution rate estimated for the industrial LanzaTech plant was roughly $1{\cdot}10^{-5}$ 1/s (Appendix G). Similarly, the gas mass inflow rate was estimated to be 2.11 kg/s (Appendix G) and kept constant at all dilution rates, as well as the biomass inlet concentration (25 g/L). The observed CO uptake rate was low at low dilution rates due to the high ethanol concentration which causes inhibition (fig. 3.11a). To understand the cause for the high ethanol concentration, the ethanol production rate in time was examined (fig. 3.11b). Due to a high ethanol production rate initially, the ethanol concentration increased leading to inhibition of CO uptake in time (fig. 3.11a, 3.11b). As a consequence of the low CO uptake rate, the difference between mass transfer rate and CO reaction rate in the riser increases which results in high dissolved CO concentrations which causes more inhibition on the CO uptake rate (fig. 3.12a, 3.12b). Therefore, too low dilution rates are not considered advantageous.

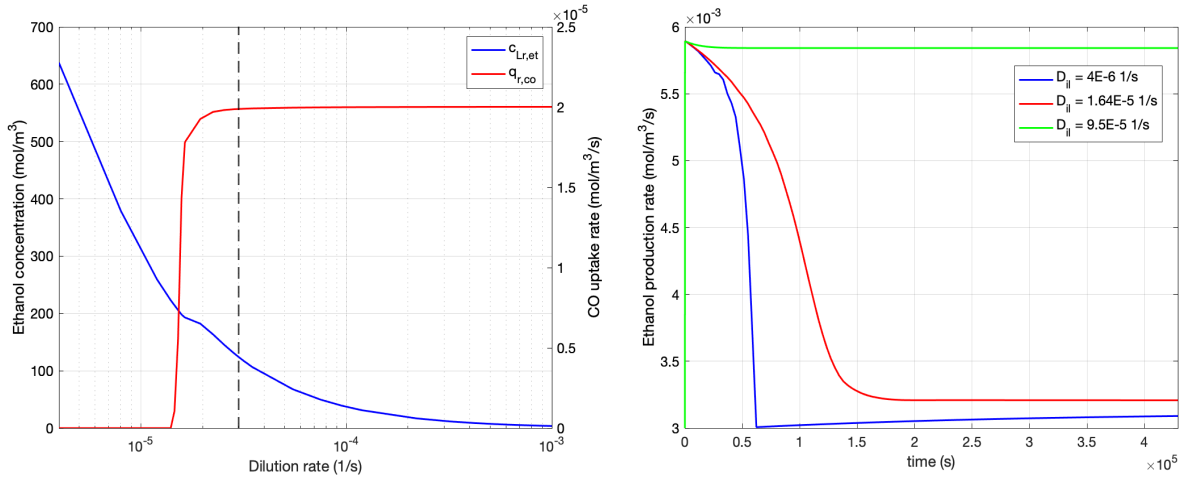

(a) **(b)**

Figure 3.11: a) CO uptake rate (mol/mol X/s) and ethanol concentration (mol/m^3) at a dilution rate range of 0-10^{-3} (1/s) on a logaritmic scale at the time point, t = $4.32{\cdot}10^5$ s. Both the CO uptake rate and ethanol concentration are averaged over the length of the riser. The red line on the right y-axis and blue line on the left y-axis indicate the CO uptake rate and ethanol concentration, respectively. **b)** Ethanol productivity (mol/m^3/s) in time at dilution rates of $4{\cdot}10^{-6}$ (blue line), $1.65{\cdot}10^{-5}$ (red line) and $9.5{\cdot}10^{-5}$ (green line) 1/s, respectively. The ethanol production rate is an average over the length of the riser.

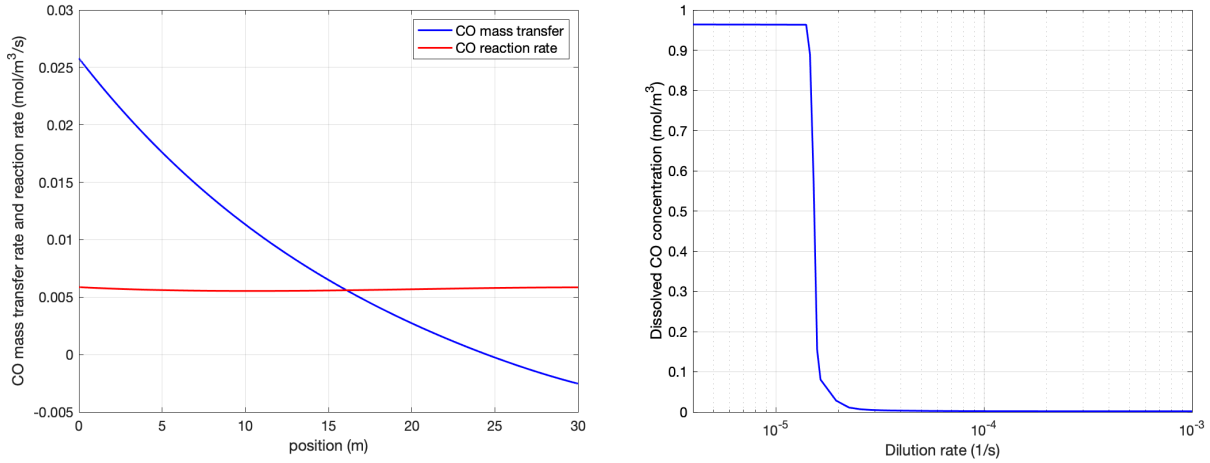

(a) **(b)**

Figure 3.12: a) Mass transfer rate (blue line) and CO reaction rate (red line) (mol/mol X/s) over the length of the riser at dilution rate (D_{il}) $1.59{\cdot}10^{-5}$ 1/s at the time point, t = $4.32{\cdot}10^{5}$ s. **b)** Dissolved CO concentration in the riser at various dilution rates at the time point, t = $4.32{\cdot}10^{5}$ s. The average of the dissolved CO concentration over the riser was considered.

At higher dilution rates ($D_{il} > 3{\cdot}10^{-5}$ 1/s) the CO uptake rate becomes almost constant (fig. 3.11a) as well as the the mass transfer and CO reaction rate (fig. 3.13). The optimal dilution rate was considered to be $3{\cdot}10^{-5}$ (1/s), since the CO uptake rate and mass transfer rate are the highest. Yet, at higher dilution rates the ethanol concentration becomes low which is considered not advantageous at large scale from an economical point of view. In addition the ethanol productivity is influenced by the dilution rate as well. After $D_{il} > 3{\cdot}10^{-5}$ the ethanol production rate reaches a constant value of 3.95 $\cdot 10^{-3}$ (fig. 3.13a). This is likely to be caused by the definition of the ethanol productivity in the 1D model (Appendix C). The ethanol production is described by its maintenance catabolism ($m_{s,et}$), biomass concentration (C_X) and the biomass specific production rate ($q_{r,et}$) which is dependent on the growth rate and this is dependent on the CO uptake rate (Appendix C). Therefore, when the CO uptake rate becomes almost constant the ethanol productivity reaches an almost constant value (fig. 3.13a). In addition the offset at low dilution rates is caused by the growth rate that is zero. At higher dilution rates the growth rate increases and thus the ethanol production rate increases. The CO uptake rate was observed to be zero at low dilution rates ($D_{il} < 1{\cdot}10^{-5}$) which should result in zero ethanol productivity since no CO is taken up (fig. 3.11a, 3.13a). However, due to the definition of ethanol productivity in the model the ethanol productivity reaches the maintenance rate for the catabolic reaction (Appendix C) instead of zero. To improve the model a conditional statement could be implemented to include the dependency of the ethanol productivity on the CO uptake rate. Hence, the ethanol productivity can be increased if the biomass concentration or growth rate is increased.

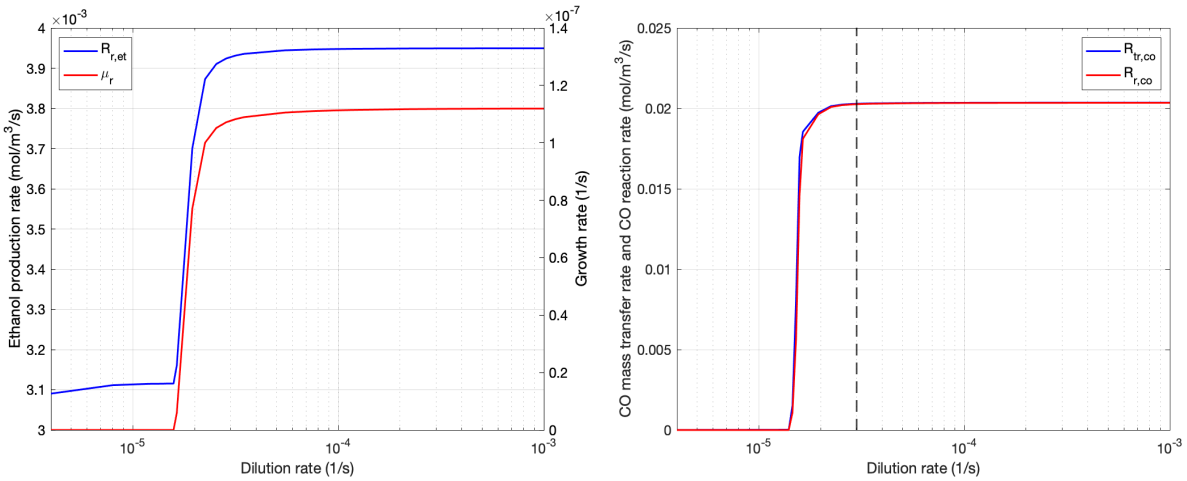

(a) **(b)**

Figure 3.13: **a)** Parametric analysis of D for ethanol production rate and specific growth rate of *C. autoethanogenum*. The blue line indicates the ethanol production rate ($R_{r,et}$) at different dilution rates. The red line indicates the specific growth rate of *C. autoethanogenum* (μ_r) at different dilution rates on the right y-axis. **b)** Mass transfer rate and CO reaction rate in the riser at various dilution rates. The blue and red line on the left and right y-axis indicate the CO mass transfer and CO reaction rate, respectively. The CO mass transfer and reaction rate, growth rate and ethanol production rate are averages over the length of the riser at the last time point t = $4.32{\cdot}10^5$ s.

Next to the dilution rate, the gas mass inflow (m_{in}) can be optimized. The gas inflow rate was varied between 0.1 and 10 kg/s to assure the inclusion of the inlet superficial gas velocities of 1-14 cm/s, since these velocities are considered a realistic range for practical external loop gaslift reactors (Young et al., 1991; Vial et al., 2002; Verlaan et al., 1989). At high gas mass inflow rates more mass transfer is expected due to the high amount of gas that is sparged in. Consequently, it is expected that the CO uptake rate increases which results in an increase of CO reaction rate, assuming that ethanol inhibition has insignificant influence. In contrast, at too high gas inflow rates it is presumed that the CO uptake decreases due to high ethanol concentration which induces inhibition. As a result of low CO uptake rates, the dissolved CO concentration increases. In the range of gas mass inflow rates applied, increasing mass transfer rates were observed, yet a mass flow rate of 6 kg/s and higher resulted in a decrease of the CO reaction rate. The difference between both rates was very small until an inflow rate of 6 kg/s (fig. 3.14a). The dissolved CO concentrations did increase at higher gas flow rates as well as the ethanol concentrations, which increased significantly. The ethanol concentration increased fast until a flow rate of 6 kg/s (fig. 3.14b).

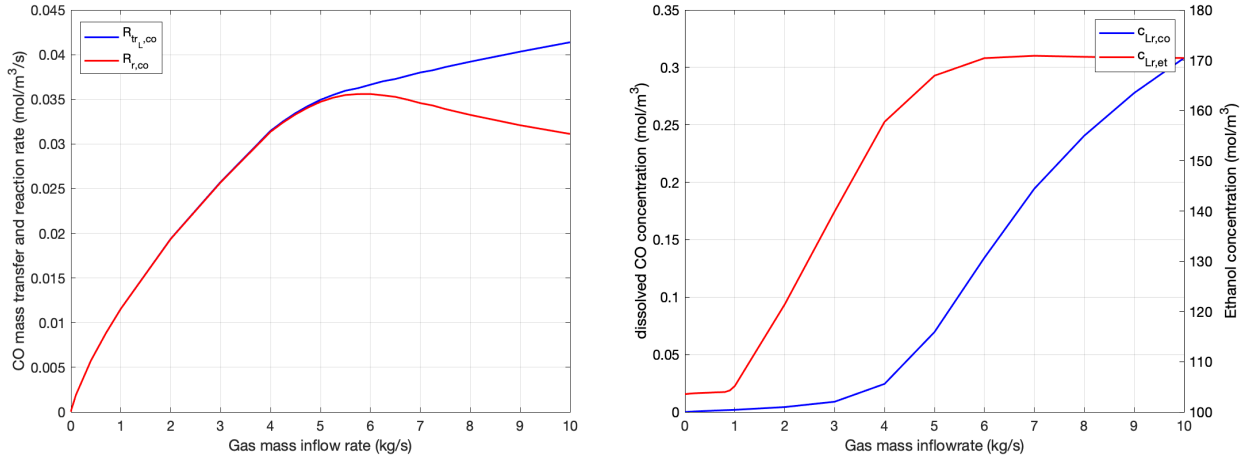

(a) **(b)**

Figure 3.14: a) CO mass transfer and reaction rate and **b)** dissolved CO and ethanol concentrations in the riser (mol/m^3). The blue line indicates the CO concentration and the red line indicates the ethanol. The left y-axis and right y-axis present the dissolved CO and ethanol concentrations, respectively. The CO mass transfer and reaction rate, ethanol and CO concentration are averages over the length of the riser at the last time point t = $4.32{\cdot}10^5$.

Consequently, the high ethanol concentration resulted in much inhibition confirming the significant influence on the CO uptake rate (fig. 3.15a). Based on these results, it is considered that a gas flow rate of more than 6 kg/s is not optimal due to the decreasing CO reaction rate, which is caused by the decrease in CO uptake rate that is inhibited by the high concentrations of ethanol. Similarly, the ethanol productivity increased with increasing gas mass flow rates until a gas inlet flow rate of 6 kg/s (fig. 3.15b). A decrease is observed after this flow rate, due to the CO uptake rate that decreases which results in a decreasing growth rate, hence a decrease of ethanol production rate (fig. 3.15b).

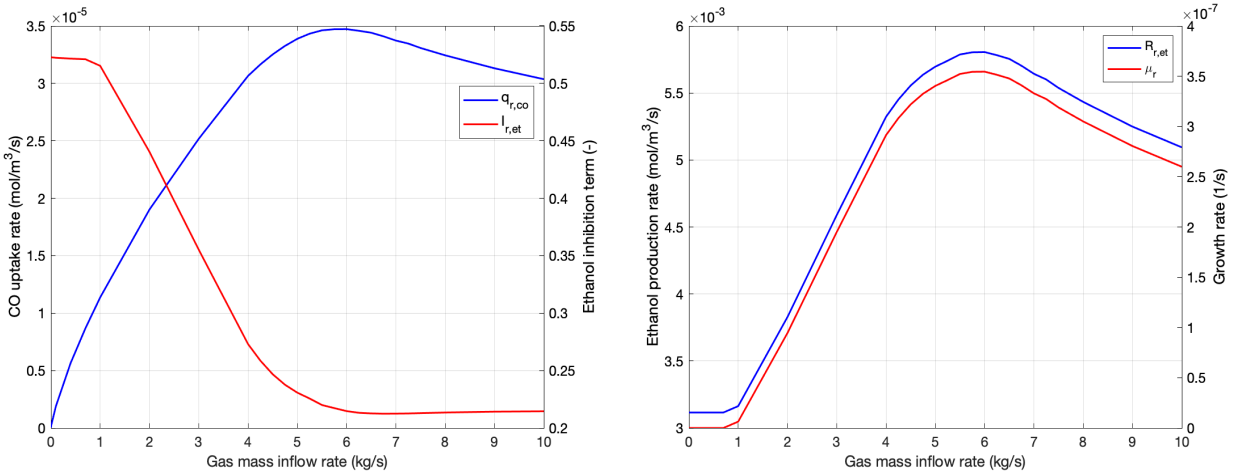

(a) **(b)**

Figure 3.15: a) CO uptake rate and ethanol concentration. With on the left axis the CO uptake rate and on the right axis the ethanol concentration. **b)** Ethanol production rate (mol/mol X/s) (blue line) and growth rate (1/s) (red line) at various gas inflow rates (kg/s). The left and right axis represent the ethanol production rate and growth rate, respectively. The CO uptake rate and ethanol inhibition, production rate and growth rate are averages over the length of the riser at the last time point t = $4.32{\cdot}10^5$ s.

In addition, the CO transferred from the gas phase to the liquid phase was examined to further elucidate a potential optimum. The mass transfer in the gas phase ($R_{tr_G,co}$) increased at higher mass gas mass

inflow rates until 2 kg/s after which it decreased. The decrease was a result of increasing dissolved CO concentrations, reducing the driving force for mass transfer. Consequently a decrease of the mass transfer in the gas phase is observed. Considering this decrease and the increasing ethanol production rate until a gas mass inflow of 6 kg/s, a trade-off analysis between the CO conversion in the gas phase and the ethanol productivity was made (fig. 3.16b). The conversion of CO in the gas phase was formulated as the difference between the gas in and outflow of the riser relative to the gas that flows in (eqn. 3.1).

$$\mathrm{Y}_{CO} = \frac{\mathrm{CO}_{in} - \mathrm{CO}_{out}(\mathrm{mol/s})}{\mathrm{CO}_{in}(\mathrm{mol/s})} = \frac{(J_{in,CO} - J_{out,CO})\, A_r\, e_{Gr}}{J_{in,CO}\, A_r\, e_{Gr}} \cdot 100\% \tag{3.1}$$

At a gas mass inflow rate of 6 kg/s the ethanol productivity is high whereas the conversion of CO is low compared to the amount of CO that flows into the riser. This is considered disadvantageous from an economical perspective. In contrast at lower dilution rates the ethanol production rate decreases, yet the CO conversion increases. Considering all the observations from the parameters mentioned, a range of the optimal gas mass inflow rate is observed between 2 and 3 kg/s. Therefore, the optimum mass transfer rate for the gas phase was established at 2.5 kg/s, hence this value was implemented in the next optimization step.

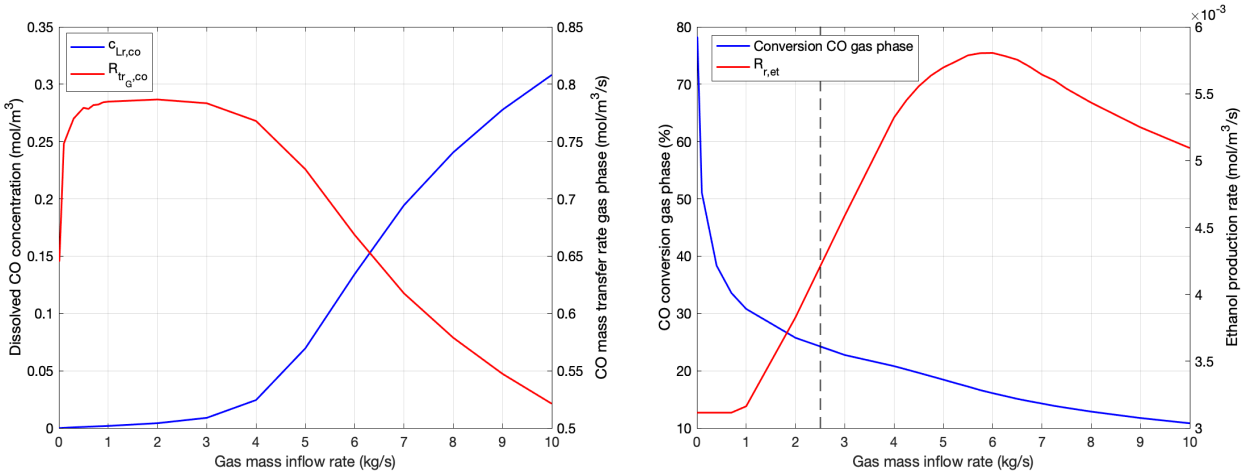

(a) **(b)**

Figure 3.16: a) CO mass transfer rate from gas phase ($R_{tr_G,co}$ (mol/m^3_G/s)) and dissolved CO concentration ($c_{Lr,co}$ (mol/m^3_L/s)) in the liquid at various gas mass inflow rates in the riser. The left y-axis and blue line represents the CO mass transfer and the right y-axis and red line represent the dissolved CO concentration in the liquid. **b)** CO conversion gas phase and ethanol production rates at various gas inflow rates in riser. The blue line and left y-axis represent the CO conversion in the gas phase. The red line and right y-axis indicates the ethanol production rate. The CO mass transfer rate in the gas phase, dissolved CO concentration and ethanol production rate are averages over the length of the riser at the last time point t = 4.32·10^5 s. The in and outflow of gas was also at time point t = 4.32·10^5 s.

The inlet biomass concentration is another external variable parameter that was varied to identify the optimal configuration in the 1D model. For the last analysis, the gas inflow rate of 2.5 kg/s and a dilution rate of 3·10^{-5} 1/s are applied. It is expected that high biomass inlet concentrations affect the reaction rates of CO and ethanol due to the dependence of these rates on the biomass concentration and the growth rate of *C. autoethanogenum*. As a result of the the low growth rate of *C. autoethanogenum* it is expected that the ethanol reaction rate is mainly influenced by the biomass concentrations. The reaction rates of CO and ethanol increased at increasing biomass concentrations, which confirmed the expectations (fig. 3.17a). The increase of ethanol at higher inlet biomass concentrations was more significant than the reasonably small increase of the CO reaction rate. Overall the reaction rates increase at higher biomass inlet concentration due to the definition of these parameters in the model. Additionally, the CO uptake rate and CO concentration were examined to further elucidate a potential optimum. The CO uptake rate increased until a biomass concentration of 3.75 g/L after which the rate decreased. The increase of CO

uptake rate is a resultant of the high dissolved CO concentrations and little ethanol inhibition (fig. 3.17b, 3.17c). Overall the reaction rates increase at higher biomass inlet concentration due to the definition of these parameters in the model, in the range of 10-25 g/L biomass, the CO and ethanol reaction rate increase is small to very small, respectively. Yet, the CO uptake rate decreases as well as the dissolved CO concentration. Considering that high biomass concentrations are not advantageous at industrial scale from an economical point of view, due to high costs for biomass and downstream processing, the optimal biomass inlet concentration is considered to be 10 g/L.

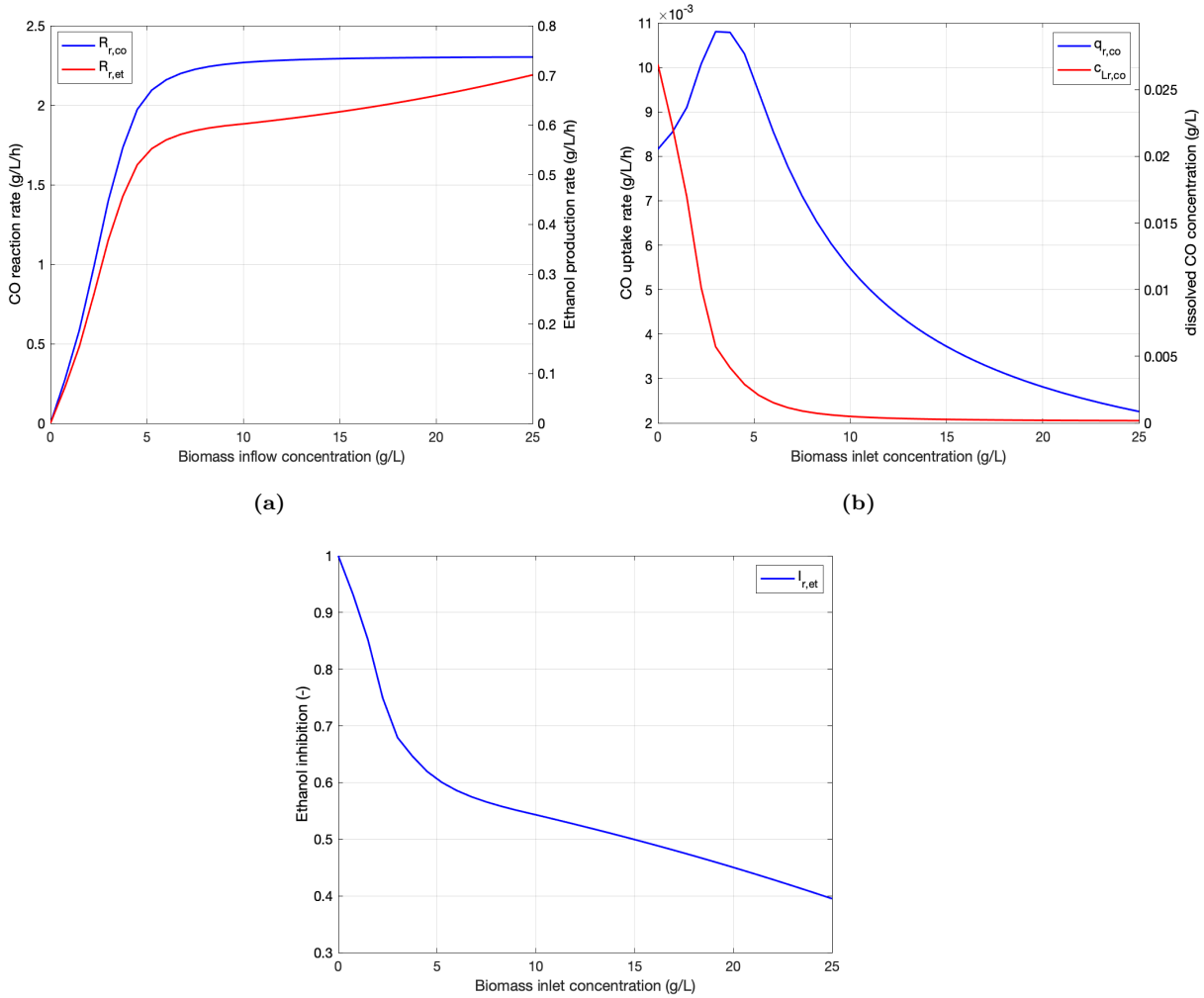

Figure 3.17: a) Ethanol production and CO reaction rate at various biomass inlet concentrations($C_{L_{ir},X,0}$). The blue line indicates the CO reaction rate which is plotted on the left y-axis. The red line indicates the ethanol production rate which is plotted on the right axis. **b)** CO uptake rate and CO concentration at various biomass inlet concentrations ($C_{L_{ir},X,0}$). The blue and red line on the left and right y-axis indicate the CO uptake rate and dissolved CO concentration, respectively. **c)** Ethanol inhibition term at various biomass inlet concentrations ($C_{L_{ir},X,0}$). All rates and concentrations are averages over the length of the riser at time point t = $4.32{\cdot}10^5$ s.

Adjustment of the variable parameters was used to optimize the overall syngas fermentation in the 1D model, resulting in an ethanol productivity and CO-to-ethanol conversion yield of 0.6 g/L/h and 30.4 % at an inlet concentration of 10 g/L, respectively.

The LanzaTech estimations were calculated for an inlet biomass concentration of 5 g/L and the metabolism of *C. autoethanogenum* was approached in a similar way. The ethanol productivity of the model at similar biomass concentrations of LanzaTech was used to compare the ethanol productivity and CO-to-ethanol

conversion yields. The productivity is predicted higher with the LanzaTech approximation. The process of LanzaTech is known to involve an engineered *C. autoethanogenum* which is assumed to have high ethanol tolerance and high CO-to-ethanol conversion yield to make the process commercial feasible. The 1D model predicted the ethanol productivity within the same order of magnitude compared to the LanzaTech approximation and the CO-to-ethanol conversion yield showed similar values (table 3.1). Since the parameters of the LanzaTech process are rough estimations and the optimized 1D model had different input parameters (reactor volume, gas phase included, dilution rate, etc) the difference between the ethanol productivity can be explained. Moreover, the conversion yield was predicted more accurate due to similar description of the metabolism in both calculations. Therefore, for both parameters it cannot be concluded whether the 1D model can describe the LanzaTech process accurately. Hence, more detailed data of the metabolism of *C. autoethanogenum* and the LanzaTech process is necessary to examine the validity of the syngas fermentation predicted by the 1D model.
In the optimization proposed here, the parameters were consecutively optimized which does not consider the influence of the last and second optimized parameter on the first optimized parameter. A trade-off analysis can be performed with the external variable parameters, D_{il}, $C_{X,0}$ and m_{in}, proposed here could derive an optimal condition for ethanol productivity and CO-to-ethanol conversion yields. Another external variable parameter that can be varied is pressure, at higher pressures the saturation concentration of gas in liquid can be increased resulting in higher higher mass transfer rates, hence reducing the mass transfer limitation. This can potentially increase the ethanol productivity since more gas is available to convert to ethanol. The reactor geometry such as length, diameter of riser and downcomer and downcomer-to-riser ratio could also be analysed and further improved with the 1D model. By varying the diameter of the riser, downcomer or downcomer-to-riser ratio the superficial liquid velocity in the reactor changes. This affects the gas hold-up and the mass transfer in the reactor. By optimizing these parameters optimal conditions for mass transfer can be obtained, which is advantageous due to the poor mass transfer in sygnas fermentation. Other parametric analysis of the hydrodynamic parameters can be performed such as, dispersion coefficients and gas velocities and the gas hold-up to examine the influence of these parameters on the CO gradients in the reactor which influence the ethanol productivity throughout the reactor.

Table 3.1: Ethanol productivity, CO-to-ethanol conversion yield and percentage difference for optimized 1D model and LanzaTech process both at an biomass inlet concentration of $C_{Lr,X0} = 5$ g/L.

	Ethanol productivity (g/L/h)	**CO-to-Ethanol conversion yield** %
1D model	0.51	24.88
LanzaTech	2.083	26
Difference	75.5 %	4.3 %

Conclusion

The optimization of the syngas fermentation in the 1D model was accomplished by varying the parameters: dilution rate (D_{il}), biomass concentration (C_X) and gas mass inflow rate (m_{in}). The most optimal values of these parameters were identified and implemented in the 1D model. The ethanol productivity predicted deviated the LanzaTech process, yet within the same order of magnitude and CO conversion yield was predicted in the same range as the LanzaTech process. Therefore, the validity of the predictions made by the 1D model for the industrial syngas fermentation were considered to be inconclusive. More data is necessary to obtain an accurate comparison between the syngas fermentation in the 1D model and industrial LanzaTech process, hence the validity of the 1D model to describe an industrial fermentation can be identified.

Chapter 4

Conclusion & Recommendations

4.1 Conclusion

In this thesis the modelling of a 1D ELGLR for syngas fermentation with *C. autoethanogenum* was accomplished. The model was considered to give rough estimations, yet within the same order of magnitude for the characteristic hydrodynamic parameters, superficial gas and liquid velocities and gas/liquid hold-ups of practical ELGLRs presented in literature. The accuracy of the syngas fermentation parameters, mass transfer, CO uptake rates and dissolved CO concentrations, could not be validated with the CFD model or the experimental data from literature due to the lack of sufficient experimental data in literature and the assumptions and simplifications made in the 1D model. The syngas fermentation was optimized through adjustment of variable parameters, dilution rate, mass gas inflow rate and biomass inlet concentration. The ethanol productivity and CO-to-ethanol conversion yield and rough estimations of the industrial process could not be used for validation due to the lack of data and assumptions made for the industrial process.

4.2 Recommendations model & future prospectives

The 1D model can be further improved by replacing the optimization procedure for the superficial liquid velocity and gas hold-up in the riser to incorporate variation of these parameters throughout the reactor, which has influence on the mass transfer and reactions. Additionally, the circular dependencies of the superficial liquid velocity and the gas hold-up and bubble diameter and bubble rise velocity have to be resolved, to eliminate some assumptions used to solve the model. Therefore a method to overcome the circular dependencies has to be examined. Proper validation of the accuracy of the 1D model can be achieved by practical experiments. Experimental measurements could give a more accurate description of the hydrodynamic parameters: superficial liquid and gas velocities, gas hold-up and mixing, in the 1D model and can be used to establish general correlations for these hydrodynamic parameters an 1D ELGLR.

For future studies several aspects are considered to generally contribute to the understanding and improvement of syngas fermentation in a practical ELGLR and to improve the accuracy of the 1D model. The syngas conversion by *C. autoethanogenum* is a key aspect which requires more research. The uptake kinetics of CO by *C. autoethanogenum* have to be determined more accurately as this would provide better understanding of the conversion of CO to ethanol, since the CO uptake rate proposed by Mohammadi et al. (2014) did not incorporate the dissolved concentrations of the gaseous compounds. The CO uptake could be determined at a steady state syngas fermentation in a practical reactor by measuring the dissolved gas concentrations. A possible method is to measure the dissolved CO concentration with a gas chromatography mass spectrometer as proposed by Abrahamson (2019). Additionally, the ethanol production and other products can be measured by taking samples of the fermentation broth in time and analyse these with liquid chromatography to determine the metabolites that are produced by *C. autoethanogenum*. Determination of the amount of other metabolites such as acetate can contribute to improvement of syngas fermentation in *C. autoethanogenum*, since the conversion yields and all products produced can be derived which could be useful for genetical modification of certain production path-

ways in *C. autoethanogenum*. Furthermore, the inhibition of CO and ethanol on the metabolism of *C. autoethanogenum* and CO uptake rate have to be examined to establish an operating range in which *C. autoethanogenum* can achieve the highest CO conversion and ethanol productivity. Subsequently, the ethanol tolerance of *C. autoethanogenum* can be improved to obtain higher ethanol productivities which are crucial for commercialization of the syngas fermentation process. The ethanol tolerance of *C. autoethanogenum* used by the industrial process of LanzaTech is hypothesized to be modified since high ethanol titers are achieved (Heijstra et al., 2019). Higher tolerance can be achieved by genetic modifications in *C. autoethanogenum* or with evolution experiments. Several genetic tools such as CRISPR Cas can be used to modify of *C. autoethanogenum* which require more knowledge on the genome and metabolism. The kinetics that are obtained through experiments can be used in a kinetic model of *C. autoethanogenum*. A model would provide the opportunity to study the behaviour of *C. autoethanogenum* under fermentation conditions in a bioreactor. By coupling the kinetic model with a large scale external loop gaslift reactor model, the influence of substrate gradients in the reactor on the metabolism of *C. autoethanogenum* can be examined. Since the environmental conditions, such as pH, influence the product spectrum of *C. autoethanogenum* (Richter et al., 2016). In addition, the implementation of these two models could aid in the scale-up of syngas fermentation.

Establishing a more detailed ELGLR model could more accurately describe the hydrodynamics of an ELGLR. An example of a more detailed model could be a CFD model. In such a model the axial dispersion coefficient, turbulence and bubble size distributions can be included (Roy and Joshi, 2006). The bubble size distributions can provide a more accurate representation of mass transfer in the reactor, since the mass transfer is dependent on the gas/liquid surface area. Whereas turbulence can model a heterogeneous flow regime which is often present in large scale ELGLRs. In addition, the local parameters such as gas hold-up and gas/liquid velocities can be predicted which might aid in determination of the local conditions for the micro-organism present in the reactor. Additionally, a CFD model with similar input parameters as the 1D model could be a method to verify the accuracy of the 1D model more. Increasing the level of detail in a CFD, increases the computational intensity which is considered a drawback.
Biomass retention in an actual large scale ELGLR should be further examined. Due to the low growth rate of *C. autoethanogenum*, high inlet biomass concentrations are necessary, which results in high costs. Recycling the biomass could reduce the amount of biomass that is being fed to the reactor. The retention can be achieved by incorporating filters to retain the biomass in the reactor. For industrial purposes more research has to be conducted on the type of retention system used.
Co-culture fermentation requires further research since this allows the formation of higher valuable compounds through chain elongation. Moreover, in this process the ethanol inhibition on *C. autoethanogenum* can be minimized since, ethanol is consumed by the second micro-organism present in the reactor.

Acknowlegdements

The past 9 months I was lucky enough to get the opportunity to learn a lot about syngas fermentation and its potential for the future. First of all I would like to very much thank Lars for letting me participate in a small part of his very interesting and promising research. His affection and knowledge about syngas fermentation kept me highly motivated and sharp at all times, even at the 2 or 3 hour online meetings we had and even in the last few weeks managed to get the best out of myself. For this I am very thankful since this was complicated during the Covid situation.

Furthermore, I want to thank Cristian Picioreanu, Marcel Ottens and Henk Noorman for participating in the thesis committee. I would like to thank Cristian, for the long online meetings we had to help with solving and definition problems in the model, even when in different countries.
Furthermore, I would like to thank the whole BPE group for making me feel more than welcome during the online coffeebreaks and multiple online pubquiz's, which I really enjoyed.

A special thanks to my parents and sister who have been a great support throughout my bachelors and masters, which made it possible for me to achieve all the goals I envisioned.
Also, I want to thank my roommates, friends and Thijmen which have been a real support during the 9 (intense) months.

Bibliography

J. Abrahamson. Conceptual Design and Evaluation of a Commercial Syngas Fermentation Process. Technical report, TU Delft, 2019.

J. Abrini, H. Naveau, and E. J. Nyns. Clostridium autoethanogenum, sp. nov., an anaerobic bacterium that produces ethanol from carbon monoxide. *Archives of Microbiology*, 161(4):345–351, 1994. ISSN 03028933. doi: 10.1007/BF00303591.

H. N. Abubackar, M. C. Veiga, and C. Kennes. Biological conversion of carbon monoxide: rich syngas or waste gases to bioethanol. *Biofuels, Bioproducts and Biorefining*, 5(1):93–114, 1 2011. ISSN 1932104X. doi: 10.1002/bbb.256. URL http://doi.wiley.com/10.1002/bbb.256.

K. Asimakopoulos, H. N. Gavala, and I. V. Skiadas. Reactor systems for syngas fermentation processes: A review. *Chemical Engineering Journal*, 348(April):732–744, 2018. ISSN 13858947. doi: 10.1016/j.cej.2018.05.003. URL https://doi.org/10.1016/j.cej.2018.05.003.

R. A. Bello, C. W. Robinson, and M. MooYoung. Gas holdup and overall volumetric oxygen transfer coefficient in airlift contactors. *Biotechnology and Bioengineering*, 27(3):369–381, 1985. ISSN 10970290. doi: 10.1002/bit.260270323.

M. D. Bredwell and R. M. Worden. Mass-Transfer Properties of Microbubbles. 1. Experimental Studies. *Biotechnology Progress*, 14:31–38, 1998.

M. D. Bredwell, P. Srivastava, and R. Mark Worden. Reactor Design Issues for Synthesis-Gas Fermentations. *Biotechnology Progress*, 15:834–844, 1999. doi: 10.1021/bp990108m.

P. H. Calderbank and M. B. Moo-Young. The continuous phase heat and mass transfer properties of dispersions. *Chemical Engineering Science*, 50(24):3921–3934, 12 1995. ISSN 00092509. doi: 10.1016/0009-2509(96)81823-9.

J. Chen, J. A. Gomez, K. Höffner, P. I. Barton, and M. A. Henson. Metabolic modeling of synthesis gas fermentation in bubble column reactors. *Biotechnology for Biofuels*, 8(1):1–12, 2015. ISSN 17546834. doi: 10.1186/s13068-015-0272-5. URL http://dx.doi.org/10.1186/s13068-015-0272-5.

J. Chen, J. Daniell, D. Griffin, X. Li, and M. A. Henson. Experimental testing of a spatiotemporal metabolic model for carbon monoxide fermentation with Clostridium autoethanogenum. *Biochemical Engineering Journal*, 129:64–73, 2018. ISSN 1369-703X. doi: https://doi.org/10.1016/j.bej.2017.10.018. URL http://www.sciencedirect.com/science/article/pii/S1369703X17303029.

M. Y. Chisti and M. Moo-Young. Airlift Reactors: Characteristics, Applications and Design Considerations. *Chemical Engineering Communications*, 60(1-6):195–242, 1987. ISSN 15635201. doi: 10.1080/00986448708912017.

M. Y. Chisti and M. Moo-Young. Improve the performance of airlift reactors. *Chemical Engineering Progress*, pages 38–45, 1993.

M. Y. Chisti, B. Halard, and M. Moo-Young. Liquid circulation in airlift reactors. *Chemical Engineering Science*, 43(3):451–457, 1988. ISSN 00092509. doi: 10.1016/0009-2509(88)87005-2.

E. Cussler. Values of Diffusion coefficients. In *Diffusion: Mass transfer in fluid systems*, chapter 5, pages 117–161. Cambridge University Press, 2009.

P. V. Danckwerts. Continuous flow systems. Distribution of residence times. *Chemical Engineering Science*, 2(1):1–13, 2 1953. ISSN 00092509. doi: 10.1016/0009-2509(53)80001-1.

J. Daniell, M. Köpke, and S. D. Simpson. Commercial biomass syngas fermentation. *Energies*, 5(12): 5373–5417, 2012. ISSN 19961073. doi: 10.3390/en5125372.

R. Datta, S.-P. Tsai, R. Tasu, and S.-H. Yoon. Process for converting syngas to liquid products with micro organisms on two-layer membrane, 2012.

E. M. de Medeiros, J. A. Posada, H. Noorman, and R. M. Filho. Dynamic modeling of syngas fermentation in a continuous stirred-tank reactor: Multi-response parameter estimation and process optimization. *Biotechnology and Bioengineering*, 116(10):2473–2487, 2019. ISSN 10970290. doi: 10.1002/bit.27108.

M. Diender, I. Parera Olm, M. Gelderloos, J. J. Koehorst, P. J. Schaap, A. J. Stams, and D. Z. Sousa. Metabolic shift induced by synthetic co-cultivation promotes high yield of chain elongated acids from syngas. *Scientific Reports*, 9(1):1–11, 2019. ISSN 20452322. doi: 10.1038/s41598-019-54445-y. URL `http://dx.doi.org/10.1038/s41598-019-54445-y`.

F. Garcia-Ochoa and E. Gomez. Bioreactor scale-up and oxygen transfer rate in microbial processes: An overview, 3 2009. ISSN 07349750.

J. J. Heijnen and K. van 't Riet. Mass Transfer, Mixing and Heat Transfer Phenomena in Low Viscosity Bubble Column Reactors. *Chemical Engineering*, 28, 1984.

B. D. Heijstra, E. Kern, M. Kopke, S. Segovia, and F. Liew. Bacteria and methods of use thereof, 2019.

J. H. Hills. The operation of a bubble column at high throughputs. I. Gas holdup measurements. *The Chemical Engineering Journal*, 12(2):89–99, 1976. ISSN 03009467. doi: 10.1016/0300-9467(76)87002-5.

N. Jang, M. Yasin, S. Park, R. W. Lovitt, and I. S. Chang. Determination of volumetric gasliquid mass transfer coefficient of carbon monoxide in a batch cultivation system using kinetic simulations. *Bioresource Technology*, 239:387–393, 2017. ISSN 18732976. doi: 10.1016/j.biortech.2017.05.023. URL `http://dx.doi.org/10.1016/j.biortech.2017.05.023`.

L. Janssen and M. Warmoeskerken. Transport Phenomena Data Companion. pages 74,100, 1987.

S. T. Jones. Gas liquid mass transfer in an external airlift loop reactor for syngas fermentation. *Iowa State University*, page 378, 2007.

R. Kleerebezem and M. C. M. Van Loosdrecht. A Generalized Method for Thermodynamic State Analysis of Environmental Systems. *Critical Reviews in Environmental Science and Technology*, 40(1):1–54, 2010. ISSN 1547-6537. doi: 10.1080/10643380802000974. URL `https://www.tandfonline.com/action/journalInformation?journalCode=best20`.

M. Köpke and S. D. Simpson. Pollution to products: recycling of above ground carbon by gas fermentation. *Current Opinion in Biotechnology*, 65:180–189, 2020. ISSN 18790429. doi: 10.1016/j.copbio.2020.02.017.

M. Köpke, C. Mihalcea, J. C. Bromley, and S. D. Simpson. Fermentative production of ethanol from carbon monoxide. *Current Opinion in Biotechnology*, 22(3):320–325, 2011a. ISSN 09581669. doi: 10.1016/j.copbio.2011.01.005.

M. Köpke, C. Mihalcea, F. M. Liew, J. H. Tizard, M. S. Ali, J. J. Conolly, B. Al-Sinawi, and S. D. Simpson. 2,3-Butanediol production by acetogenic bacteria, an alternative route to chemical synthesis, using industrial waste gas. *Applied and Environmental Microbiology*, 77(15):5467–5475, 2011b. ISSN 00992240. doi: 10.1128/AEM.00355-11.

X. Li, B. J. Cossey, and S. R. Trevethick. Fermentation of Gaseous substrate, 2017.

X. Li, D. Griffin, X. Li, and M. A. Henson. Incorporating hydrodynamics into spatiotemporal metabolic models of bubble column gas fermentation. *Biotechnology and Bioengineering*, 116(1):28–40, 2019. ISSN 10970290. doi: 10.1002/bit.26848.

F. M. Liew, M. E. Martin, R. C. Tappel, B. D. Heijstra, C. Mihalcea, and M. Köpke. Gas Fermentation-A flexible platform for commercial scale production of low-carbon-fuels and chemicals from waste and renewable feedstocks. *Frontiers in Microbiology*, 7(MAY), 2016. ISSN 1664302X. doi: 10.3389/fmicb.2016.00694.

J.-C. Liou and E. L. Madsen. Microbial Ecological Processes: Aerobic/Anaerobic. In S. E. Jørgensen and B. D. B. T. E. o. E. Fath, editors, *Earth systems & environmental sciences*, pages 2348–2357. Academic Press, Oxford, 2008. ISBN 978-0-08-045405-4. doi: https://doi.org/10.1016/B978-008045405-4.00254-8. URL http://www.sciencedirect.com/science/article/pii/B9780080454054002548.

S. Mazumder. The Finite Difference Method. In *Numerical Methods for Partial Differential Equations*, pages 51–101. Elsevier, 1 2016. doi: 10.1016/B978-0-12-849894-1.00002-0. URL https://linkinghub.elsevier.com/retrieve/pii/B9780128498941000020.

J. Merchuk and F. Garcia Camacho. Bioreactors: Airlift Reactors. In *Encyclopedia of Industrial Biotechnology*, number 19, pages 1–62. Encyclopedia of Industrial Biotechnology, Almeria, 2010. doi: 10.1002/9780470054581.eib144.

M. Mohammadi, G. D. Najafpour, H. Younesi, P. Lahijani, M. H. Uzir, and A. R. Mohamed. Bioconversion of synthesis gas to second generation biofuels: A review. *Renewable and Sustainable Energy Reviews*, 15(9):4255–4273, 2011. ISSN 13640321. doi: 10.1016/j.rser.2011.07.124. URL http://dx.doi.org/10.1016/j.rser.2011.07.124.

M. Mohammadi, A. R. Mohamed, G. D. Najafpour, H. Younesi, and M. H. Uzir. Kinetic studies on fermentative production of biofuel from synthesis gas using clostridium ljungdahlii. *The Scientific World Journal*, 2014(1), 2014. ISSN 1537744X. doi: 10.1155/2014/910590.

R. F. Mudde and H. E. Van Den Akker. 2D and 3D simulations of an internal airlift loop reactor on the basis of a two-fluid model. *Chemical Engineering Science*, 56(21-22):6351–6358, 2001. ISSN 00092509. doi: 10.1016/S0009-2509(01)00222-6.

P. C. Munasinghe and S. K. Khanal. Biomass-derived syngas fermentation into biofuels: Opportunities and challenges. *Bioresource Technology*, 101(13):5013–5022, 2010a. ISSN 09608524. doi: 10.1016/j.biortech.2009.12.098. URL http://dx.doi.org/10.1016/j.biortech.2009.12.098.

P. C. Munasinghe and S. K. Khanal. Syngas fermentation to biofuel: Evaluation of carbon monoxide mass transfer coefficient (kLa) in different reactor configurations. *Biotechnology Progress*, 26(6):1616–1621, 2010b. ISSN 87567938. doi: 10.1002/btpr.473.

National EnergyTechnology Laboratory. Alternatives/Supplements to Coal - Feedstock Flexibility, 2014. URL http://www.netl.doe.gov/research/Coal/energy-systems/gasification/gasifipedia/feedstock.

J. J. Orgill, H. K. Atiyeh, M. Devarapalli, J. R. Phillips, R. S. Lewis, and R. L. Huhnke. A comparison of mass transfer coefficients between trickle-bed, Hollow fiber membrane and stirred tank reactors. *Bioresource Technology*, 133:340–346, 4 2013. ISSN 18732976. doi: 10.1016/j.biortech.2013.01.124.

S. H. Park, C. Park, J. Y. Lee, and B. Lee. A Simple Parameterization for the Rising Velocity of Bubbles in a Liquid Pool. *Nuclear Engineering and Technology*, 49(4):692–699, 2017. ISSN 2234358X. doi: 10.1016/j.net.2016.12.006. URL http://dx.doi.org/10.1016/j.net.2016.12.006.

S. Paul and A. Dutta. Challenges and opportunities of lignocellulosic biomass for anaerobic digestion. *Resources, Conservation and Recycling*, 130(March 2017):164–174, 2018. ISSN 18790658. doi: 10.1016/j.resconrec.2017.12.005. URL https://doi.org/10.1016/j.resconrec.2017.12.005.

L. Puiman. Modelling syngas fermentation in hollow fibre membrane reactors. Technical report, TU Delft, 2020.

H. Richter, M. E. Martin, and L. T. Angenent. A two-stage continuous fermentation system for conversion of syngas into ethanol. *Energies*, 6(8):3987–4000, 2013. ISSN 19961073. doi: 10.3390/en6083987.

H. Richter, B. Molitor, H. Wei, W. Chen, L. Aristilde, and L. T. Angenent. Ethanol production in syngas-fermenting: Clostridium ljungdahlii is controlled by thermodynamics rather than by enzyme expression. *Energy and Environmental Science*, 9(7):2392–2399, 2016. ISSN 17545706. doi: 10.1039/c6ee01108j.

S. Roy and J. Joshi. Effect of Liquid Velocity on Axial Mixing in Gas-Liquid Dispersions: A CFD Simulation. *Chemical Engineering Technology*, 29(9):1034–1041, 2006. doi: 10.1002/ceat.200600154. URL `http://www.cet-journal.com`.

Y. T. Shah, B. G. Kelkar, S. P. Godbole, and W. D. Deckwer. Design parameters estimations for bubble column reactors. *AIChE Journal*, 28(3):353–379, 1982. ISSN 15475905. doi: 10.1002/aic.690280302.

Y. Shen, R. Brown, and Z. Wen. Syngas fermentation of Clostridium carboxidivoran P7 in a hollow fiber membrane biofilm reactor: Evaluating the mass transfer coefficient and ethanol production performance. *Biochemical Engineering Journal*, 85:21–29, 4 2014. ISSN 1369703X. doi: 10.1016/j.bej.2014.01.010.

F. Siebler, A. Lapin, and R. Takors. Synergistically applying 1-D modeling and CFD for designing industrial scale bubble column syngas bioreactors. *Engineering in Life Sciences*, 20(7):239–251, 2020. ISSN 16182863. doi: 10.1002/elsc.201900132.

M. H. Siegel and J. C. Merchuk. Mass transfer in a rectangular airlift reactor: Effects of geometry and gas recirculation. *Biotechnology and Bioengineering*, 32(9):1128–1137, 1988. ISSN 10970290. doi: 10.1002/bit.260320906.

I. K. Stoll, N. Boukis, and J. Sauer. Syngas Fermentation to Alcohols: Reactor Technology and Application Perspective. *Chemie-Ingenieur-Technik*, 92(1-2):125–136, 2020. ISSN 15222640. doi: 10.1002/cite.201900118.

K. Valgepea, R. De Souza Pinto Lemgruber, T. Abdalla, S. Binos, N. Takemori, A. Takemori, Y. Tanaka, R. Tappel, M. Köpke, S. D. Simpson, L. K. Nielsen, and E. Marcellin. H2 drives metabolic rearrangements in gas-fermenting Clostridium autoethanogenum. *Biotechnology for Biofuels*, 11(1): 1–15, 2018. ISSN 17546834. doi: 10.1186/s13068-018-1052-9. URL `https://doi.org/10.1186/s13068-018-1052-9`.

K. van't Riet and R. G. van der Lans. *Mixing in Bioreactor Vessels*, volume 2. Elsevier B.V., second edi edition, 2011. ISBN 9780080885049. doi: 10.1016/B978-0-08-088504-9.00083-0. URL `http://dx.doi.org/10.1016/B978-0-08-088504-9.00083-0`.

P. Verlaan. *Modelling and characterization of an airlift-loop bioreactor*. PhD thesis, Wageningen, 1987.

P. Verlaan, J. Tramper, K. Van't Reit, and K. C. Luyben. A hydrodynamic model for an airlift-loop bioreactor with external loop. *The Chemical Engineering Journal*, 33(2):43–53, 1986. ISSN 03009467. doi: 10.1016/0300-9467(86)80052-1.

P. Verlaan, J. Vos, and K. Van T Riet. Hydrodynamics of the flow transition from a bubble column to an airliftloop reactor. *Journal of Chemical Technology & Biotechnology*, 45(2):109–121, 1989. ISSN 10974660. doi: 10.1002/jctb.280450204.

C. Vial, S. Poncin, G. Wild, and N. Midoux. Experimental and theoretical analysis of the hydrodynamics in the riser of an external loop airlift reactor. *Chemical Engineering Science*, 57(22-23):4745–4762, 2002. ISSN 00092509. doi: 10.1016/S0009-2509(02)00284-1.

N. C. WebBook. NIST database.

J. Yang, Y. Liu, J. Chang, Y. N. Wang, L. Bai, Y. Y. Xu, H. W. Xiang, Y. W. Li, and B. Zhong. Detailed kinetics of Fischer-Tropsch synthesis on an industrial Fe-Mn catalyst. *Industrial and Engineering Chemistry Research*, 42(21):5066–5090, 2003. ISSN 08885885. doi: 10.1021/ie030135o.

M. Yasin, N. Jang, M. Lee, H. Kang, M. Aslam, A. A. Bazmi, and I. S. Chang. Bioreactors, gas delivery systems and supporting technologies for microbial synthesis gas conversion process. *Bioresource Technology Reports*, 7(April):100207, 2019. ISSN 2589014X. doi: 10.1016/j.biteb.2019.100207. URL `https://doi.org/10.1016/j.biteb.2019.100207`.

M. A. Young, R. G. Carbonell, and D. F. Ollis. Airlift bioreactors: Analysis of local twophase hydrodynamics. *AIChE Journal*, 37(3):403–428, 1991. ISSN 15475905. doi: 10.1002/aic.690370311.

Appendix A

Mass balances

A.1 Mass balance derivation

The convection-dispersion mass balances that are used to describe the 1D ELGLR model are derived from simple molar mass balances. The derivation of the mass balances was performed, to understand and implement two phases of an ELGLR in a 1D model. The dimensions of the mass balances are presented by amount of mass (mole) per phase volume (m^3_L or m^3_G) per unit of time (s).

Liquid phase

$$(\Delta N_i)_t - (\Delta N_i)_{t+\Delta t} = (N_i)_{x,t} - (N_i)_{x+\Delta x,t} + k_L \Delta c_{L,i} \Delta A_{GL} \Delta t - q_i C_x \Delta x A_L \Delta t \tag{A.1}$$

Divide by Δt and take the limit: $\Delta t \to 0$ and $\frac{dn_i}{dt} = \lim_{x\to 0} \frac{\Delta N_i}{\Delta t}$. The molar flowrate ($n_i$) is given in mol/s.

$$\frac{dN_i}{dt} = (n_i)_x - (n_i)_{x+\Delta x} + k_L \Delta c_{L,i} \Delta A_{GL} - q_i C_x \Delta x A_L \tag{A.2}$$

$$\frac{dn_i}{dt} = (n_i)_x - (n_i)_{x+\Delta x} + k_L \Delta c_{L,i} \Delta A_{GL} - q_i C_x \Delta x A_L \tag{A.3}$$

$$a = \frac{\Delta A_{GL}}{V_R} = \frac{\Delta A_{GL}}{A_T \Delta x}$$

$$A_T = \frac{A_L}{\varepsilon_L}$$

$$\frac{dN_i}{dt} = (n_i)_x - (n_i)_{x+\Delta x} + k_L \Delta c_{L,i} a A_T \Delta x - q_i C_x A_L \Delta x \tag{A.4}$$

The moles are converted to concentration by dividing the mass balance with the reactor volume: $V_R = A_T \Delta x$ which can be written as the liquid volume: $V_L = \varepsilon_L V_R$. Similarly, the area of the liquid can be calculated: $A_L = \varepsilon_L A_R$.

$$\frac{1}{A_T \Delta x} \frac{dN_i}{dt} = \frac{1}{A_T} \frac{[n_i|_x - n_i|_{x+\Delta x}]}{\Delta x} + k_L a \Delta c_{L,i} - q_i C_x \frac{A_L \Delta x}{A_T \Delta x}$$

The general convection-dispersion equation can be written as: $J_i = \frac{n_i}{A_L} = \mathrm{u_L} C_i - D_L \frac{\partial C_i}{\partial x}$

$$\varepsilon_L \frac{dC_i}{dt} = \varepsilon_L [\frac{J_i|_x - J_i|_{x+\Delta x}}{\Delta x}] + k_L a \Delta c_{L,i} - q_i C_x \varepsilon_L$$

Take the limit where $\Delta x \to 0$: $-\frac{\partial J_i}{\partial x} = \lim_{x\to 0} \frac{\Delta J_i}{\Delta x}$

$$\varepsilon_L \frac{\partial C_i}{\partial t} = \varepsilon_L[-\mathrm{u_L}\frac{\partial C_i}{\partial x} + D_L \frac{\partial^2 C_i}{\partial x^2}] + k_L a \Delta c_{L,i} - q_i C_x \varepsilon_L$$

The velocity $\mathrm{u_L}$ is defined as m_R/s, which is converted to the superficial liquid velocity, u_{L_s} ($\mathrm{m}_L^3/\mathrm{m}_R^2/\mathrm{s}$) with the liquid hold-up (ε_L).

$$\varepsilon_L \frac{\partial C_i}{\partial t} = -u_{Ls}\frac{\partial C_i}{\partial x} + \varepsilon_L D_L \frac{\partial^2 C_i}{\partial x^2} + k_L a \Delta c_{L,i} - q_i C_x \varepsilon_L$$

Similarly,

$$\frac{\partial C_i}{\partial t} = -\frac{u_{Ls}}{\varepsilon_L}\frac{\partial C_i}{\partial x} + D_L \frac{\partial^2 C_i}{\partial x^2} + \frac{k_L a \Delta c_{L,i}}{\varepsilon_L} - q_i C_x$$

The dimensions of the mass balances are checked, which are in $\mathrm{mol}/\mathrm{m}_L^3/\mathrm{s}$.

$$\begin{aligned}\frac{mol}{m_L^3 s} &= -\frac{\frac{m_L^3}{m_R^2 s}}{\frac{m_L^3}{m_R^3}}\frac{\frac{mol}{m_L^3}}{m_R} + \frac{m_R^2}{s}\frac{\frac{mol}{m_L^3}}{m_R^2} + \frac{\frac{mol}{m_R^3 s}}{\frac{m_L^3}{m_R^3}} - \frac{mol}{m_L^3 s} \\ &= -\frac{mol}{m_L^3 s} + \frac{mol}{m_L^3 s} + \frac{mol}{m_L^3 s} - \frac{mol}{m_L^3 s}\end{aligned}$$

Gas phase

$$(\Delta N_i)_t - (\Delta N_i)_{t+\Delta t} = (N_i)_{x,t} - (N_i)_{x+\Delta x,t} - k_L \Delta C_{L,i} \Delta A_{GL} \Delta t \tag{A.5}$$

Divide by Δt and take the limit: $\Delta t \to 0$ and $\frac{dn_i}{dt} = \lim_{x\to 0} \frac{\Delta N_i}{\Delta t}$. The molar flowrate ($n_i$) is given in mol/s.

$$\frac{dN_i}{dt} = (n_i)_x - (n_i)_{x+\Delta x} - k_L \Delta C_{L,i} \Delta A_{GL} \tag{A.6}$$

$$\frac{dn_i}{dt} = (n_i)_x - (n_i)_{x+\Delta x} - k_L \Delta C_{L,i} \Delta A_{GL} \tag{A.7}$$

$$a = \frac{\Delta A_{GL}}{V_R} = \frac{\Delta A_{GL}}{A_T \Delta x}$$

$$A_T = \frac{A_G}{\varepsilon_G}$$

$$\frac{dN_i}{dt} = (n_i)_x - (n_i)_{x+\Delta x} - k_L \Delta C_{L,i} a A_T \Delta x \tag{A.8}$$

The moles are converted to concentration by dividing the mass balance with the reactor volume: $V_R = A_T \Delta x$ which can be written as the gas volume: $V_G = \varepsilon_G V_R$. Similarly, the area that is occupied by the gas can be calculated: $A_G = \varepsilon_G A_R$.

$$\frac{1}{A_T \Delta x} \frac{dN_i}{dt} = \frac{1}{A_T} \frac{[n_i|_x - n_i|_{x+\Delta x}]}{\Delta x} - k_L a \Delta C_{L,i}$$

The general convection-dispersion equation can be written as: $J_i = \frac{n_i}{A_G} = \mathrm{u_G} C_i - D_G \frac{\partial C_i}{\partial x}$

$$\varepsilon_G \frac{dC_i}{dt} = \varepsilon_G [\frac{J_i|_x - J_i|_{x+\Delta x}}{\Delta x}] - k_L a \Delta C_{L,i}$$

Take the limit $\Delta x \to 0$: $-\frac{\partial J_i}{\partial x} = \lim_{x\to 0} \frac{\Delta J_i}{\Delta x}$

$$\varepsilon_G \frac{\partial C_i}{\partial t} = \varepsilon_G [-\mathrm{u_G} \frac{\partial C_i}{\partial x} + D_G \frac{\partial^2 C_i}{\partial x^2}] - k_L a \Delta C_{L,i}$$

The velocity $\mathrm{u_G}$ is defined as m_R/s, which is converted to the superficial gas velocity, u_{G_s} ($\mathrm{m}^3_G/\mathrm{m}^2_R$/s) with the gas hold-up (ε_G).

$$\varepsilon_G \frac{\partial C_i}{\partial t} = -u_{Gs} \frac{\partial C_i}{\partial x} + \varepsilon_G D_G \frac{\partial^2 C_i}{\partial x^2} - k_L a \Delta C_{L,i}$$

Similarly,

$$\frac{\partial C_i}{\partial t} = -\frac{u_{Gs}}{\varepsilon_G} \frac{\partial C_i}{\partial x} + D_G \frac{\partial^2 C_i}{\partial x^2} - \frac{k_L a \Delta C_{L,i}}{\varepsilon_G}$$

The dimensions of the mass balances are checked.

$$\frac{mol}{m_G^3 s} = -\frac{\frac{m_G^3}{m_R^2 s}}{\frac{m_G^3}{m_R^3}} \frac{\frac{mol}{m_G^3}}{m_R} + \frac{m_R^2}{s} \frac{\frac{mol}{m_G^3}}{m_R^2} - \frac{\frac{mol}{m_R^3 s}}{\frac{m_G^3}{m_R^3}}$$

$$= -\frac{mol}{m_G^3 s} + \frac{mol}{m_G^3 s} - \frac{mol}{m_G^3 s}$$

A.2 Mass balance calculation

The mass balances are calculated for each individual reactor section, phase and species according the equations proposed in section 2.2. The error percentage difference is calculated by the difference between the mass that goes in and out divided by the mass that goes in to that specific reactor part.

Table A.1: Mass balance inflow riser. In and outlet of the inflow riser are calculated in mol/s. The error represents the difference in the mass between the in and outlet of the inflow riser. The error is given in mol/s and in percentage difference.

Compound	In	Out	error	error %
X	32.9283626	32.9283626	0	0

Table A.2: Mass balance gas phase riser. In and outlet of the gas in the riser are calculated in mol/s. The error represents the difference in the mass between the in and outlet of the riser. The error is given in mol/s and in percentage difference.

Compound	In	Out	Mass transfer	error	error %
CO	8.592528705	7.427535459	-1.164996628	-3.38158E-06	-3.93549E-05
N_2	8.592528705	8.592527625	-	1.08045E-06	1.25743E-05

Table A.3: Mass balance liquid phase riser. In and outlet of the riser are calculated in mol/s. The error represents the difference in the mass between the in and outlet of the riser. The error is given in mol/s and in percentage difference.

Compound	In	Out	MT	Reaction	error	error %
CO	1.99828E-05	0.003140841	1.164996628	-1.161859826	1.594E-05	0.001368534
EtOH	9.584411338	9.773158481	-	0.188760788	1.36453E-05	0.00014237
X	1491.107337	1491.121299	-	0.013963345	7.16316E-07	4.80387E-08

Table A.4: Mass balance downcomer. In and outlet of the downcomer are calculated in mol/s. The error represents the difference in the mass between the in and outlet of the downcomer. The error is given in mol/s and in percentage difference.

Compound	In	Out	Reaction	error	error %
CO	0.003067503	4.93424E-40	-0.003068047	-5.43994E-07	-0.017734107
EtOH	9.557256946	9.584408129	0.02715127	8.64255E-08	9.04291E-07
X	1458.178971	1458.178974	2.42468E-06	6.56779E-09	4.50411E-10

The mass balance of CO in the outflow riser did not close due to the reaction rate in the outflow riser, since the balance did close when neglecting the reaction rate. It is presumed that the length of the outflow riser causes the balance not to close. Therefore, the characteristic time of the reaction and convection are determined (eqn. A.9, A.10). The reaction time is much smaller than the convective time, as a consequence the reaction rate is much higher than the difference between the convective in and outflow (mol/s) of the outflow riser. The outflow riser has no influence on calculations in other parts of the model and the ethanol and biomass balance in the outflow riser close, therefore the error is considered negligible yet more research can be performed to clarify the difference.

$$\tau_{conv} = \frac{L}{u} = 93.16s \tag{A.9}$$

$$\tau_{reac} = \frac{K_s + C_{L,CO} + C_{L,CO}^2/K_I}{q_{\max,CO} C_{L,X}} = 0.2168s \tag{A.10}$$

Table A.5: Mass balance outflow riser. In and outlet of the outflow riser are calculated in mol/s. The error represents the difference in the mass between the in and outlet of the outflow riser. The error is given in mol/s and in percentage difference.

Compound	**In**	**Out**	**Reaction**	**error**	**error %**
CO	0.002904234	0.000388272	-0.0031450	-0.0006290	-21.65769092
EtOH	0.215469349	0.21586317	0.000490956	9.71349E-05	0.045080631
X	32.94215363	32.94232836	1.59276E-05	-0.000158801	-0.00048206

Appendix B

Hydrodynamic parameters

The hydrodynamic parameters that were derived and calculated are elucidated for the 1D ELGLR model are elucidated in this section.

B.1 Gas phase

B.1.1 Superficial gas velocity riser - u_{G_r}

In the gas phase the superficial gas velocity was derived from the gas phase mass balance at steady state (eqn. B.11). The derivation starts with the gas phase mass balance is rewritten with the ideal gas law (eqn. B.2). The concentration of a gaseous compound can be defined as the fraction (y_i) of the total gas concentration (eqn. B.3).

$$\varepsilon_{G_r} \frac{\partial C_{G_r,i}}{\partial t} = -\frac{\partial C_{G_r,i} u_{G_r}}{\partial x} - k_L a \Delta C_{L_r,i} \tag{B.1}$$

$$PV = nRT \tag{B.2}$$

$$c_{tot} = \frac{n}{V} = \frac{P}{RT} \quad \text{with} \quad c_i = y_i c_{tot} \tag{B.3}$$

$$\varepsilon_{G_r} \frac{\partial \frac{P y_i}{RT}}{\partial t} = -\frac{\partial \frac{P y_i}{RT} u_{G_r}}{\partial x} - k_L a \Delta C_{L_r,i} \tag{B.4}$$

The mole fraction (y_i) changes over time and over the length of the riser and the pressure (P) changes over the length of the riser. The gas constant (R) and temperature T are constant over time and the length of the riser (eqn. B.5).

$$\varepsilon_{G_r} \frac{P}{RT} \frac{\partial y_i}{\partial t} = -\frac{1}{RT} \frac{\partial P y_i u_{G_r}}{\partial x} - k_L a \Delta C_{L_r,i} \tag{B.5}$$

Taking the sum of equation B.6 represents all gaseous compounds in the gas phase. The sum of $y_i = 1$ (eqn. B.7), with $\frac{\partial 1}{\partial t} = 0$ (eqn. B.8).

$$\sum_i \varepsilon_{G_r} \frac{P}{RT} \frac{\partial y_i}{\partial t} = -\sum_i \frac{1}{RT} \frac{\partial P y_i u_{G_r}}{\partial x} - \sum_i k_L a \Delta C_{L_r,i} \tag{B.6}$$

$$\varepsilon_{G_r} \frac{P}{RT} \frac{\partial \sum_i y_i}{\partial t} = -\frac{1}{RT} \frac{\partial P u_{G_r} \sum_i y_i}{\partial x} - \sum_i k_L a \Delta C_{L_r,i} \tag{B.7}$$

$$0 = -\frac{1}{RT}\frac{dPu_{G_r}}{dx} - \sum_i k_L a \Delta C_{L_r,i} \tag{B.8}$$

The differential equation is solved with the chain rule (eqn. B.9). The pressure change over the length of the riser can be written as gravitational constant times the density of the gas and liquid phase in the riser: $\frac{dP}{dx} = -g\ (\rho_L e_{Lr} + \rho_G e_{Gr})$ (eqn. B.10). Equation B.9 is rewritten and the equation for the superficial gas velocity is obtained (eqn. B.11).

$$0 = -\frac{P}{RT}\frac{du_{G_r}}{dx} \cdot -\frac{1}{RT}u_{G_r}\frac{dP}{dx} - \sum_i k_L a \Delta C_{L_r,i} \tag{B.9}$$

$$\frac{du_{G_r}}{dx} = -\frac{g\, u_{G_r}\,(\rho_L e_{Lr} + \rho_G e_{Gr})}{P} - \frac{RT}{P}\sum_i k_L a \Delta C_{L_r,i} \tag{B.10}$$

$$\frac{du_{G_r}}{dx} = \frac{\rho_G g u_{G_r}}{P} - \frac{RT}{P}\sum_i (k_{L,i} a \Delta C_{L_r,i}) \tag{B.11}$$

B.1.2 Bubble rise velocity

The bubble rise velocity (v_r) was considered constant in the 1D model due to circular dependency between the bubble rise velocity, bubble diameter and mass transfer coefficient. The influence of the bubble rise velocity on the hydrodynamics in the 1D model was examined with a parametric analysis. The range of bubble rise velocities used for the analysis was based on Park et al. (2017). Park et al. (2017) presented a correlation for bubble rise velocities of spherical cap bubbles in a stagnant pool of liquid based on experimental data. The correlation was proposed to be applicable in a range of bubble diameters. The bubble rise velocity fluctuated between 23-28 cm/s for bubble diameters of 1-10 mm. This range of bubble diameters was considered to be applicable for bubbles in ELGLRs. Therefore, the range of 23-28 cm/s was chosen to perform the analysis with. Only the influence of the v_r on the k_L is analysed, since the bubble rise velocity is only considered in the mass transfer coefficient equation. The bubble diameter was calculated according to the equation proposed in section 2.3.1 and presented as well to analyse the influence of v_r on the bubble diameter d_b. The bubble rise velocity had very little influence on the bubble diameter, whereas the bubble rise velocity had more influence on the mass transfer coefficient ($\pm$ $0.55{\cdot}10^{-4}$ m/s) (fig. B.1). As a result, the bubble rise velocity was kept constant and the bubble diameter and mass transfer coefficient were varied. In addition, the bubble rise velocity is considered to reach its terminal rise velocity in an ELGLR (Young et al., 1991).

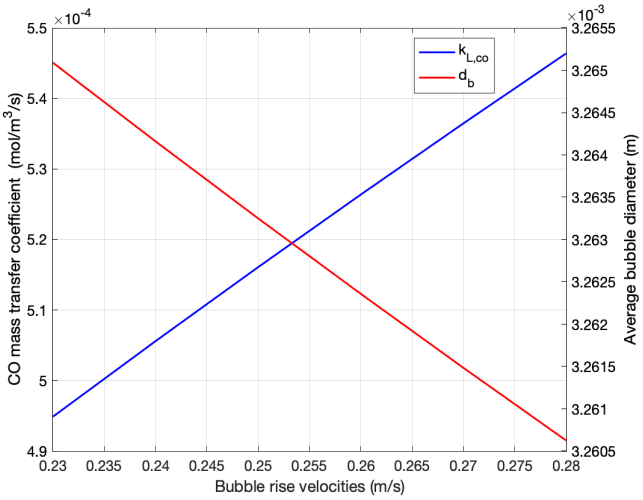

Figure B.1: Parametric analysis of the bubble rise velocity (v_b) for mass transfer coefficient ($k_{L_{co}}$) and bubble diameter (d_b). The blue and red line indicate the mass transfer coefficient and bubble diameter at the left and right y-axis, respectively.

B.2 Parameter calculations

B.2.1 Pressure - P

The equation describing the changing pressure over the length of a specific reactor part in an ELGLR was derived from equation B.12 (Li et al., 2019). The differential equation was integrated to describe the pressure at a certain x (eqn. B.13). The pressure at the bottom of the riser was calculated to calculate the inlet superficial gas velocity. To overcome circular dependency between the pressure and the gas density at the bottom of the riser, only the liquid density was considered since this contributes mostly to the pressure in the riser (eqn. B.14).

$$\frac{dP}{dx} = g\left(\rho_L e_{Lr} + \rho_G e_{Gr}\right) \tag{B.12}$$

$$P(x) = P_L + g\left(\rho_L e_{Lr} + \rho_G e_{Gr}\right)(L - x) \tag{B.13}$$

$$P_b = P(0) = P_L + (g\ \rho_L\ (L_r - 0)) = P_L + (g\ \rho_L\ L_r) \tag{B.14}$$

B.2.2 Saturation concentration gaseous compounds - C^*

The mass transfer of the gaseous compounds from the gas to the liquid phase is described by the liquid side mass transfer. It is assumed that at the gas-liquid interface an equilibrium exits, in which the partial pressure of the bulk gas is in equilibrium with the liquid phase and the saturation concentration of the gas in the bulk liquid is in equilibrium with the gas phase (Garcia-Ochoa and Gomez, 2009). The assumption of this equilibrium, allows the calculation of the saturation concentration with Henry's Law (eqn. B.15). The Henry coefficients (H_i) at 298 K (25 °C) are obtained from WebBook. The coefficient is corrected for the temperature applied in the 1D model, 310 K (37 °C), with the equation proposed by WebBook (eqn. B.16).

$$P^* = H_i C^*_{L_r} \tag{B.15}$$

$$\begin{aligned} H_{\mathrm{i}}(T) = H_i^{\circ} e^{(d(\ln(H_{\mathrm{i}}))/d(1/T)((1/T)-1/(298\ \mathrm{K})))} &= 0.00095\ \mathrm{mol/(kg\ bar)} \times e^{\left(1600\cdot\left(\frac{1}{310\ \mathrm{K}}-\frac{1}{298\ \mathrm{K}}\right)\right)} \\ &= 7.71879 \cdot 10^{-4}\ \mathrm{mol/(kg\ bar)} \end{aligned} \tag{B.16}$$

Table B.1: Henry's constant parameters. Parameters used in equation B.16 to calculate Henry's coefficient

Gas	H_i (mol/(kg bar))	H_i° (mol/(kg bar))	$\boldsymbol{d}(\ln(H_i))/\boldsymbol{d}(1/T))$	Temp. (K)	H_i (mol/(m^3 Pa))
CO	7.71879E-4	0.00095	1600	310	7.595E-6

B.2.3 Gas density - ρ_G

The gas density was considered to change over time and length of the riser, due to the gas concentrations that change as a result of mass transfer from the gas to the liquid phase. Therefore, the density was described by the concentrations (mol/m^3) and the molar mass (g/mol) of the gaseous compounds.

$$\rho_G = \sum_i C_{G_r,i} \cdot M_i \tag{B.17}$$

B.2.4 Gas inlet concentration - C_{G_i}

The gas inlet concentrations are calculated using the ideal gas law and the inlet molar fractions of the gaseous compounds present in syngas. The total gas concentration is a function of the ideal gas law (eqn. B.18). The concentrations of the specific gaseous compounds are calculated by multiplication of the total gas concentration and the molar fractions (eqn. B.19).

$$C_{G,0} = \frac{P_b}{(R \cdot T)} \tag{B.18}$$

$$C_{G,i} = C_{G,0} \cdot y_{i,0} \tag{B.19}$$

B.2.5 Gas mass inflow rates - m_{in}

The inlet superficial gas velocities used in the experimental data, were converted to mass inflow rates for the 1D model to obtain similar inlet velocities. Since the inlet velocities in the 1D model were calculated according to the gas mass inflow rate (table B.2.

$$n_{in} = m_{in} \sum_i \frac{y_i}{M_i} \tag{B.20}$$

$$F_{Gr,in} = \frac{P_b}{\mathrm{R}T} \sum_i C_{G_r,i} \cdot M_i \tag{B.21}$$

$$u_{G_r,in} = \frac{F_{Gr,in}}{A_r} \tag{B.22}$$

Table B.2: Inlet superficial gas velocities and mass inflow rates of experimental data and CFD model.

	Inlet superficial gas velocities (cm/s) ($\boldsymbol{u_{G_r,in}}$)	**Gas mass inflow rates (kg/s)** ($\boldsymbol{m_{in}}$)
Young et al. (1991)	0.96	0.0003435
	2.1	0.000754
	4.7	0.001682
	8.2	0.00293
Vial et al. (2002)	1.2	0.000366
	3.7 or 4.3	0.00113 or 0.001313
	6.6	0.002012
	11.7	0.003566
Abrahamson (2019)	-	-
	-	-
	-	-
	9.78	6.658

B.2.6 Liquid inlet liquid velocities - $u_{L_{in}}$

The liquid inlet velocities of the inflow and outflow riser parts of the reactor are calculated with the dilution rate and total liquid volume and surface area of the reactor B.23.

$$u_{L_{in}} = \frac{D_{il} V_{L,tot}}{A_r} \tag{B.23}$$

$$V_{L,tot} = e_{Lr} V_{tot}$$

$$\text{with} \quad V_{tot} = A_r L_i r + A_r L_r + A_d L_d + A_r L_{or} \quad \text{and} \quad A_r = \frac{1}{4}\pi D_r^2$$

B.2.7 Mass transfer coefficient - k_L

The mass transfer coefficient was calculated with the diffusion coefficient of CO, the bubble diameter and bubble rise velocity. The diffusion coefficient was calculated according to the Stokes-Einstein equation (eqn. B.24) (Cussler, 2009). In addition, the solute radius (R_0) presented by Cussler (2009) was used as well. The mass transfer coefficient was only calculated for CO since this was the only compound for which mass transfer occurred.

$$D_{if} = \frac{k_{\mathrm{B}}T}{6\pi\eta_L R_0} = \frac{1.3806 \cdot 10^{-23}\mathrm{J/K} \times 310\mathrm{K}}{6\pi \times 6.922 \cdot 10^{-4}\mathrm{Pa\ s} \times 1.2081 \cdot 10^{-10}\mathrm{m}} = 2.7166 \cdot 10^{-9}\ \mathrm{m^2/s} \tag{B.24}$$

$$k_L = 1.13 \left(\frac{v_{\mathrm{b}}\, D_{\mathrm{if}}}{d_{\mathrm{b}}} \right)^{0.5} \tag{B.25}$$

B.2.8 Inlet concentration riser - $C_{L_r,i,0}$

The inlet concentration of the riser was determined by amount of moles that flow out of the outlet inflow riser and downcomer. Since no dispersion was assumed in the outlet boundaries of the outflow riser and downcomer, the convective flux was used to calculate the amount of moles per surface area reactor per second (mol/m_R^2/s) that flow out of these two parts divided by the flow that is present at the inlet boundary of the riser B.26.

$$C_{L_r,i}(0,t) = \frac{C_{L_d,i}(0,t)\, A_d\, u_{L_d} + C_{L_{ir},i}(L_{ir},t)\, A_r\, u_{L_{ir}}}{A_r\, u_{L_r}} \tag{B.26}$$

Appendix C

Metabolic equations and reaction rates

The metabolism of *C. autoethanogenum* was modelled by an black-box approach. In this approach the microbial metabolism is comprised of and simplified to catabolism and anabolism which are linearly coupled by an energy carrier(Kleerebezem and Van Loosdrecht, 2010). In catabolism Gibbs free energy is generated through the transfer of electrons from the substrate (electron donor) to the product (electron acceptor). The black-box model used by Puiman (2020) was implemented in the 1D model. In this model the stoichiometry of the catabolic reaction is derived from elemental conservation and electrical charge balances(eqn. C.1) as well as the anabolic reaction (eqn. C.2). The free energy that is generated there is used to drive the anabolism. In the anabolic reaction substrate is converted into biomass. The stoichiometry of the metabolic reaction is derived from the anabolic and catabolic reactions. In addition, the parameters in the black-box model calculated by Puiman (2020) were implemented as well.

$$\text{Cat:} \quad -6\,\text{CO} - 3\,\text{H}_2\text{O} + 4\,\text{CO}_2 + 1\,\text{C}_2\text{H}_5\text{OH} \tag{C.1}$$

$$\text{An:} -2.2\,\text{CO} - 0.2\,\text{NH}_4{}^+ - 0.6\,\text{H}_2\text{O} + 1\,\text{C}_1\text{H}_{1.8}\text{O}_{0.5}\text{N}_{0.2} + 1.1\,\text{CO}_2 + 0.2\,\text{H}^+ \tag{C.2}$$

$$\text{Met:} -46.08\,\text{CO} - 0.2\,\text{NH}_4{}^+ - 22.59\,\text{H}_2\text{O} + 1\,\text{C}_1\text{H}_{1.8}\text{O}_{0.5}\text{N}_{0.2} + 30.41\,\text{CO}_2 + 7.33\,\text{C}_2\text{H}_5\text{OH} + 0.2\,\text{H}^+ \tag{C.3}$$

The catabolic maintenance requirements were calculated with the maintenance coefficient. The coefficient described by the black-box approach is dependent on the catabolic maintenance coefficient of the substrate CO and the stoichiometric coefficient of the compound and CO (eqn. C.4). Only the formation of ethanol was considered, therefore only the maintenance coefficient for ethanol was calculated (eqn. C.5).

$$m_{s,i} = \frac{m_{s,co}}{Y_{co}^{cat}} \cdot Y_i^{cat} \qquad \text{with} \quad i = \text{CO, EtOH and X} \tag{C.4}$$

$$m_{s,et} = \frac{1.83944 \cdot 10^{-5}\ \text{mol/mol X/s}}{6} \cdot 1 = 3.06667 \cdot 10^{-6}\ \text{mol/mol X/s} \tag{C.5}$$

Table C.1: Catabolic maintenance coefficients

Compound	$\boldsymbol{m_s}$ (mol/mol X/s)
CO	$1.83944 \cdot 10^{-5}$
Ethanol	$3.06667 \cdot 10^{-6}$

Appendix D

Parametric analyses

D.1 Parametric analysis friction coefficient (K_B)

The difference between experimental data of Young et al. (1991) and Vial et al. (2002) and the predicted superficial liquid velocity by the 1D model as discussed in section 2.3.1, was hypothesized to be influenced by the value of K_B. To analyse the influence of the friction coefficient on the superficial liquid velocity prediction, a parametric analysis was performed. The reactor geometry of Young et al. (1991) and Vial et al. (2002) was applied with inlet superficial gas velocities of: 0.96 cm/s and 8.2 cm/s for Young et al. (1991) and 6.6 and 11.7 cm/s for Vial et al. (2002), respectively. Two different superficial gas velocities were used to examine the influence the superficial inlet gas velocity ($u_{G_r,0}$). The K_B values were varied from 1 until 19. For Young et al. (1991) it is observed that the inlet gas velocity has a substantial impact on the friction coefficient. At a gas inlet velocity of 8.2 cm/s, lower values of the friction coefficients ($K_B < 5$) influence the superficial liquid velocity more than at higher friction ($K_B > 5$) coefficients (fig. D.1a). This influence is observed to be less at a inlet gas velocity of 0.96 cm/s. For Vial et al. (2002) it is also observed that at lower friction coefficients the superficial liquid velocity is more influenced by K_B than at higher friction coefficient ($K_B > 5$) (fig. D.1b). In addition, the influence of K_B is more significant at higher superficial inlet gas velocities for the data of Vial et al. (2002) too.
From both analyses it can be concluded that the friction coefficient can have a significant influence on the superficial liquid velocity in the riser. If the K_B values for the comparison between the predicted u_{Lr} and that of Young et al. (1991) were assumed at around 1-3 in the 1D model, the superficial liquid velocities of the 1D model would have corresponded more to Young et al. (1991). If the K_B values for the comparison of u_{Lr} with Vial et al. (2002) were assumed between 6-9, the superficial liquid velocities of the 1D model would have corresponded to the values obtained by Vial et al. (2002).

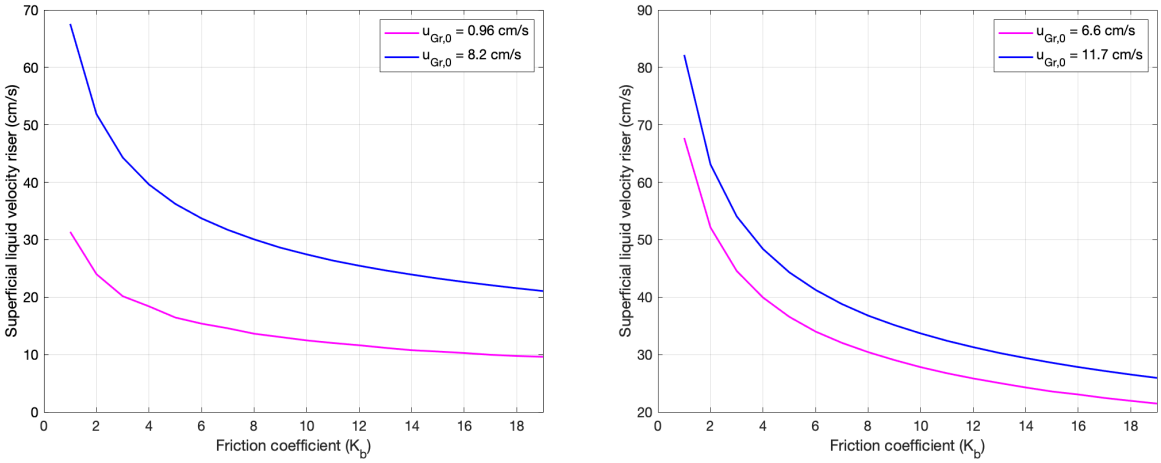

(a) **(b)**

Figure D.1: Parametric analysis of K_B. a) K_B calculated for Young et al. (1991) with superficial gas inlet velocities of 0.96 and 8.2 cm/s, respectively. **b)** K_B calculated for Vial et al. (2002) with superficial gas inlet velocities of 6.6 and 11.7 cm/s, respectively.

D.2 Parametric analysis bubble diameter (d_b)

The difference between the mass transfer of the CFD model and the 1D model was hypothesized to be caused by the different bubble diameters that were assumed in both models. Additionally, larger bubble diameters are expected to have a negative effect on the mass transfer rate. Therefore, the mass transfer rates in the 1D model were compared at constant bubble diameters of 3 and 7 mm, respectively (fig. D.2). It was observed that the CO mass transfer rate was higher at smaller bubble diameters, which confirmed the expectation.

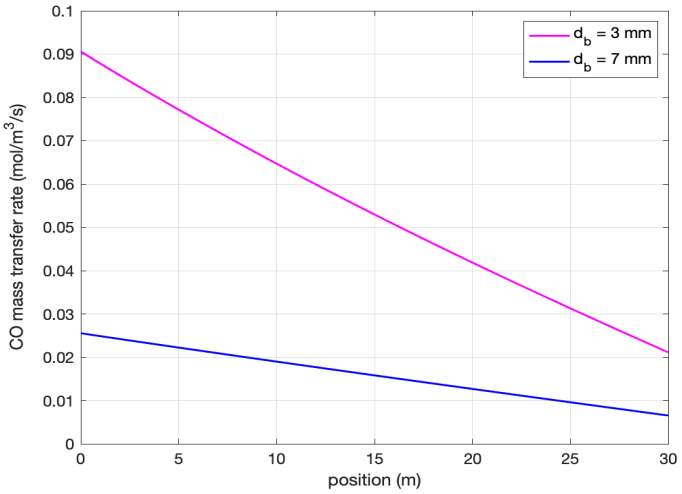

Figure D.2: Influence of d_b on CO mass transfer in 1D model. The CO mass transfer coefficients at 3 and 7 mm of the 1D model are presented over the length of the riser.

Appendix E

Conditional statements

Several correlations and equations are interrelated to predict parameters used in the 1D model. As a result, the parameters at the boundaries of the model were not always solved. To ensure the model solved the model equations, several conditional statements were implemented. The conditional statements are discussed for each parameter it was used for.

E.1 Bubble diameter - d_b

The bubble diameter equation was based on the molar flow in the riser. The molar flowrate was defined as the convective flow of gas (eqn. E.1). The superficial gas velocity and gas concentration were calculated by the model, therefore at the boundary the concentration and velocity were calculated to be zero which caused division by zero in the bubble diameter equation (eqn. E.2, E.3). In addition the bubble diameter was used in other correlations and equations, at small bubble diameters the model did not solve. Therefore, the bubble diameter was set to the initial bubble diameter at too small diameters (eqn. E.4) .

$$n_G = u_{G_r} A_r C_{Gr} \tag{E.1}$$

$$u_{G_r} = \begin{cases} 1 \times 10^{-5} \text{ m/s} & \text{if} \quad u_{G_r} < 1 \times 10^{-5} \quad \text{m/s} \\ u_{G_r} & \text{if} \quad u_{G_r} \geq 1 \times 10^{-5} \quad \text{m/s} \end{cases} \tag{E.2}$$

$$C_{G_r} = \begin{cases} 1 \cdot 10^{-5} & \text{if} \quad C_{G_r} < 1 \cdot 10^{-5} \text{ mol/m}^3 \\ C_{G_r} & \text{if} \quad C_{G_r} \geq 1 \cdot 10^{-5} \text{ mol/m}^3 \end{cases} \tag{E.3}$$

$$d_b = \begin{cases} d_{b,0} & \text{if} \quad d_b < 0.0015 \text{ m} \\ d_b & \text{if} \quad d_b \geq 0.0015 \text{ m} \end{cases} \tag{E.4}$$

E.2 Liquid dispersion coefficient - D_L

The liquid dispersion coefficient was based on the superficial gas velocity, since the superficial gas velocity is calculated by the model. At zero velocity which is calculated by the model, the velocity is considered to be a very small value.

$$u_{G_r} = \begin{cases} 1 \cdot 10^{-8} & \text{if} \quad u_{G_r} < 1 \cdot 10^{-8} \text{ m/s} \\ u_{G_r} & \text{if} \quad u_{G_r} \geq 1 \cdot 10^{-8} \text{ m/s} \end{cases}$$

E.3 Total gas concentration

The gas concentration of all gaseous compounds was used to calculate the change of molar fractions due to mass transfer. Since, the model did not solve at too low concentrations, a conditional statement was implemented (eqn. E.5).

$$C_{G_r} = \begin{cases} 1 \cdot 10^{-3} & \text{if} \quad C_{G_r} < 1 \cdot 10^{-3} \text{ mol/m}^3 \\ C_{G_r} & \text{if} \quad C_{G_r} \geq 1 \cdot 10^{-3} \text{ mol/m}^3 \end{cases} \tag{E.5}$$

E.4 Ethanol inhibition - I_{et}

The ethanol inhibition was conditioned to prevent ethanol concentrations above the inhibition constant ($K_{I,et}$), since the constant should inhibit the micro-organism at too high ethanol concentrations.

$$I_{et} = \begin{cases} I_{et} & \text{if} \quad C_{L,et} \leq K_{I,et} \\ 0 & \text{if} \quad C_{L,et} > K_{I,et} \end{cases} \tag{E.6}$$

E.5 Growth rate - μ

The growth rate was conditioned to prevent the growth rate becoming a negative value. The growth rate is assumed to be zero when the uptake rate of CO is reaches the value of the CO maintenance coefficient.

$$\mu = \begin{cases} 0 & \text{if} \quad q_{co} \leq m_{s,co} \\ \mu & \text{if} \quad q_{co} > m_{s,co} \end{cases} \tag{E.7}$$

E.6 Pressure - P

The pressure was conditioned due to the varying density of the gas ρ_G. The density was dependent on the concentrations of the gaseous compounds in the gas phase, which vary due to mass transfer. Since the concentrations are zero at initial times, pressure is considered very small.

$$P = \begin{cases} 1 \cdot 10^{-16} & \text{if} \quad P \leq 1 \cdot 10^{-16} \\ P & \text{if} \quad P > 1 \cdot 10^{-16} \end{cases} \tag{E.8}$$

Appendix F

Optimization procedure

The superficial liquid velocity and the gas hold-up are predicted by an optimization method. Since the superficial liquid velocity and gas hold-up are interrelated, solving the model without the optimization method was impossible. The iterative procedure proposed by Chisti and Moo-Young (1993) was used as basis for the optimization. In this iterative procedure a initial guess for the superficial liquid velocity is made. Subsequently, the gas hold-up is calculated according to a proposed correlation along with other parameters present in the superficial liquid velocity equation presented by Chisti et al. (1988). The calculated superficial liquid velocity is compared to the initial guess, when both values agree the iterative procedure is stopped. Since Comsol Multiphysics was used to solve the 1D model, such an iterative procedure was considered to be complex to implement. Therefore, an optimization method was used instead. In the optimization the superficial liquid velocity (eqn. F.1) and gas hold-up equations (eqn. F.2) proposed by Chisti and Moo-Young (1993) were used and formulated in as an objective function. In this function the gas hold-up equation was formulated to an equation in which the superficial liquid velocity is a function of the gas hold-up and the superficial liquid velocity (eqn. F.3). The objective function was formulated as the sum of smallest residuals of equations F.1 and F.3. The Nelder-Mead method was used to minimize the objective function to obtain the gas hold-up and superficial liquid velocity in the riser. The lower and upper limit of the minimization were set to the gas hold-up in the downcomer (ε_{G_d}) and the upper limit was obtained through an iterative procedure.

$$u_{L_r} = \left[\frac{2gL_r \left(\varepsilon_{L_r} - \varepsilon_{L_d}\right)}{K_B \left(\frac{1}{\left(1-\varepsilon_{L_r}\right)^2} + \left(\frac{A_r}{A_d}\right)^2 \frac{1}{\left(1-\varepsilon_{L_d}\right)^2} \right)} \right]^{0.5} \tag{F.1}$$

$$\varepsilon_{G_r} = \frac{u_{G_r}}{0.24 + 1.35 \left(u_{G_r} + u_{L_r}\right)^{0.93}} \tag{F.2}$$

$$u_{L_r}\left(\varepsilon_{G_r}\right) = \left(\frac{u_{G_r} - 0.24\varepsilon_{G_r}}{1.35\varepsilon_{G_r}} \right)^{\frac{100}{93}} - u_{G_r} \tag{F.3}$$

$$q = \left(u_{L_r}\left(\varepsilon_{G_r}\right)|_{F.1} - u_{L_r}\left(\varepsilon_{G_r}\right)|_{F.3} \right)^2 \tag{F.4}$$

Lower limit: ε_{G_d} and Upper limit: $\frac{u_{G_r,in}}{1.35 \cdot 0.24 \text{ m/s}}$

Appendix G

Industrial LanzaTech process estimations

The parameters of the industrial LanzaTech process were roughly estimated with the little available data and estimations. From LanzaTechs own publications some data is available on the industrial process (table G.1). The ethanol titer was considered to be around 50 g/L due to high cost of downstream processing at higher concentrations. Furthermore the yields of the black-box model were used (table G.1).

Table G.1: Parameters from LanzaTech available in literature and approximations of parameters made for calculations

Parameter	**LanzaTech**	**Parameter**	**Assumptions**
Annual production	50 kton/year	Operation hours	8000 h
Reactor height	25-30 m	yield CO/EtOH	6.28
Reactor diameter	5 m	yield CO/X	46
Conversion CO	90 %	yield EtOH/X	0.1365
Gas composition	50 % CO/ 50 % N_2	gas mass inflow	2.11 kg/s
$C_{X,in}$	5 g/L		

Simple mass balances were established for CO, ethanol and biomass in the reactor assuming steady state and a continuous process. Only the ethanol production rate was calculated with the annual production and operating hours (eqn. G.4). The CO consumption rate and biomass production rate were both calculated with the ethanol production rate and yields, respectively. Furthermore, the productivity of all three compounds was calculated using the reaction rate and reactor volume. The CO-to-ethanol yield was estimated with the reaction rates, that were calculated (table G.4).

$$\frac{dC_{et}}{dt} = F_{out}C_{et} + R_{et} = 0 \tag{G.1}$$

$$\frac{dC_X}{dt} = F_{in}C_X - F_{out}C_X + R_X = 0 \tag{G.2}$$

$$\frac{dC_{CO}}{dt} = F_{in}C_{CO} - F_{out}C_{CO} - R_{CO} = 0 \tag{G.3}$$

$$R_{r,et} = \frac{50 \text{ kton/year}}{8000 \text{ h/year}} = 0.2894 \text{ kg/s} = 6.29 \text{ mol/s} \tag{G.4}$$

Table G.2: Approximated mass flow and productivity rates of industrial LanzaTech process.

Estimated parameters	**Rate**	**Productivity**
Ethanol production	6.29 mol/s	2.083 g/L/h
CO consumption	39.5 mol/s	7.964 g/L/h
Biomass production	21.13 g/s	0.152 g/L/h
Yield EtOH/CO	26 %	2.083